UCSF
UC San Francisco Electronic Theses and Dissertations

Title
A Multiparametric MRI for the Classification and Grading of Prostate Cancer

Permalink
https://escholarship.org/uc/item/30p0x6mt

Author
Korn, Natalie

Publication Date
2019

Peer reviewed|Thesis/dissertation

eScholarship.org Powered by the California Digital Library
University of California

A Multiparametric MRI for the Classification and Grading of Prostate Cancer

by

Natalie Korn

DISSERTATION

Submitted in partial satisfaction of the requirements for degree of

DOCTOR OF PHILOSOPHY

in

Bioengineering

in the

GRADUATE DIVISION

of the

UNIVERSITY OF CALIFORNIA, SAN FRANCISCO
AND
UNIVERSITY OF CALIFORNIA, BERKELEY

Approved:

DocuSigned by:
John Kurhanewicz
593BD10CA23A498...

John Kurhanewicz

Chair

DocuSigned by:
Susan Noworolski

Susan Noworolski

DocuSigned by:
Antonio Westphalen
ECB2282AD4DC4D2...

Antonio Westphalen

Committee Members

Copyright 2019
by
Natalie Korn

"Well, I'm glad it's not harder than it is!" - Sensei

Acknowledgments

I am so lucky to have had the wonderful mentors I've had while working at UCSF. I owe my scientific career to Dr. Susan Noworolski, who taught me to write in bash and perl, taught me how to actually write in MatLab, and arguably taught me how to write in English. Sue was my boss as a research associate, and counseled me through my Master's before becoming my PhD mentor. You taught me how to do each part of a human MR experiment, from pulse sequence design to the physical acquisition, to image processing and to statistics.

Dr. John Kurhanewicz has been a mentor to me since before my PhD began, and I've had the opportunity to work closely with John over the past two years on the hyperpolarized research team. Thank you for showing me the process of translating a research protocol to the clinic, guiding me through the process of applying for this PhD, and including me in your lab dynamics as I began working at Mission Bay.

Dr. Antonio Westphalen has always been available to remind me why we do what we do, how close we are to our patients and what they deserve from medical research. I would like to extend a particular thanks to Dr. Peder Larson, for writing most of the advance pulse sequences I've used, as well as most of the spectroscopic processing code I've used, teaching me all of MR physics twice, and yet always being kind and humble in person. Dr. Daniel Vigneron has been a voice of reason so many times as my graduate mentor, counseling me through my qualifying exam and bringing me onto the team of carbon-13 researchers.

None of this work would be possible without dedicated staff, ready to roll with the punches we throw as we flail towards science. Dr. Bob Bok, Lynn Delos Santos, Bert

Jimenez, Allison Fuller, Kimberly Okamoto, Nicole Bronson, Vahid Ravanfar, Mary Frost, and Hope Williams are rigorous and thorough medical staff who manage to provide quality care to our patients while we find ever more complicated things to do. Barbara Green is a great friend, and has helped pull our research and people through more than her fair share of administrative tape, as has Celestine Fry, Kathy Devine, Jenny Che, Kim Semien, and Thomas Mattes. Ana Marie DeLuca fought a sea monster to get me a new laptop. Students in the Bioengineering program are also lucky to have SarahJane Taylor and Kristin Olson as administrators. They navigate this complex program split between two schools with so much kindness, I am so grateful for the myriad of problem solving they both do.

Teaching the MatLab bootcamp was an important part of my time as a graduate student. Thank you to Rukayah Abdolcader for making most of the MSBI program actually possible, and to Robert Smith for doing so in years past. Thank you to Dr. Alastair Martin and Dr. David Saloner for allowing me to take on the bootcamp and expand it however I liked for three years. And my thanks to my students for being open, questioning, and collaborative, and teaching me so much! Thank you to Dr. Julie Owen for the work she put in to establish the bootcamp, and thank you to Alejandro Morales Martinez for being a wonderful TA and so intentionally and passionately taking it over. Go make it better than I did.

I have wonderful people to look up to. Olga Starobinets was my model of how to be a research associate, how to transition to graduate school, and how to be a graduate student. The five years we shared a cube were so fun, I almost forgive you for moving. Galen Reed and Cornelius von Morze have never worked with me on any projects, yet have taught me

how to use equipment, helped me understand a lot of physics, and been consistently available for (repeating the same) advice. You are two of my most treasured mentors and friends.

What I'll miss most about UCSF is the bonds of camaraderie and friendship with my peers. Justin Delos Santos and Sonam Iqbal were early compatriots in clinical work, managing our schedules and managing to make real differences in the lives of our patients. More recently, labmates like Jessie Lee, Dave Korenchan, Jeremy Bancroft Brown, and Hecong Qin have really been willing to help me look for the path when I can't find it. Jinny Sun especially has been like a sister to me over the last year.

Living thousands of miles away from my family wouldn't be possible without the support network of friends I still can't believe I have, for each Shabbat dinner and each moment in between, my emergency contacts: Molly Conway, Win Wallace, Meb Byrne, Tom Byrne, Katie Mock, Bradan Litzinger, Ash Redfield, Tenaya Raives, Mickey Finn, Loui Conde, Whitney Moses, Sarah Gzesh and Das Rush are my best friends, and I could not have done this without you all.

Lastly I want to thank my amazing family, watching my parents work in medicine made me so sure from so young that I definitely didn't want to be a doctor..but wanted to help them work! To my mother, April Weeks, and my father, Len Korn, as well as my step parents, Elyse Barry and Rich Antal, and my entire extended family, thank you for pushing me towards my dream of doing scientific research since I was a little kid, and supporting me through the crazy ride, including moving across the country! You continue to inspire me to realize what is truly important in life.

A Multiparametric MRI for the Classification and Grading of Prostate Cancer

Natalie Korn

Abstract

Prostate cancer is one of the most common diseases in men worldwide, however only a small percentage of men with prostate cancer have aggressive cancer, and most men diagnosed with focal disease have indolent disease with low risk of progression compared to the risks associated with treatment. There is a current, pressing need to differentiate between aggressive and indolent prostate cancers in ways that are minimally invasive and not damaging to patients. This dissertation proposes the multiparametric MRI of the prostate, with its inherent non-invasive technique void of harmful radiation, as a solution. However, the current multiparametric MRI of the prostate is not widespread, due to lingering artifacts and ambiguous results in some acquisitions. In this work, we provide improvements to pulse sequence software, acquisition hardware, and image-processing software for the multiparametric MRI of the prostate. Additionally, we introduce hyperpolarized carbon-13 imaging in patients as part of a phase 2 clinical trial, with the unique ability to quantify tissue energetics as a signature of prostate cancer's abnormal metabolism.

Table of Contents

1 Practical aspects of prostate MRI: hardware and software considerations, protocols, and patient preparation **4**
1.1 History, Environment Hardware and Patient Preparation 5
1.2 Anatomic T_1- and T_2-weighted Imaging 10
1.3 Diffusion-weighted Imaging 15
1.4 Dynamic Contrast-enhanced Imaging 20
1.5 ^{1}H MR Spectroscopic Imaging 25
1.6 ^{13}C MR Spectroscopic Imaging 29
1.7 Conclusion 32

2 A Reduced-FOV Excitation Decreases Susceptibility Artifact in Diffusion-weighted MRI for Prostate Cancer Detection **33**
2.1 Introduction 34
2.2 Materials and Methods 35
2.3 Results 41
2.4 Discussion 44

3 Distinguishing Inflammation from Low-Grade Prostate Cancer in the Peripheral Zone of the Prostate **51**
3.1 Introduction 52
3.2 Materials and Methods 54
3.3 Results 56
3.4 Discussion 61

4 Multi-element, Multi-nuclear Endorectal Coil for Development of a ^{13}C, ^{1}H-Multiparametric Magnetic Resonance Imaging Exam of the Human Prostate at 3T **66**
4.1 Background and Significance 67
4.2 Prototype Design and Simulation Results 72
4.3 Future Directions 81

5 The Rate of Hyperpolarized [1-^{13}C]Pyruvate to [1-^{13}C]Lactate Conversion Distinguishes High-Grade from Low-Grade Prostate Cancer in Patients **82**
5.1 Introduction 83
5.2 Materials and Methods 86
5.3 Results 90
5.4 Discussion 97

Bibliography **104**

List of Figures

1.1 A Multiparametric MRI of the Prostate 6

1.2 Oblique axial T_2 with and without an ERC 9

1.3 T_1 Decay over 60 Seconds 12

1.4 T_2 Decay over 60 Seconds 14

1.5 2D and 3D Axial T_2-weighted Images of the Prostate 15

1.6 Stejskal-Tanner Pulsed Gradient Diffusion Model 16

1.7 Full- and reduced-Field-of-View DWI 20

1.8 Common Enhancement Curves in DCE 24

1.9 ^{1}H-MRSI in Cancer and Contralateral Benign Tissue 27

1.10 ^{13}C-MRSI in Murine Models 31

2.1 Distortion Scores from Sample Patients 39

2.2 A Typical Distortion Pattern 43

2.3 A Distortion Case from Contamination Aritfact 43

3.1 Decision Tree Classifier 57

3.2 Signal intensities in Inflammation, Low-grade Prostate Cancer, and Normal Peripheral Zone Tissue 59
3.3 Representative Inflammation and Low-grade Prostate Cancer in a Patient 60
3.4 DCE MRI Time Signatures for Inflammation, Low-grade Prostate Cancer, and Normal Peripheral Zone Tissue 61

4.1 Semi-automatic Segmentation of the Prostate 74
4.2 Proposed Coil Array Geometry 75
4.3 Receive Field Profile Simulation 76
4.4 Solid Copper Inductive Coupling Prototype 78
4.5 2D Simulation of Oblique Axial Field Map over Prostate Sizes 79

5.1 A patient with Aggressive, High-grade Prostate Cancer 93
5.2 A Patient with Indolent, Low-grade Prostate Cancer 94
5.3 Box Plot of the Maximum Values of Carbon Parameters 95
5.4 A Patient with Bilateral Disease 96
5.5 ROC Analyses 97

List of Tables

2.1 Distortion Scoring Statistics Table 42

2.2 Contrast-to-Noise Ratio Comparison 44

4.1 Prostate Size Distributions in 847 Patients 79

5.1 Clinical Presentation of Patients in a Phase 2 Clinical Trial of Carbon Imaging of Prostate Cancers 92

5.2 Carbon Parameters in Normal Peripheral Zone, Low-grade, and High-grade Prostate Cancers. 94

Introduction

Prostate cancer is one of the most common types of cancer in American men. Although the prevalence is high in the US and abroad, the mortality rate for prostate cancer is proportionally low and the risk of lowering quality of life with therapeutic interventions is relatively high. Clinicians and hospitals are faced with increasing numbers of prostate cancer patients and treatment decisions, and the need to improve diagnostic tools.

The multiparametric MRI (mpMRI) exam of the prostate is a powerful noninvasive tool for the detection and staging of prostate cancer. First popularized by the widespread combination of high-resolution T_2-weighted imaging with functional diffusion-weighted imaging (DWI), a number of versions of the prostate mpMRI exam now exist in major hospitals around the world.

In Chapter 1, we present the current state of the multiparametric MRI prostate exam. We present the practical aspects of acquiring an mpMRI including T_1-weighted and T_2-weighted imaging to assess anatomy, diffusion-weighted imaging (DWI) to detect changes in tissue cellularity, dynamic contrast-enhanced imaging (DCE) to semi-quantitatively analyze perfusion and tissue cellularity and structure, proton spectroscopic imaging (^{1}H-MRSI) to measure differences in steady state metabolite levels, and carbon-13 spectroscopic imaging (^{13}C-MRSI), with the potential to probe rates of metabolic reactions in patients. We further present considerations in hardware, patient preparation, and standardization.

In Chapter 2, we present a solution to the susceptibility artifact common in DWI of the

prostate. DWI is the most common functional imaging sequence used in prostate cancer mpMRI exams. However, susceptibility artifact from the adjacent rectum can distort the peripheral zone of the prostate, where 70% of prostate cancers are located. Our solution is a pulse sequence modification using a reduced Field-of-View excitation, based on a sequence developed to decrease similar artifact in the spinal column. By using a 90°, 2D spatially-selective, echo-planar RF pulse to limit the excitation in the phase-encode direction suffering from susceptibility artifact, we show significantly less distortion in the resulting apparent diffusion coefficient (ADC) maps.

In Chapter 3, we develop a model to distinguish inflammation in the peripheral zone of the prostate from low-grade prostate cancer based on DWI and dynamic contrast-enhanced imaging (DCE MRI). Inflammation is a common confounder of prostate mpMRI because of its similar signature to low-grade prostate cancer on ADC maps produced from DWI. Using post-radical prostatectomy whole-mount data labeled with Gleason scores of cancers and regions of chronic inflammation, we construct a decision tree model that distinguishes 80% of regions of inflammation from regions of low-grade prostate cancer, and make recommendations for inclusion in the American College of Radiology's Prostate Imaging Reporting and Data System (PI-RADS).

In Chapter 4, we propose an improvement in the acquisition hardware used for acquiring an mpMRI by creating a dual-tuned, multi-element endorectal coil to facilitate the translation of hyperpolarized ^{13}C-MRSI into the clinic. Hyperpolarized metabolic imaging offers real-time quantification of metabolic rates, correlating changes in cellular metabolic path-

ways, such as aerobic glycolysis and the tricarboxylic acid (TCA) cycle, to the presence, aggressiveness and response of cancer to therapy. Hyperpolarized ^{13}C MRI data of the prostate needs to be acquired rapidly due to the relatively rapid relaxation of the hyperpolarized state (the T_1 relaxation rate of the ^{13}C nuclei) and also requires 3D coverage of the prostate to be clinically useful. We aim to take advantage of the increased speed of parallel imaging, which requires the construction of a multi-element endorectal RF coil optimized for prostate imaging. We present simulated fields of several potential coil geometries, based on the Bio-Savart law, and find a three-element longitudinal design to provide increased imaging acceleration factor, increased field strength in the peripheral zone, and sufficient coverage of the anterior prostate.

In Chapter 5, we introduce findings from the first phase 2 clinical trial of hyperpolarized ^{13}C-MRSI in the human prostate. We discuss incorporating acquisition design from murine models and the phase 1 clinical trial at UCSF, and add pharmacokinetic modeling to quantify the rate of metabolic conversion of [1-^{13}C]pyruvate to [1-^{13}C]lactate, k_{PL}. We find that hyperpolarized ^{13}C-MRSI can distinguish metabolically-aggressive high-grade prostate cancer from indolent low-grade prostate cancers, based on correlation with whole-mount pathology after radical prostatectomy.

Chapter 1

Practical aspects of prostate MRI: hardware and software considerations, protocols, and patient preparation

Abstract

The use of multiparametric MRI scans for the evaluation of men with prostate cancer has increased dramatically and is likely to continue expanding as new developments come to practice. However, it has not yet gained the same level of acceptance of other imaging tests, partly due to lack of standardization in both the scan environment and imaging protocol design. In this chapter, we describe several practical aspects of prostate MRI that may facilitate the implementation of new prostate imaging programs or the expansion of existing ones, beginning with an overview of the scan environment before focusing on the imaging protocol.

1.1 History, Environment Hardware and Patient Preparation

Multiparametric magnetic resonance imaging (mpMRI) of the prostate combines anatomic with functional and physiological assessment of the gland, and encompasses various sequences, including T_1- and T_2-weighted MR imaging, diffusion-weighted imaging (DWI), dynamic contrast-enhanced (DCE) MRI, and possibly including proton magnetic resonance spectroscopic imaging (^{1}H-MRSI)[1] [2] as shown in Fig. 1.1.

In addition to structural data, the mpMRI exam offers information about the microscopic mobility of water, biochemical characteristics, neovascularity, and cellular structure of the prostatic tissue. Since these characteristics are different for malignant and benign tissues, high-resolution mpMRI provides valuable data that helps characterize the extent and biological behavior of prostate cancer, and is increasingly being used to assist patients and clinicians to make more informed decisions on treatment [3] [4] [5].

The mpMRI exam can offer a comprehensive assessment of the prostate using metrics that can be tailored according to the patient's clinical need, with particular attention to the patient's treatment history [7]. The imaging metrics most relevant to diagnosis may change for imaging patients after radiation [8], focal brachytherapy [9], hormone treatment and/or surgery [10]. Implants associated with abdominal and pelvic comorbidities—such as hip replacements or lumbar fusions [11]—can significantly affect image quality for certain modalities, however the detrimental effect of implants on MR imaging is changing with increased usage of non-metallic implants [12].

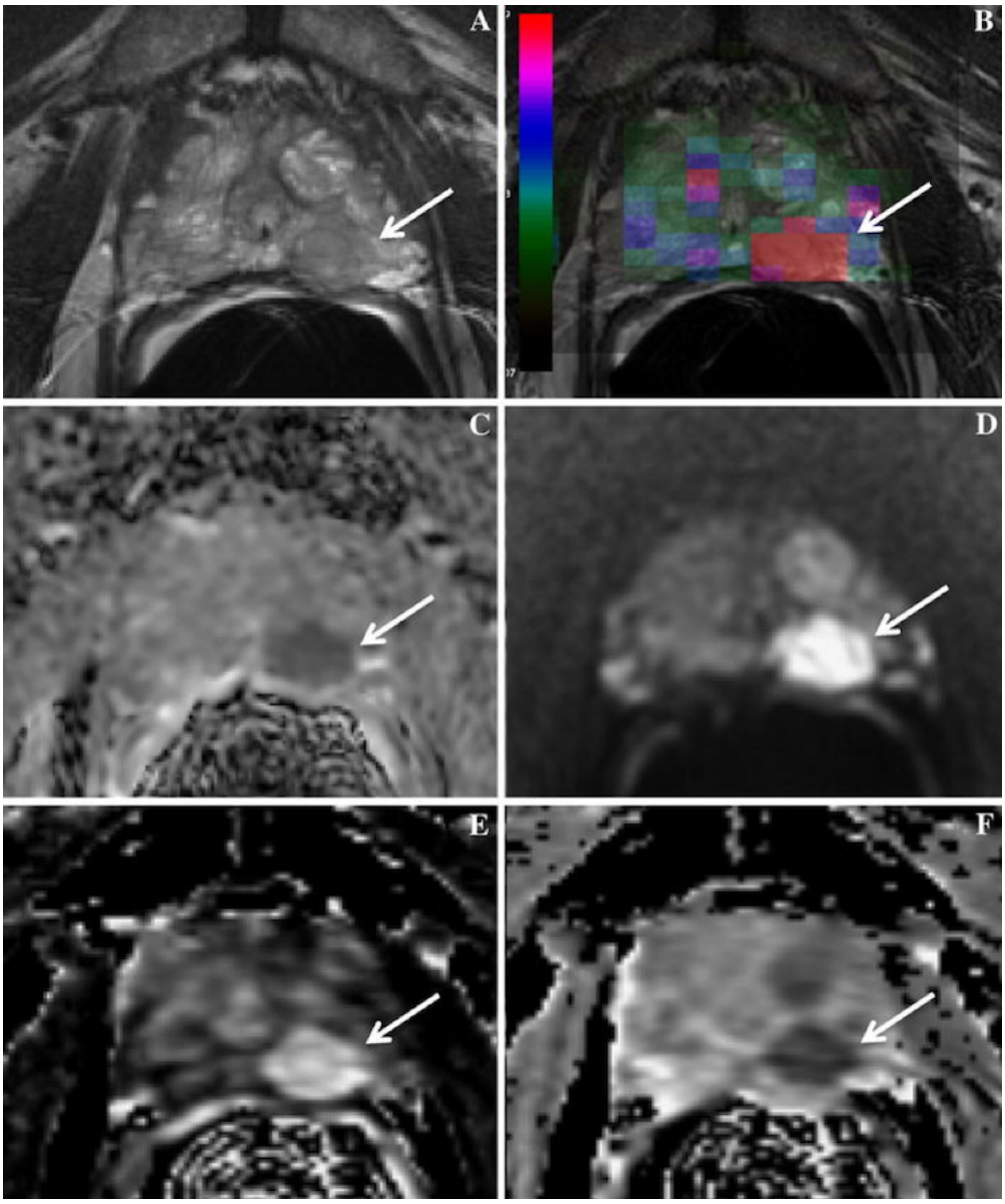

Figure 1.1: An untreated 78-year-old man with serum PSA of 9.8 ng/mL showing a, **A** coil-corrected T_2-weighted FSE image, **B** MRSI choline metabolite map created in SIVIC [6], **C** rFOV ADC map (b = 0, 600 s/mm^2), **D** coil-corrected rFOV DWI (b = 0, 1350 s/mm^2), and DCE-derived semi-quantitative parameters of **E** enhancement slope, and **F** washout slope. Subsequent TRUS–MRI fusion-guided biopsy revealed a Gleason 4+3 lesion in the left apex, indicated by white arrows.

The mpMRI of the prostate, however, suffers from lack of standardization, leading to variable performance between sites. The American College of Radiology (ACR), the European Society of Urogenital Radiology, and the AdMeTech Foundation have proposed the use of the Prostate Imaging Reporting and Data System (PI-RADS), now in its second version [13]. In PI-RADS, the ACR describes the minimum recommended parameters for imaging patients, among other important aspects of mpMRI. In this chapter, we discuss various aspects of imaging acquisition and suggest protocols that may be used for more optimal assessment of patients with prostate cancer.

MpMRI prostate imaging was initially implemented on 1.5-Tesla (1.5T) scanners [14] [15]. To acquire scans with diagnostic value, a pelvic phased array was used in combination with and an endorectal coil (ERC) [16]. In prostate MR imaging, ERCs can provide a nine-fold improvement in the signal-to-noise ratio (SNR) and spatial resolution when compared to pelvic phased array coils alone [17]. This has a profound impact on the quality of functional imaging, such as MRSI and DWI. Traditional ERCs use a balloon-filled coil, inflated with 40–80 mL of either an inert fluid that matches the susceptibility of the prostatic tissues, such as perfluorocarbon (PFC) [17], or with air or water. Using an inert fluid instead of air or water improves the homogeneity of the magnetic field and decreases susceptibility artifacts between the rectum and the prostate [18]. Using either a rigid or an inflatable ERC will create an inhomogeneous reception profile which results in higher signal intensity near the rectal wall and may hinder cancer detection in the peripheral zone. Fortunately, this signal non-uniformity can be easily rectified using readily available coil-correction software [19].

The introduction of 3-Tesla (3T) clinical scanners presented an opportunity to enhance image quality by trading the increased SNR for improvements in spatial and temporal resolutions, decreasing the necessity of an ERC. The nine-fold SNR increase provided by an ERC can only be partially replaced by a two-fold SNR improvement in doubling the magnet strength. Nevertheless, with advances in pulse sequence design, several groups reported that studies done solely with 6 to 32 phased array surface coils at 3T yielded comparable images as the exams conducted with 1.5T scanners with an endorectal coil [20]. A comparison study with and without an ERC at 3T showed increased sensitivity (0.45, no ERC and 0.75, with ERC) and positive predictive value (0.64, no ERC and 0.80, ERC) for prostate cancer detection [21] when using an ERC (Fig. 1.2). However, considering patient discomfort, patient preparation, costs, coil placement time, and anatomical distortion associated with ERCs, the use of ERCs in prostate imaging is still being actively debated. An important note on this point is the different aims of prostate cancer imaging. In the U.S., an mpMRI of the prostate is generally performed to assist in treatment planning, after either positive biopsy or serial negative biopsies with abnormal blood work or family history. Elsewhere, as in the E.U., much abbreviated mpMRIs of the prostate are performed as a diagnostic procedure without necessary clinical presentation other than advanced age [22]. In that setting, it is easy to see why invasive hardware for marginal quality gain is of less importance than hospital throughput. In this work, we focus on the mpMRI of the prostate as performed in the U.S., with the priority of creating images with the sensitivity to discern disease extent and aggressiveness to assist clinicians in treatment planning.

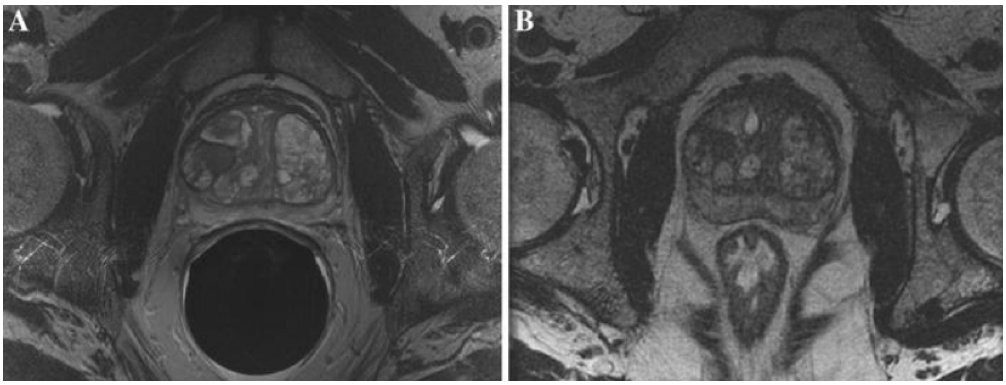

Figure 1.2: An untreated 66-year-old man with no prior biopsies and serum PSA of 7.9 ng/mL. Oblique axial 2D FSE T2-weighted images acquired with 0.35 x 0.35 x 3 mm, **A** with an endorectal coil and **B** without an endorectal coil. This patient was scanned twice in 3 months in anticipation of the MR-guided biopsy. We observe a noticeably increased noise in the image without an ERC, as well as diminished delineation between nodules inside the gland.

We have anecdotally noted that providing patients with information detailing the procedure and the required preparation prior to the exam can improve patient compliance. Patients with severe claustrophobia may be required or advised to bring prescription sedatives to the exam. In some centers, antispasmodic agents like butylscopolamine are administered immediately prior to scanning to decrease bowel peristalsis and potential artifacts related to motion. However, peristaltic suppression is controversial, and some groups have failed to identify a significant improvement of image quality in studies performed on 3T scanner without an ERC [23]. Patients undergoing scans with an ERC should be advised to perform a saline laxative enema within a three-hour window of the exam to facilitate proper endorectal coil placement and minimize susceptibility artifacts associated with air or fecal contamination. Enemas are not required prior to scans done without an ERC, as the improvement in image quality is at best marginal [24].

1.2 Anatomic T_1- and T_2-weighted Imaging

The foundation of the mpMRI, and MR imaging, is high-resolution T_1- and T_2-weighted acquisitions. So-called "anatomic imaging" for the ability to delineate anatomy by combining high resolution with soft tissue contrast, these acquisitions are based on the two principle relaxation phenomena of nuclei returning to equilibrium after excitation by a radiofrequency pulse [25].

To create an MR signal, equilibrium is established by a main magnetic field B_0 and perturbed by a radiofrequency pulse B_1. Relaxation, the return to thermal equilibrium, is the time when MR signals are recorded. It is the difference in the relaxation time constants of nuclei in different microenvironments that gives rise to the most basic of MR images. The process is described fundamentally by the Bloch equation:

$$\frac{dM}{dt} = \mathbf{M} \times \gamma\mathbf{B} - \frac{M_x\mathbf{i} + M_y\mathbf{j}}{T_2} - \frac{(M_z - M_0)\mathbf{k}}{T_1} \tag{1.1}$$

with precession of the net magnetization $\mathbf{M}$ around a magnetic field $\mathbf{B}$, typically described as vectors $\mathbf{M}$=($M_x\mathbf{i}$, $M_y\mathbf{j}$, $M_z\mathbf{k}$) and $\mathbf{B}$=($B_x\mathbf{i}$, $B_y\mathbf{j}$, $B_z\mathbf{k}$), in a 3D coordinate system. Calling the main magnetic field in the z-direction $\mathbf{B}$=$B_0\mathbf{k}$, the magnetization vector $\mathbf{M}$ before RF excitation points along the vector B:

$$\mathbf{M} = M_0\mathbf{k} \tag{1.2}$$

We denote M_0 as the net equilibrium magnetization, a physical property of the magnetized sample dependent on the concentration of nuclear spins, temperature, strength of the mag-

netic field, and Boltzmann's constant. An RF pulse at the resonant frequency of the sample and perpendicular to the z-direction can induce torque on the magnetization vector $\mathbf{M}$, which will precess around the main magnetic field B_0 until returning to thermal equilibrium. The relaxation in the direction of the main magnetic field, ignoring the effects of precession, is shown in Eqn 1.3 by the behavior:

$$\frac{dM_z}{dt} = \frac{(M_z - M_0)\mathbf{k}}{T_1} \tag{1.3}$$

which has a general solution of:

$$M_z(t) = M_0 + (M_z(0) - M_0)\exp^{(-t/T_1)} \tag{1.4}$$

The system will dissipate power over a period of milliseconds as the magnetization returns to thermal equilibrium where $\mathbf{M} = M_0\mathbf{k}$. This is the longitudinal relaxation, or T_1 decay, of the sample in the system. Magnetization along the longitudinal axis according to T_1 decay is shown in Figure 1.3.

A multiparametric MR imaging exam of the prostate typically includes a large field-of-view, axial T_1-weighted scan of the pelvis to assess regional lymph nodes for abnormal size, shape, or intensity. Identification of these lymph nodes is facilitated by the T_1 contrast between the high signal intensity of visceral fat and lower signal intensity of large or irregularly shaped lymph nodes [26]. To ensure that the lymph nodes in the drainage pathway are imaged during the exam, the T_1-weighted scan prescription should extend superiorly to the aortic bifurcation [27]. In addition, these T_1-weighted images offer an opportunity to de-

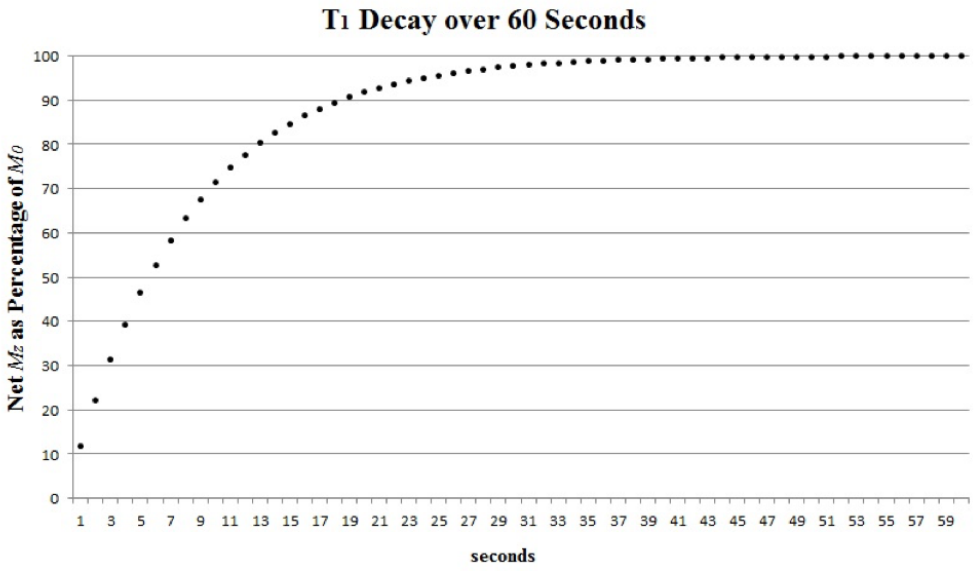

Figure 1.3: T_1 Decay over 60 Seconds according to Eqn 1.4.

tect osseous metastases. While lesions will be incompletely assessed with a single sequence, after correlation with clinical history and histology, further diagnostic steps may be taken. T_1-weighted imaging is also useful to diagnose post-biopsy hemorrhage, which demonstrates high signal intensity [26]. Hemorrhage often has low T_2 signal intensity, mimicking cancer, and may introduce significant artifact on DWI and ^{1}H-MRSI, and confound results from DCE MR imaging. For this reason, an interval of at least 6 weeks between the most recent prostate biopsy and the MRI scan is recommended [28].

T_2 decay, relaxation of the net magnetization vector $\mathbf{M}$ along the plane transverse to the main magnetic field B_0, is a loss of phase coherence in M_{xy} [25]. Before excitation, when $\mathbf{M} = M_0\mathbf{k}$, there is phase coherence along the longitudinal axis. The detectable signal in M_{xy} immediately begins to decay after the RF pulse. The relaxation is described as:

$$\frac{dM_{xy}}{dt} = \frac{M_x\mathbf{i} + M_y\mathbf{j}}{T_2} \tag{1.5}$$

which has a general solution of:

$$M_{xy}(t) = M_0 \exp^{(-t/T_2)} \tag{1.6}$$

Because the loss of coherence decreases the net magnetization vector $\mathbf{M}$ in M_{xy}, the resulting T_2 decay curve decreases with return to thermal equilibrium. Furthermore, because a system in a large magnetic field will undergo simultaneous T_1 decay, and there is phase coherence when $\mathbf{M} = M_0\mathbf{k}$, $T_2 \leq T_1$. Magnetization along the longitudinal axis according to T_2 decay is shown in Figure 1.4.

Multiplanar high-resolution two-dimensional (2D) fast spin-echo (FSE) T_2-weighted MR images provide exquisite soft-tissue contrast and excellent depiction of zonal anatomy, and are the backbone of MR imaging of the prostate. The majority of prostate cancers are adenocarcinomas that arise within the peripheral zone, which have low signal intensity against the background of the bright peripheral zone tissue on T_2-weighted imaging. Transitional zone tumors represent most of the remaining prostate cancers. Similarly to peripheral zone cancers, these lesions usually have low signal intensity on T_2-weighted imaging but can be difficult to distinguish from benign tissue, in particular in the presence of benign prostatic hyperplasia (BPH). T_2-weighted imaging is also the main sequence utilized to assess local spread of cancer, however the diagnostic accuracy is higher when it is combined with other functional sequences [29].

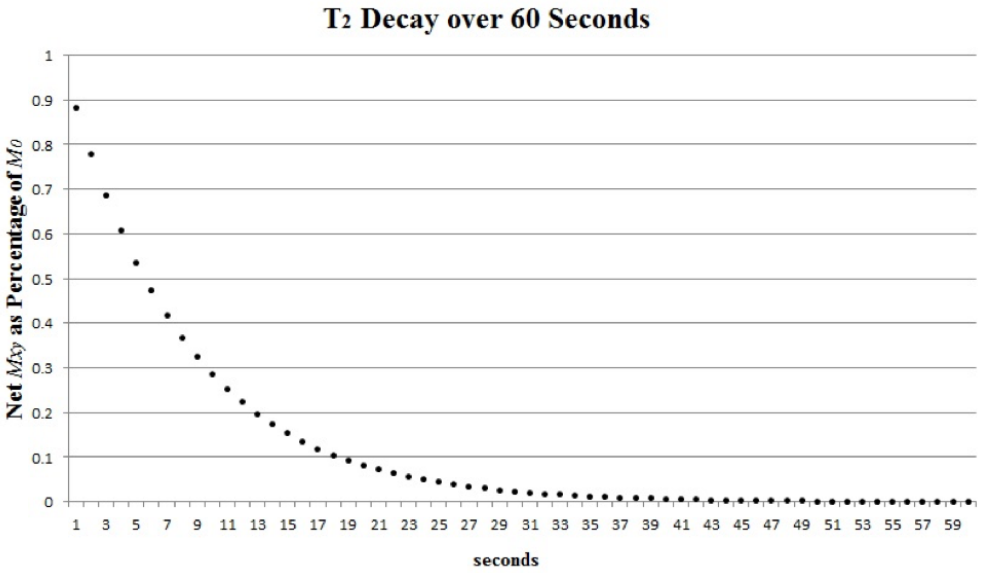

Figure 1.4: T_2 Decay over 60 Seconds according to Eqn 1.6.

High-resolution 2D FSE T_2-weighted images are acquired in the true sagittal plane, as well as the oblique axial (Figure 1.1) and oblique coronal planes of the prostate. The slice thickness should not be more than 3 mm, without a gap, and the in-plane dimension of $\leq$ 0.7mm (phase) x $\leq$ 0.4mm (frequency). For most patients, a field-of-view of 12–18 cm will include the entire gland and seminal vesicles. High-resolution 3D FSE T_2-weighted MR imaging has emerged as a promising technique that allows for the acquisition of isotropic images and may save time by reducing the number of sequences that need to be obtained. However, the quality of the 3D sequence may be limited if acquired on older or low-field magnets due to the need for thinly sliced images for adequate reformatting. While the T_2 contrast is not the same as seen in 2D acquisitions, it is clinically acceptable [30]. Data of a study by Westphalen et al. showed that the preference for the 2D or 3D FSE MR images varies widely among radiologists, but without differences in their ability to delineate the

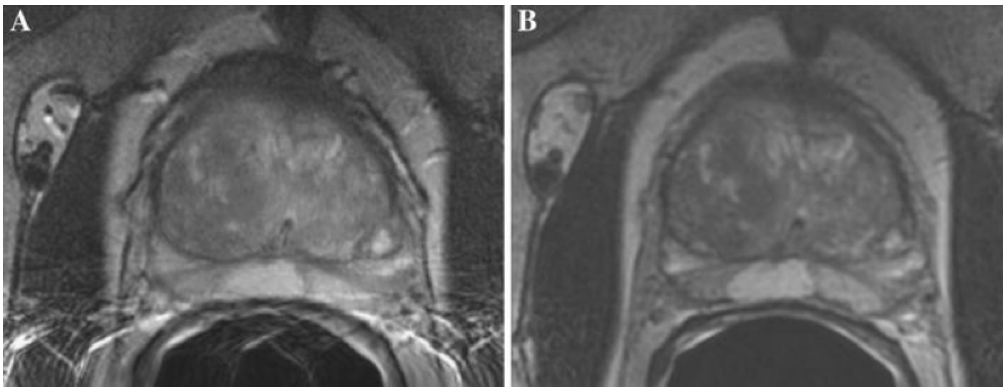

Figure 1.5: An untreated 61-year-old man with biopsied Gleason 3 + 3 prostate cancer and serum PSA of 5.6 ng/mL showing an oblique axial, **A** T_2-weighted FSE anatomic image and **B** T_2-weighted 3D FSE anatomic image. The phase-encoding direction aliasing artifact present in the FSE image is not present in the CUBE image. However, the 3D FSE image has less contrast in comparison to the 2D FSE

anatomy and identify cancer [31]. This same study did find differences in image sharpness and the presence of some artifacts. The 2D FSE images were sharper than the 3D ones but demonstrated more artifacts (Figure 1.5).

1.3 Diffusion-weighted Imaging

Diffusion-weighted imaging (DWI) exploits the random motion of water molecules in biological tissues to characterize disease. Water molecules travel through nearly all tissues and, as in T_1- and T_2-weighted imaging, our resulting image is a record of differences in the rate of the phenomenon over a unit of time. DWI is typically performed using a pulsed gradient spin-echo approach originally presented by Stejskal and Tanner [32], shown in Figure 1.6.

After excitation into the transverse plane, equal amplitude and duration gradients (called diffusion gradients) are played on either side of a 180° refocusing pulse. After the first

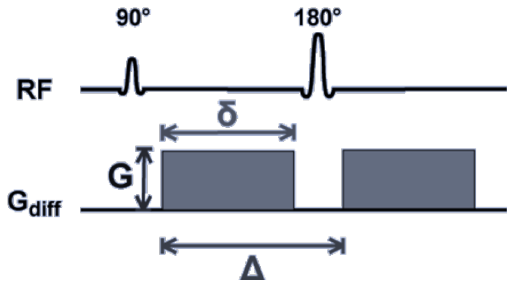

Figure 1.6: Stejskal-Tanner pulsed gradient diffusion model [32].

diffusion gradient, molecules will accumulate phase. After the refocusing pulse, a molecule experiencing no change in position will see the same gradient power in opposing directions, cancelling any accumulated phase and restoring the signal amplitude to its strength before the diffusion gradients. A moving molecule, however, will experience two different diffusion gradients based on two positions in time. This mismatch leads to phase accumulation and weaker signal strength.

The amount of motion the pulsed gradient spin-echo approach can detect is determined by the diffusion gradients [25]. The magnitude (G), duration (δ), and interval (Δ) of the gradient lobes in Figure 1.6 can be tuned based on the limits of given hardware. The b-value in DWI is a conglomerate variable reflecting the gradient shape and timing:

$$b = \gamma^2 G^2 \delta^2 (\Delta - \frac{\delta}{3}) \tag{1.7}$$

which can be simply related to the signal strength after the diffusion gradients have been played:

$$S = S_0(e^{-bD}) \tag{1.8}$$

The b value measures movement in units of s/mm^2. Generally, a shorter b-value will create a signal dominated by particles moving long distances, and is useful for the study of vas-

culature. A longer b-value will capture signal from particles traveling over small distances, and can show differences in tissue microstructure and cell density.

Interpreting the difference in signal in the context of current prostate MRI requires two more steps. First, because diffusion gradients are directional, images are obtained in—usually three or six—different directions and combined to form a trace image:

$$S_{DWI} = S_0(e^{-b\frac{(D_x+D_y+D_z)}{3}}) \tag{1.9}$$

The trace consolidates the directional diffusion of molecules in a tissue into a single number. However, because diffusion measures dephasing, the resulting signal can reflect the inherent T_2-weighting of the spin-echo sequence, a phenomenon known as T_2-shine-through [25]. To remove the effect of this simultaneous T_2 decay, the trace image is divided by a reference image with similar echo timing and a b-value of 0 s/mm^2, with the natural logarithm correcting for exponential decay. The resulting apparent diffusion coefficient (ADC) is a directionless metric of diffusion without the effects of T_2-weighting:

$$ADC = -\frac{1}{b}ln(\frac{S_{DWI}}{S_0}) \tag{1.10}$$

The glandular structure of the normal peripheral zone of the prostate compared to the shrunken glands or tightly packed cancerous tissue defines a well-established contrast between healthy and tumor tissue on DWI and the corresponding ADC maps [33]. Perhaps not surprisingly, DWI has been shown to increase the sensitivity and specificity of multiparametric MR imaging for the detection of prostate cancer [22]. Some studies have shown improvement in the assessment of tumor aggressiveness when combined with conventional

T_2-weighted imaging, with an inverse relationship between the ADC map intensity and the Gleason score [34]. A threshold of approximately 850 x 10^6 mm^2/s has been used to distinguish between low- and high-grade tumors [35]. However, substantial overlap of ADC values is commonly seen between cancer and confounders like inflammation and benign prostatic hyperplasia (BPH), and variability across the various imaging platforms due to different acquisition parameters prevent DWI metrics from being recommended bases for aggressiveness and have not been accepted into the PI-RADS v2 standard [13].

For prostate cancer detection on 3T scanners, the b-values are generally divided into mid (between 500 and 800 s/mm^2) and high (between 1000 and 2500 s/mm^2) (Figure 1.1) [36], where using a lower b-value emphasizes extracellular effects in the resulting ADC maps, and using a high b-value emphasizes intracellular motion. Limits in gradient hardware on older magnets may exclude b-values above 1000 s/mm^2. Recently, it has become popular to utilize more than one b-value for the assessment of prostate cancer. Imaging with a mid-range b-value will normally have a greater SNR, which can result in finer resolution and a decreased number of signal averages per image. However, a high b-value acquisition reduces the signal from normal prostatic tissue and vasculature, increasing the sensitivity to abnormal cellular environments [37]. One method of gaining the advantage of contrast of a high b-value while still having the high SNR and fine resolution of a lower b-value acquisition is to extrapolate and compute the theoretical image output for higher b-values. These images show higher SNR than traditional DWI collected with the equivalent high b-values and can be utilized on older 1.5T scanners where gradient hardware may not allow acquisition with high b-values

[38].

In addition to more heavily diffusion-weighted images, a low b-value image is acquired with a b-value in the range of 0–100 s/mm^2. This image serves as a reference, to fit a slope to the signal per b-value per direction, which is combined to define the ADC map. The lower b-values are also used because they remove the effect of perfusion on the resulting ADC map.

In order to easily associate structural T_2-weighted images with functional DWI data, DWI should be performed with the same or similar slice thickness and acquisition prescription to high-resolution T_2-weighed imaging. DWI can be performed immediately after T_2-weighted imaging to increase structural similarity.

DWI is heavily affected by susceptibility artifacts, which increase in magnitude with higher field strength [39]. Images acquired with EPI, in particular, suffer from severe susceptibility artifact at the interfaces of tissue with air, blood, or fecal matter in the rectum. These artifacts are important because they present at the border of the rectum and affect the peripheral zone of the prostate, where 70% of cancers are located [40]. Performing a rectal enema before the exam reduces susceptibility artifact from air or fecal matter in the rectum [41]. A promising recent development for artifact reduction is reduced Field-of-View imaging, which has been shown to improve image quality and contrast between tumor and healthy tissue, as well as to decrease susceptibility artifact in prostate DWI [42] (Fig. 1.7). This technique will be discussed in detail in Chapter 2.

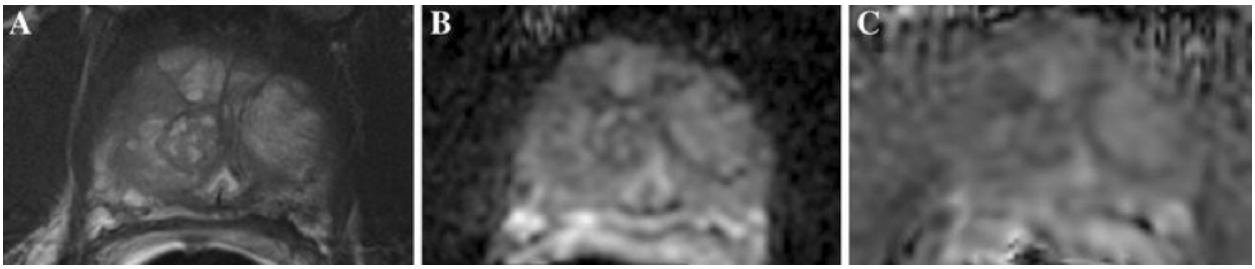

Figure 1.7: An untreated 74-year-old man with biopsied Gleason 3+3 prostate cancer and serum PSA of 6.85 ng/mL. An oblique axial **A** T_2-weighted 2D FSE anatomic image, **B** rFOV ADC map, and **C** full FOV ADC map show the advantages of the rFOV method for distinguishing boundaries of the prostate and BPH nodules within the prostate. We also see susceptibility artifact from fecal matter or air in the rectum, which significantly blurs the rectal wall on **C** and less so on **B**.

1.4 Dynamic Contrast-enhanced Imaging

Dynamic contrast-enhanced imaging follows the time course of tissue enhancement before, during, and after injection of a contrast agent to evaluate the properties of tissue microstructure and neovascularity. The most common MR contrast agents are chelated forms of a gadolinium ion [43]. Gadolinium has several important properties that make it an ideal magnetic contrast agent, most importantly that it is biologically inert and paramagnetic, and it maintains these properties when chelated.

The gadolinium ion's signal isn't acquired directly; rather it's the effect of gadolinium's magnetic moment on the surrounding hydrogen atoms that we measure [25]. The net magnetic moment of gadolinium in a tissue is proportional to the number of chelated gadolinium ions that have permeated the tissue. This net magnetic moment aligns with the main magnetic field $B_0\mathbf{k}$, strengthening the local B_0 field and shortening the T_1 relaxation time of surrounding hydrogen ions. Dynamic T_1-weighted images reflect a difference in signal inten-

sity in regions of similar tissues with different amounts of injected gadolinium. Gadolinium is therefore used as a perfusion agent, and is popular in cancer diagnostics to measure tumor angiogenesis.

Prostate cancer, specifically, brings about numerous changes in the cellular structure of the tissues, resulting in tissue alterations that can be measured with injected contrast. It is believed that MR contrast agents do not reach the lumen of the healthy glandular tissues [44]. Conversely, prostate cancer is marked by the loss of the basement membrane outside the glandular epithelial cells, which allows the contrast to enter the glands, resulting in a greater and faster tissue enhancement. In addition to continuing alterations in tissue microstructure, prostate cancer progression is also associated with neoangiogenesis [45]. The rapid growth and division of tumor vasculature result in disorganized, irregularly shaped, immature vessels [46]. DCE takes advantage of the unique characteristics associated with the abnormal tumor vasculature to assess aggressiveness of the disease. The usefulness of DCE in detecting, localizing, and staging prostate cancer is well documented in literature [47]. Additionally, several studies have reported promising findings on the utility of DCE parameters in discriminating prostate cancer based on aggressiveness of the disease [48]. However, these results are often confounded by the presence of prostatitis in the peripheral zone or by mixed BPH nodules in the central gland [1] [4].

DCE imaging is often done with a 3D Fast Spoiled Gradient Echo (3D-FSPGR) pulse sequence. T_1-weighted images are collected before, during, and after administration of a contrast agent. A DCE scan is often preceded by a T_1 mapping, a measurement of the native

tissue relaxation time ($T_{1,0}$) obtained using a series of volume acquisitions with variable flip angle values. Once the native T_1 mapping is complete, several pre-contrast dynamic T_1-weighted volumes are acquired to establish a baseline. The contrast agent is administered as an intravenous bolus at a rate of 2-4 ml/s followed by a 20-mL saline flush using a power injector. To ensure patient safety, patient's kidney function should be evaluated prior to contrast injection. Estimated glomerular filtration rate (eGFR) based on the blood creatinine levels are often used as indicators of kidney health. Once injected, the contrast agent does not penetrate the healthy prostate glands but collects in the extravascular extracellular space (EES), where it serves to shorten local relaxation times, producing high signal intensity on T_1-weighted images.

DCE-MRI studies typically utilize weight-adjusted (0.1 mmol/kg of body weight) paramagnetic gadolinium chelate contrast agents. There are several agents approved by the United States Food and Drug Administration, including gadopentetate dimeglumine (Magnevist), gadobutrol (Gadovist), or gadodiamide (Omniscan) [43]. Aiming for a reasonable spatiotemporal resolution, a five-minute DCE acquisition yields dynamic imaging with a temporal resolution in the range of 3-10 s, a spatial resolution in the range of 0.7x0.7 mm to 1.9x1.9 mm with a slice thickness of 3-4 mm [30]. Compressed sensing techniques can improve spatiotemporal resolution or increase the coverage in DCE acquisitions. Recently, Rosenkrantz et al. reported the use of a high-spatiotemporal resolution DCE technique GRASP (Golden-angle Radial Sparse Parallel) imaging, which allows for image acquisition with spatial resolution of 1.1x1.1x3.0 mm and temporal resolution of 2.3 s [49].

Tissue enhancement observed during DCE can be interpreted either by visually inspecting the raw images (qualitative approach) or by using semi-quantitative or quantitative methods [50]. The qualitative analysis of the DCE images [51] is based on the premise that the blood vessels recruited by the prostate tumors are leaky [52]. When the contrast is injected, the cancerous tissues demonstrate early and rapid enhancement followed by a quick washout, which is noticeably different from a slow and steady enhancement observed for normal tissues. An observer may evaluate regions of interest within the prostate by categorizing the overall enhancement as 1) persistent—a steady enhancement, usually indicative of benign pathology, 2) plateau—the initial uptake is followed by a constant enhancement, slightly suspicious for malignancy, and 3) washout—a sharp uptake is followed by a steep washout, strongly suspicion for malignancy (Figure 1.8).

While the qualitative approach is quick and intuitive, it fails to comprehensively assess heterogeneous tissues and is inherently subjective and difficult to standardize among imaging centers. Semi-quantitative analysis characterizes the enhancement curve on a voxel by voxel basis by calculating curve parameters such as maximum enhancement slope (Figure 1.1), time to peak, peak enhancement, washout slope, and area under the curve [48]. Although this approach is extensively used in the assessment of DCE-MRI, the semi-quantitative parameters provide little physiologic insight into behavior of the tumor vessels and the usefulness of the computed metrics can be limited when comparing data across different imaging protocols. Normalization to muscle has been suggested to aid in generalization of semi-quantitative parameters [44].

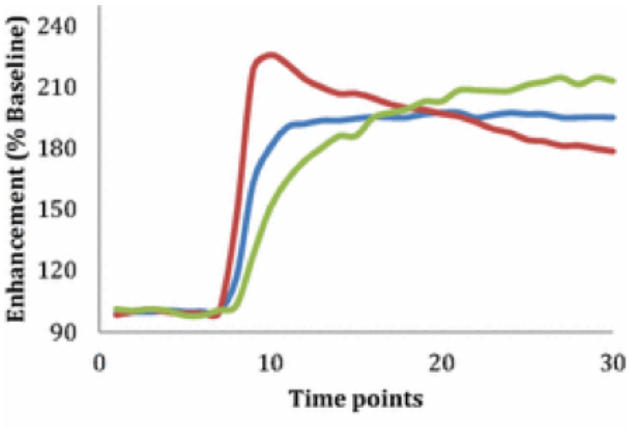

Figure 1.8: Three main types of overall enhancement seen in prostate tissues: persistent enhancement, typically indicative of benign pathology (*green*); plateau, slightly suspicious for malignancy (*blue*); and washout, strongly suspicious for malignancy (*red*).

The final approach to analyzing DCE images aims to estimate physiologically interpretable, kinetic parameters by fitting pharmacokinetic models to the enhancement curves [53] [54]. The most common is the two-compartment model, where the two compartments are the plasma space of the vasculature and the interstitial space between the prostate cells. The two main parameters derived from such models are K^{trans} (the volume transfer constant between plasma and extracellular space, expressed in units of min^{-1}) and v_e (the fractional volume of extracellular space per unit volume of tissue) [55]. While K^{trans} maps offer diagnostically valuable information, acquiring stable measurements from quantitative analysis remains a challenge. Quantitative methods are affected by a number of variables such as changes in cardiac output, accurate tissue T_1 and arterial input function (AIF) measurements, as well as the underlying assumptions made by the software packages. Accuracy of T_1 measurements is greatly aided by T_1 mapping [56]. Ideally, the AIF (the concentration of the contrast agent in the feeding blood supply) is measured for each individual patient

in the femoral artery [57]. Unfortunately, in a clinical setting, the required temporal resolution may be difficult to achieve. Finally, there are several open-source and commercially available software packages for both clinical and preclinical quantitative DCE analyses [58] [59] [60]. However, few studies have been done to assess reproducibility of pharmacokinetic measurements obtained with different software packages.

The second version of PI-RADS highlights the fact that DCE-MRI can be and is most widely assessed based on direct visualization of the raw data; optional tools, e.g., parametric maps and compartmental models, can be used to assist in diagnosis, but findings should always be confirmed on source images [13]. PI-RADS v2 characterizes a positive finding on DCE-MRI as a lesion with focal enhancement, earlier or contemporaneous with enhancement of adjacent normal tissues, and that corresponds to a suspicious finding on T_2- or diffusion-weighted MR images.

1.5 ^{1}H MR Spectroscopic Imaging

Benign and malignant tissues can also be differentiated based on the metabolic changes associated with prostate cancer [61], and proton magnetic resonance spectroscopic imaging (^{1}H-MRSI) has been established as a powerful technique for assessing in vivo cellular metabolism. MRSI combines the spatial localization of imaging with traditional nuclear magnetic resonance (NMR) to discern relative metabolite abundance within tissues. The result can be viewed as a matrix of NMR spectra, or as maps of relative metabolite abundance as in the choline map in Figure 1.1.

The ability of NMR to distinguish metabolites in a tissue is based on the small differences in magnetic microenvironment experienced by protons in different molecular configurations. The electron cloud surrounding each proton creates a small shield from the main magnetic field B_0, and the small changes in the 'effective' B field of each proton results in small differences in resonant frequency, a phenomenon known as chemical shift. The chemical shift of each proton is measured by its difference in frequency from a reference molecule, usually the stable and well-shielded trimethylsilane (TMS), as describe by Eqn 1.11.

$$\delta = \frac{f_{sample} - f_{reference}}{f_{reference}} \tag{1.11}$$

The chemical shift is a dimensionless constant dependent on nucleus and molecular configuration, typically measured in parts per million (PPM), which simplifies language when accounting for the six orders of magnitude between precession (MHz) and chemical shifts (Hz). PPM is also independent of field strength.

Normal prostatic glandular epithelial cells produce and secrete high levels of citrate (2.5–2.7 ppm) (Fig 1.9) [62]. Prostate cancer disrupts the epithelial tissues and triggers a metabolic shift from citrate production to citrate oxidation; the overall effect is a substantial reduction in citrate levels in malignant prostate tissues [63]. Furthermore, increased cell density and elevated cell membrane turnover lead to increased levels of choline (3.21 ppm) in prostate cancer [64]. Creatine (3.02 ppm) is another metabolite of interest; it is maintained at a relatively constant level in both healthy and malignant prostatic tissues and serves as an internal reference. Lastly, some groups found it informative to track metabolic changes associated with polyamine [61]. Polyamines (especially spermine) are found in healthy prostate

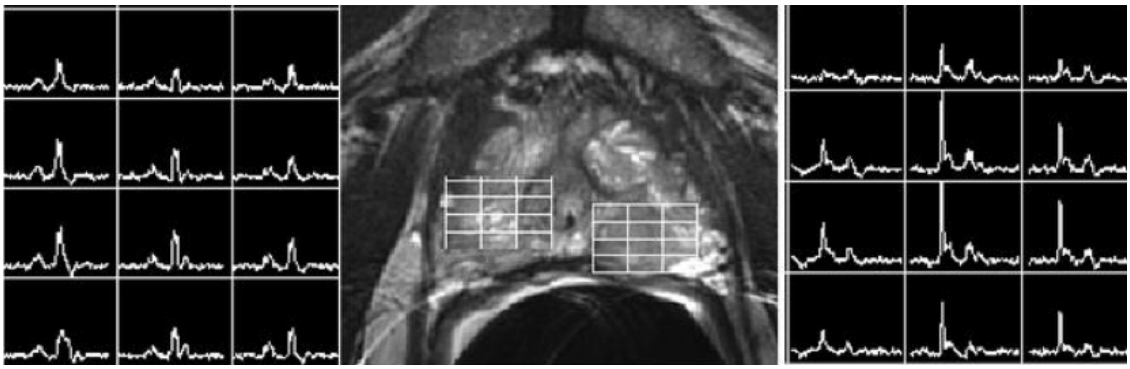

Figure 1.9: An untreated 78-year-old man with serum PSA of 9.8 ng/mL. MRSI demonstrating highly elevated choline (*right panel*) in the *left apex*, drastically different from the contralateral healthy tissues (*left panel*) that demonstrate high citrate signal without elevated choline. Subsequent TRUS–MRI fusion-guided biopsy revealed a Gleason 4+3 lesion in the *left apex*.

epithelial cells, and similar to citrate, their levels are dramatically reduced in prostate cancer [65].

Due to the multifocal nature of prostate cancer, a high-resolution metabolic mapping of the entire prostate is required for accurate cancer localization and diagnosis. The ^{1}H-MRSI acquisition has evolved from single-voxel spectroscopy to 3D ^{1}H-MRSI that is typically acquired using phase encoding in all three directions, but is time consuming. Improvements in pulse sequence design have enabled the acquisition of metabolic information from the entire prostate at high resolution within less than 10 min with voxel sizes ranging from 0.2 to 0.5 cm^3, making ^{1}H-MRSI a clinically feasible technique [66]. These include using flyback echo-planar readout gradients to improve efficiency and robustness to errors and non-uniform undersampling, and compressed sensing to accelerate the acquisition [67]. A number of techniques have been used to reduce the negative effects of periprostatic fat, including outer volume saturation (OVS) with very selective suppression (VSS) pulses [68], band-selective

inversion with gradient dephasing (BASING) [69], and spectral-spatial radiofrequency pulses [70].

The ^{1}H-MRSI sequence is usually prescribed off the axial T_2-weighted MR images with a volume selected to maximally cover the prostate while excluding the seminal vesicles, periprostatic fat, and as much of the rectum as possible. Standard post-processing involves zero-filling, apodization using Gaussian or Lorentzian filtering, and Fourier transform of the free induction decay signal, as well as baseline and phase corrections [6].

Interpretation of ^{1}H-MRSI data is often done on a voxel-by-voxel basis, which can be time consuming and introduce interobserver variability. An alternative approach to review these metabolites is to observe peak area ratios, such as the choline + creatine to citrate ratio within each voxel; choline and creatine are typically combined due to signal overlap. In 2004, Jung et al. proposed a standardized scoring system for peripheral zone tissues based on metabolic data, ranging from 1 (definitely normal) to 5 (definitely cancer) [71]. And in 2007, Futterer et al. introduced standardized thresholds for differentiation of benign and malignant tissues in the peripheral zone and central gland of the prostate [72]. Several studies reported significant correlations between peak area ratios and Gleason scores [73] [74]; yet, interpretation can be hindered by choline contamination from the seminal vesicles or urethra [75] or by prostatitis [76], which can result in false positive findings.

It is also important to note that the data of some studies were unfavorable to the clinical usefulness of ^{1}H-MRSI, more notoriously those of the ACRIN 6659 study published by Weinreb et al. that found no incremental benefit for ^{1}H-MRSI compared with MRI alone

in sextant tumor localization [15]. Based on such data, and possibly on the complexity of imaging acquisition and interpretation, ^{1}H-MRSI, which was an optional tool in the initial version of PI-RADS, no longer influences the assessment of lesions in PI-RADS v2 [13].

1.6 ^{13}C MR Spectroscopic Imaging

Imaging with an injectable, radioactively labeled accumulating agent as is done in ^{18}F - fluorodeoxyglucose Positron Emission Tomography (PET) imaging can eliminate the background signal that often hampers the specificity of ^{1}H-MRSI. There is considerable interest in the development of injectable, non-radioactive, MR-based agents that could probe metabolic changes in tissue without the background signal inherent to proton imaging, specifically agents whose natural abundance is less ubiquitous in the body.

While many probes have been developed in recent years, labeling with carbon-13 (^{13}C), i.e. replacing ^{12}C (98.9% natural abundance) with MR-sensitive ^{13}C (1.1% natural abundance), has the potential to detect and track the metabolism of a large number of organic metabolic substrates, like glucose and glutamine. In cancer imaging, ^{13}C-labeled pyruvate can provide a measure of the Warburg effect: that after glycolysis cancerous cells tend to favor lactic acid fermentation by lactate dehydrogenase (LDH) over the more common and energy-efficient oxidative phosphorylation [77]. Preference for either metabolic pathway can therefore be studied by injecting ^{13}C labeled pyruvate, the end product of glycolysis, and observing the amount of resulting ^{13}C labeled lactic acid.

There are several practical hurdles to ^{13}C imaging: frequency-specific hardware, and low

sensitivity. ^{13}C has a gyromagnetic ratio of 6.7x10^7 rad/T/s [78], almost exactly 1/4 that of ^{1}H, so dedicated transmit and receive hardware tuned to the resonant frequency of ^{13}C must be available to perform carbon imaging. Because high-resolution anatomic proton imaging is often desired along with functional carbon, dual-tuned RF coils are common. Multinuclear RF coil design is discussed in detail in Chapter 4. Pulse sequences must also be adjusted, specifically to account for the differences in power absorption and relaxation times.

The low natural abundance of ^{13}C has the major benefit of reducing background signal; however the low sensitivity creates low signal of an injected probe as well. ^{13}C imaging over many hours to compensate for this low sensitivity is common in *ex vivo* experiments, but impractical for the clinic, where sufficient signal needs to be generated before the probe is cleared from the system. A practical solution is to overcome the natural, thermal polarization level of the sample determined by the Boltzmann distribution:

$$\frac{N_+}{N_-} = exp^{\frac{-\Delta E}{kT}} \tag{1.12}$$

Where N+/N- is the ratio of parallel to anti-parallel alignments, ΔE is the difference in energy level, K is the Boltzmann constant and T is temperature. Close to absolute zero, spins overwhelmingly prefer parallel alignment to the main magnetic field. However as increasing temperature increases the energy in the environment, the conglomerate effects of random motion tend to equilibrate preference in alignment, and decrease the net magnetization vector. Creating nonthermal polarization levels in liquid solutions at body temperature is done using a process called dynamic nuclear polarization (DNP), which can increase the resulting signal-to-noise ratio of an injectable probe by over 10,000-fold [79].

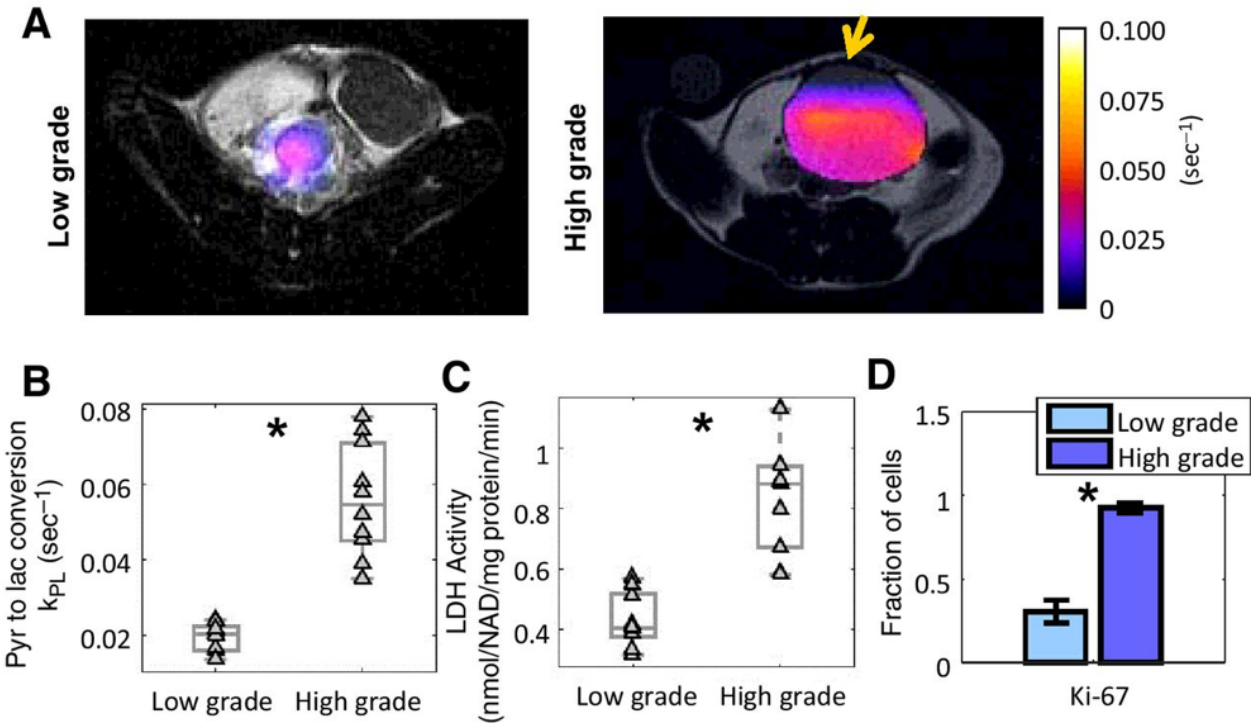

Figure 1.10: **A** Representative calculated pyruvate-to-lactate flux (k_{PL}) images overlaid on corresponding T_2-FSE reference images from a low-grade (left) and a high-grade (right) TRAMP tumor. At pathology, a region of necrosis was observed in the anterior aspect of the tumor (red arrow). **B** Box plots showing individual (diamonds), median, and standard deviation k_{PL} flux measurements in the 9 low-grade and 10 high-grade TRAMP tumors. **C** LDH activities for the same TRAMP tumors. **D** A bar plot showing the fraction of cells staining positive for Ki-67 (mean $\pm$ SE) $\star$ significantly different; $p<0.001$.

This hyperpolarized ^{13}C probe can be imaged *in vivo* to track the metabolic conversions of the injected substrate in real time, a diagnostic feature without equal in traditional MR or radiologic imaging [80]. In murine models, the measurement of the Warburg effect using hyperpolarized [1-^{13}C]pyruvate correlates with traditional histpathological staging of disease aggressiveness (Figure 1.10) [81] [82]. Chapter 5 explores current advances in [1-^{13}C]pyruvate in human prostate cancer in detail.

1.7 Conclusion

Use of mpMRI exams for the staging and improved characterization of prostate cancer has become prominent at medical centers around the world [22] [83] [84] and is likely to continue expanding into increasing modalities in the age of precision medicine. However, the mpMRI of the prostate has not gained the same level of acceptance of other imaging tests, at least in part due to the lack of standardization and inadequate patient preparation. Discrepancies in pulse sequence design can create exams vulnerable to artifact, and sequence design is limited by currently available hardware. Even in state-of-the-art imaging, differentiating between similar appearing tissues is challenging. Benign conditions like chronic inflammation can masquerade as low-grade cancer, and cancer aggressiveness cannot be measured by the current mpMRI. In this work, we provide solutions to the above concerns through innovations in pulse sequence design and hardware, novel analytic methods, and clinical application of hyperpolarized ^{13}C-MRSI.

Finally, regardless of the magnet strength, the use of an endorectal coil, or the details of the imaging protocol, patient preparation is essential to acquiring the highest quality images while maintaining maximal patient comfort and compliance. Equally important in providing the best imaging exam for patient diagnosis is the communication between primary physicians, radiologists, researchers, and staff.

Chapter 2

A Reduced-FOV Excitation Decreases Susceptibility Artifact in Diffusion-weighted MRI for Prostate Cancer Detection

Abstract

The purpose of this study was to determine if image distortion is less in prostate MR apparent diffusion coefficient (ADC) maps generated from a reduced-field-of-view (rFOV) diffusion-weighted-imaging (DWI) technique than from a conventional DWI sequence (FULL), and to determine if the rFOV ADC tumor contrast is as high as or better than that of the FULL sequence. Fifty patients underwent a 3T MRI exam. FULL and rFOV (utilizing a 2D, echo-planar, rectangularly-selective RF pulse) sequences were acquired using b=600 and 0 s/mm^2. Distortion was visually scored 0–4 by three independent observers and quantitatively measured using the difference in rectal wall curvature between the ADC maps and T_2-weighted images. Distortion scores were lower with the rFOV sequence (p=0.012, Wilcoxon signed-rank test, n=50), and difference in distortion scores did not differ signifi-

cantly among observers (p=0.99, Kruskal-Wallis test). The difference in rectal curvature was less with rFOV ADC maps (26±10%) than FULL ADC maps (34±13%) (p=0.011, student's t-test). In seventeen patients with untreated, biopsy confirmed prostate cancer, the rFOV sequence afforded significantly higher ADC tumor contrast (44.0%) than the FULL sequence (35.9%), (p=0.0012, student's t-test). The rFOV sequence yielded significantly decreased susceptibility artifact and significantly higher contrast between tumor and healthy tissue.

2.1 Introduction

Diffusion-weighted imaging (DWI) increases both sensitivity and specificity in prostate cancer detection in multiparametric MR studies [21]. DWI has also been shown to improve the assessment of tumor aggressiveness when combined with conventional T_2-weighted imaging, with an inverse relationship between the apparent diffusion coefficient (ADC) map intensity and Gleason score [34]. DWI typically uses the echo-planar imaging (EPI) technique to decrease scan time. However, images acquired with EPI suffer from severe susceptibility artifact at the interfaces of tissue with air, blood, or fecal matter in the rectum. These artifacts are of particular importance because they present at the border of the rectum and the peripheral zone of the prostate, where 70% of prostate cancers are located [40].

In this work, we have utilized a reduced-field-of-view (rFOV) acquisition scheme for prostate DWI that employs a 90° 2D spatially-selective, echo-planar RF pulse to excite a limited extent of the Field-of-View (FOV) in the phase encoding direction [85]. This enables a higher spatial resolution to be achieved in the phase encoding direction than in

conventional DWI with a shorter echo-train length, and without obvious aliasing artifacts. The reduced echo-train length can potentially reduce prostate image distortions induced by magnetic-susceptibility differences within the FOV [85]. Additionally, this pulse is designed so that the excited fat profile and the excited water profile are displaced in volume in the slice-selective direction, and only the on-resonance water profile can be selected by the subsequent refocusing pulse. This displacement in volume (Δd_{cs}) is dependent on the chemical shift between fat and water (f_{cs}), as well as the number of blips (N_{blips}), the extent of k-space traversed per blip (k_{blip}), and the duration of the gradient lobe (T_{fast}). This could potentially provide a robust method of periprostatic fat suppression in prostate DWI images.

The aim of this study was to determine if image distortion is less in prostate ADC maps generated from the rFOV technique than from a conventional DWI sequence (FULL) and to determine if the rFOV ADC contrast between tumors and healthy-appearing tissue within subjects is as high as or better than that of the FULL sequence.

2.2 Materials and Methods

This prospective study was approved by our institutional review board and was compliant with the Health Insurance Portability and Accountability Act. Written, informed consent was obtained from all participants. Fifty patients receiving MR examinations of the prostate were studied between September of 2011 and January of 2013. Patients presented with suspected prostate cancer, as indicated by either elevated levels of serum prostate-specific antigen (PSA) (median=5, range 0.10–291 ng/mL), biopsy-proven prostate cancer, or both.

The patients' mean age was 64.2 years, ranging from 47 to 81 years old. Two patients had undergone a partial radical prostatectomy, two patients had undergone hormone therapies, two patients had received external beam radiation therapy (EBRT), four patients had radiation seed implants, and one patient had received hormone therapy and EBRT. Data from the eleven patients having undergone any form of treatment were not used in assessment of contrast; however these data were included in visual and quantitative assessments of distortion.

Thirty-nine of the fifty patients studied were untreated and considered for inclusion in the study of contrast. Of these patients, ten were scanned with inconsistent MR parameters during initial trials of this study and were not considered for the studies of ADC values. The ADC value in presumed healthy peripheral zone tissue was assessed in the resulting twenty-nine patients. Within this group of twenty-nine patients, twelve had no positive biopsy on record. The seventeen remaining patients' data were used to calculate the contrast between tumor and healthy tissue for both FULL and rFOV sequences. Fourteen of these patients exhibited a Gleason score of 3+3. One patient each presented with Gleason scores of 3+4, 3+5, and 4+3.

All images were acquired using a 3T MR scanner (GE Healthcare, Waukesha, WI, USA) equipped with an eight-channel phased-array for the pelvis and an endorectal coil encased in a balloon probe (Bayer Healthcare, Warrendale, Pa, USA). A perfluorocarbon compound (3M, St. Paul, MN, USA) was used to inflate the balloon probe to reduce artifacts due to susceptibility [17].

Anatomic imaging was provided by oblique axial T_2-weighted images (512x512, TR/TE = 6350/103 ms). FULL (128x128, FOV=24cm x 24cm, NEX=4, TR/TE = 4000/78–90ms, 2:44 minutes) and rFOV (128x64, FOV=18cm x 9cm (n=37) or 24cm x 12cm (n=13), NEX=6, TR/TE = 4000/78–90ms, 2:52 minutes) DWI sequences were acquired using a 2D single-shot EPI (ss-EPI) spin-echo sequence with receiver bandwidth = 250kHz, b = 600 and 0 s/mm^2, and 3mm slices (n=37) or between 3mm and 4 mm slices (n=13). Parallel imaging was used in the FULL sequence, with an acceleration factor of 2. The rFOV acquisition employed a 2D spatially-selective echo-planar RF pulse in place of conventional excitation in the ss-EPI sequence. The RF envelope of the 2D echo-planar pulse ($\sim$18 ms duration) is minimum phase by design so the echo time occurs toward the end of the pulse. Because of this, and the fact that the spacing between the 90° pulse and the following 180° pulse is dominated by the diffusion weighting time, the RF pulse did not increase the echo time compared to the conventional sequence. The time-bandwidth of the RF envelope (slice direction) was relatively small, therefore the slice dephasing from the non-linear phase excitation was relatively benign. The TE varied among patients due to changes in obliquity of the prostate and therefore, the scan prescription. The phase-encoding direction, and consequently the reduced-FOV axis for the rFOV DWI scan, was in the oblique anterior-posterior direction. The DWI images were obtained with slice locations and obliquity identical to the oblique axial T_2-weighted images. Thirteen patients were scanned with the rFOV sequence acquired with FOV = 24cm x 12cm and the slice thickness greater than 3 mm during initial testing. These patients' data, acquired with inconsistent MR parameters, were used in the quantitative

and visual assessments of distortion. Although ten of the thirteen patients presented with radiologist-identified tumor regions, the data were not used in the study of contrast to avoid any bias due to different partial-voluming effects. Under the assumption that prostate tissue is isotropic, ADC maps were computed from the combined DWI and T_2-weighted reference images using Eqn 1.10.

The incidence and severity of visually assessed distortion was characterized by changes in the contour of the prostate adjacent to the rectal wall. The rFOV and FULL ADC maps were scored 0 for no distortion, and 1–4 for increasing distortion. A distortion score of 0 reflects no visible change in the boundary between prostate and rectum in comparison to a T_2-weighted image. A distortion score of 1 reflects slight disturbances in the boundary region, whereas a distortion score of 2 is appropriate for more extensive disturbances in the boundary, or specific regions of high susceptibility artifact. A distortion score of 3 denotes a consistently distorted prostatic boundary, with some areas in the prostate unusable due to susceptibility artifact, and a distortion score of 4 is used to describe a prostate image that is entirely unusable due to susceptibility artifact. Examples of each distortion score are shown in Figure 2.1. All distortion scores were assigned by three independent observers to control for inter-observer variability. T_2-weighted oblique axial images were used as a reference of no distortion.

A quantitative method of measuring distortion was also performed by comparing the radii of circles that reflect rectal wall curvature adjacent to the prostate. The inflated endorectal probe creates a reliably circular rectal shape on oblique axial images, and deviation from

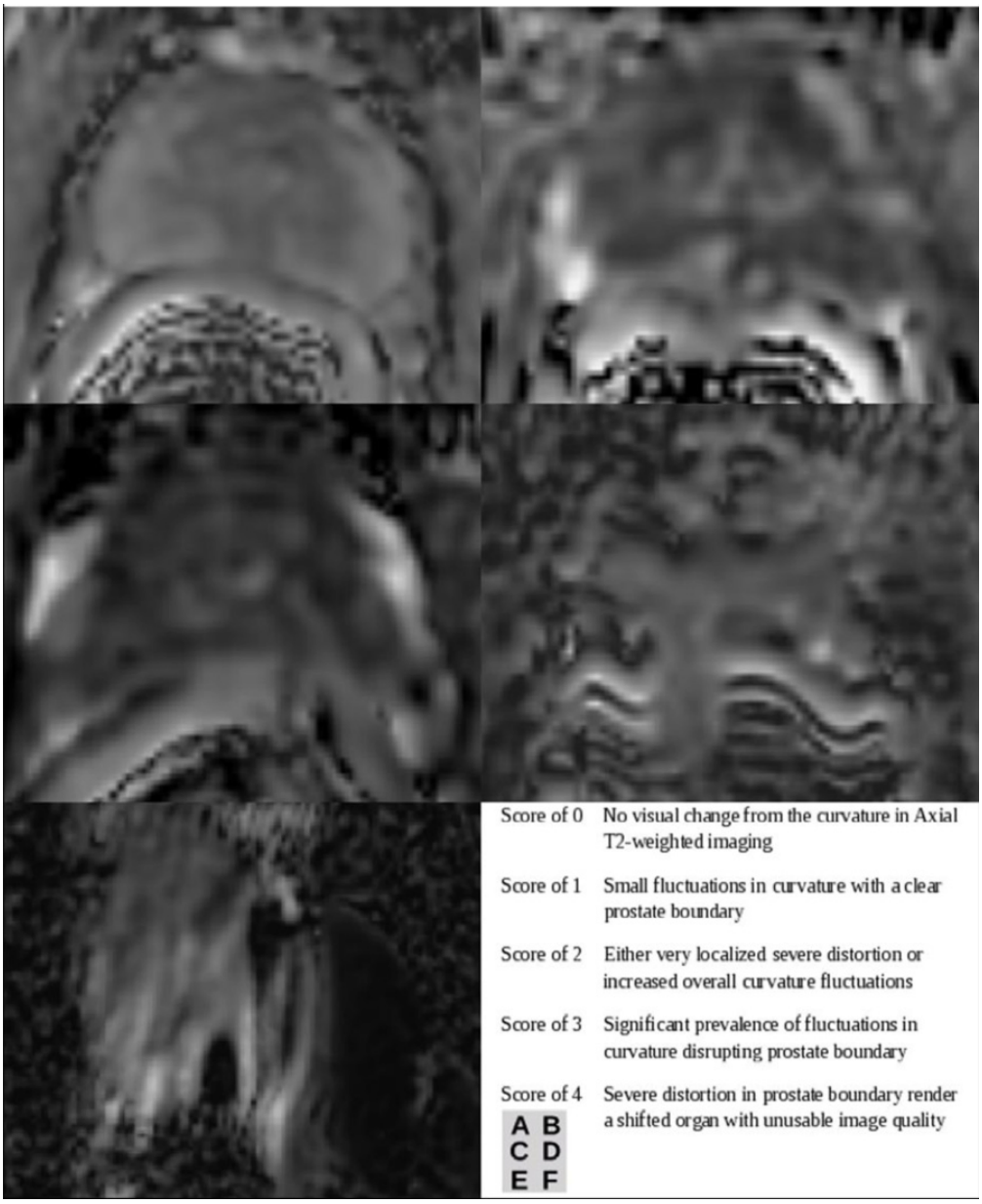

Figure 2.1: Distortion scores from sample patients showing **A** score of 0, **B** score of 1, **C** score of 2, **D** score of 3, **E** score of 4, and **F** a guideline of visual score interpretation. Please note that **E** contains artifact that has rotated the prostate signal, rendering spatial localization unusable.

the circular pattern is a typical sign of susceptibility-induced distortion. On FULL, rFOV, and T_2-weighted images, the radius of the largest circle tracing the rectum adjacent to the prostate, and without covering the rectal wall, was recorded on three slices. These three selected slices were equally spaced throughout the prostate—in the base, midgland, and apex—and matched in location among image types. The percent difference of the rectal wall radius on the FULL and rFOV ADC maps from the corresponding radius on the T_2-weighted image was calculated for each of the three slices. These values were averaged within each patient to create a quantitative distortion measure of each DWI sequence for each patient.

Regions of interest (ROIs) were placed in areas of presumed healthy peripheral zone tissue in the group evaluated for assessment of healthy ADC values. ROIs were also placed in areas of reduced ADC corresponding to suspected tumor regions and in areas of presumed healthy contralateral tissue in each patient included in the study of contrast. Suspected tumor regions were identified as regions of both positive biopsy findings and radiologist-identified tumor in the MR exam. For patients with more than one biopsy-proven tumor region, the most aggressive tumor region was used to calculate contrast. For a given patient, all tumor ROIs and control ROIs were the same size within one pixel, and ranged between 0.143 and 0.642 cm^2. ROIs for all patients were drawn by a single researcher to avoid inter-observer variability. Tumor contrast was calculated using Eqn 2.1:

$$Contrast = \left| \frac{ADC_{tumor} - ADC_{healthy}}{ADC_{healthy}} \right| \tag{2.1}$$

Statistical analyses were performed using JMP V10 software (SAS Institute, Cary, NC, USA). A Wilcoxon signed-rank test was performed to assess significant differences between FULL and rFOV distortion scores for each observer. The difference in distortion scores between FULL and rFOV images for each patient was compared among the three observers using a Kruskal-Wallis test. As a quantitative distortion assessment, differences in rectal curvature were tested by student's t-tests. Differences in tumor, healthy tissue, and tumor-to-healthy-tissue contrast in FULL and rFOV scans were also tested for significance using student's t-tests. Tests for normalcy were done using Shapiro-Wilk tests.

2.3 Results

Forty-nine of the fifty patients (98%) assessed showed rectal wall distortion interfering with the peripheral zone of the prostate on either the FULL or rFOV sequence by at least one observer. Examples of each distortion score are shown in Figure 2.1. Distortion scores were significantly reduced with the rFOV sequence (p=0.012 Wilcoxon signed-rank tests, n=50). Significance and average difference between sequences scored by each observer are shown in Table 2.1. The measured difference between FULL and rFOV distortion for a given patient did not vary significantly among observers (p=0.99, Kruskal-Wallis test, n=50 counts per group, 3 groups). The quantitative measure of distortion—the average percent difference in rectal wall radii between the ADC maps and the T_2-weighted images—also demonstrated lower distortion with the rFOV sequence than the FULL sequence. The average percent

Table 2.1: Wilcoxon signed-rank tests for difference in distortion scoring among patients show a significant decrease in observed distortion in ADC maps created from the reduced-Field-of-View (rFOV) sequence compared to the conventional (FULL) sequence for each observer (n=50). The average decrease in distortion score is similar for all observers, p=0.99, Kruskal-Wallis test, SD = standard deviation.

Observer	**rFOV Improvement**	**FULL - rFOV Difference (0-4 Scale) (Average ± SD)**
1	p=0.0063	0.56± 0.68
2	p=0.0117	0.48 ± 0.61
3	p=0.0010	0.52 ± 0.65

difference in rectal wall radii compared to T_2-weighted reference images was significantly lower for rFOV ADC maps (26 ± 10%) than for FULL ADC maps (34 ± 13%) (p=0.011, n=50, student's t-test).

A typical distortion case (Figure 2.2) shows a patient whose rectal wall signal has merged with the medial prostate peripheral zone signal, drastically distorting the entire prostate border and the periphery of the tumor on the FULL ADC in this region. This patient had an average distortion score of 2.67 on FULL ADC and 1.33 on rFOV ADC and a percent difference of rectal wall radii of 50.8% on FULL ADC and 21.8% on rFOV ADC. A second example case (Figure 2.3) shows either blood or fecal matter as dark lobules in the rectal wall with localized susceptibility artifact on the FULL ADC map demonstrating an average distortion score of 2.33. These distortions are greatly reduced on the rFOV ADC map, with an average distortion score of 1. The quantitative distortion measure yielded 20.1% percent difference on the FULL ADC map and 14.8% on the rFOV ADC map.

All reported ADC values (measured by units of 10^{-3}mm^2/s) and ADC contrast values were normally distributed across the studied population (Shapiro-Wilk Tests). The average

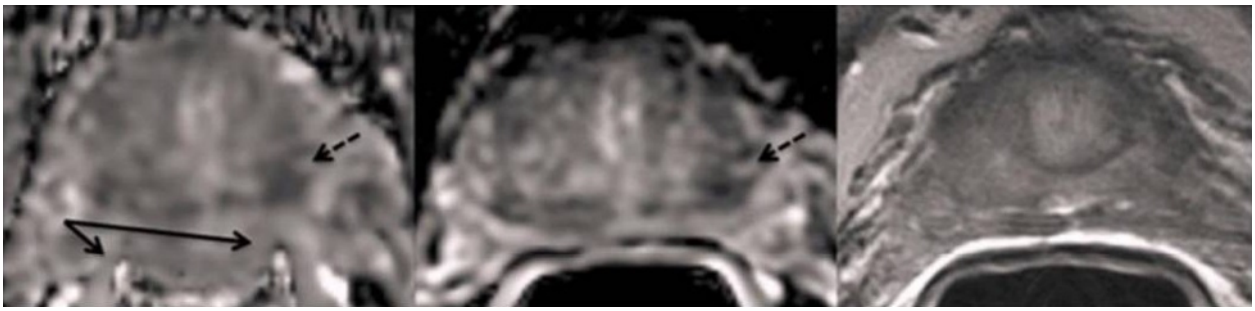

Figure 2.2: Oblique axial images of **A** FULL ADC map, **B** rFOV ADC map, and **C** T_2-weighted image for a patient with a visible tumor in the left peripheral zone (dashed arrows). The boundary of the rectum and peripheral zone (solid arrow) is distorted in the FULL image, less so in the rFOV image, and not at all in the T_2-weighted image. This is a patient with a negative biopsy and recently elevated PSA of 2.0, on active surveillance at the time of this scan.

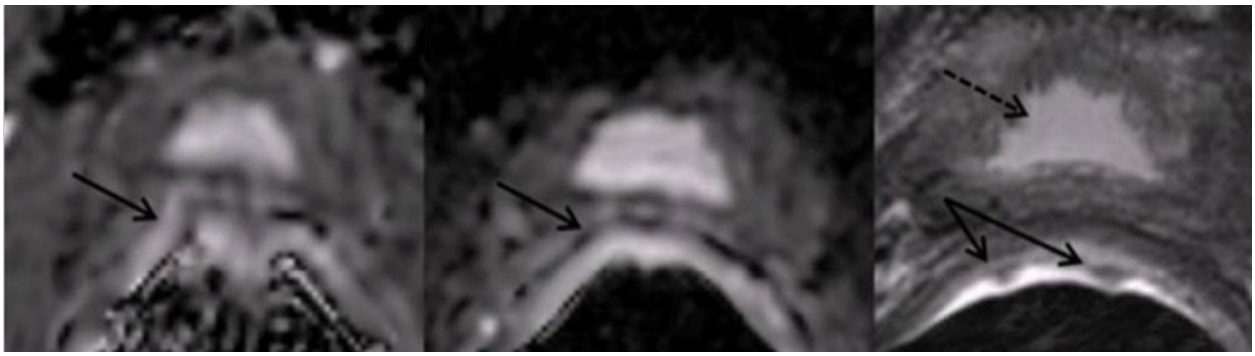

Figure 2.3: Oblique axial images of **A** FULL ADC map **B** rFOV ADC map and **C** T_2-weighted image at the base of the prostate near the bladder (dashed arrow) for a patient with blood or fecal artifact visible at the rectum/peripheral zone interface (solid arrows). This is a patient with a positive biopsy showing Gleason Score 3+3, on active surveillance at the time of this scan.

Table 2.2: Conventional full-Field-of-View sequence (FULL) and reduced-Field-of-View sequence (rFOV) apparent diffusion coefficient (ADC) values [10^{-3}mm^2/s] and contrast [%] for untreated patients with identified tumor (n=17). ADC values show no statistical difference between healthy tissue in tested sequences (p=0.978) and a trend towards lower ADC values in tumor regions using rFOV (p=0.0854).

Acquisition	Tumor ADC	Healthy Tissue ADC	Contrast (%)	Significance
Full	1.022 ± .185	1.620 ± .231	35.9 ± 13.2	
rFOV	0.952 ± .180	1.731 ± .230	44.0 ± 13.3	p=0.0012

ADC in healthy tissue for the twenty-nine untreated patients was 1.616 ± 0.399 for the FULL and 1.733 ± 0.223 for the rFOV, which were not significantly different, p=0.754.

For the seventeen patients included in the study of tumor contrast, the rFOV sequence provided significantly higher absolute value of the contrast between tumor and healthy tissue (average contrast = 44.0%) than the FULL sequence (average contrast = 35.9%) (p=0.0012, n=17, student's t-test). ADC values for tumor and healthy tissues with corresponding contrast values are listed in Table 2.2 for this group of patients. For the FULL and rFOV sequences, the ADC values in the healthy tissue of the untreated patients presenting with tumor were not significantly different (p=0.9782, n=17, student's t-test). However, the intensities of the tumor regions in the rFOV ADC maps had a trend to be lower than the corresponding tumor regions in the FULL ADC maps (p=0.0854, n=17, student's t-test).

2.4 Discussion

This study demonstrated that an alternate DWI acquisition scheme, based on using a pulse sequence with reduced-FOV excitation, provided significantly less image distortion and sig-

nificantly improved contrast between tumor and healthy tissue ADC compared to a conventional DWI sequence acquired with a full phase-direction FOV. To the best of our knowledge, this is the first study to compare either susceptibility-related distortion or tumor contrast in prostate DWI utilizing conventional- and reduced-FOV DWI acquired in the same exam.

It must be noted that the patient population in this study was enrolled regardless of Gleason score, and as a result does not adequately represent a range of tumor aggressiveness. Regardless, the FULL ADC values measured in this study in tumor (mean = 1.00 $\pm$ 0.52x10^{-3} mm^2/s) and healthy tissue (mean = 1.61 $\pm$ 0.40x10^{-3} mm^2/s) were similar to those from other studies, which had healthy values ranging from 1.59 $\pm$ 0.04x10^{-3} mm^2/s to 1.75 $\pm$ 0.23x10^{-3} mm^2/s [41] [86] and tumor values for Gleason Score = 6 disease ranging from 0.86 $\pm$ 0.04x10^{-3} mm^2/s to 1.3 $\pm$ 0.30x10^{-3} mm^2/s [87] [88]. Absolute contrast measures between tumor ADC and healthy tissue ADC were also similar to the values from the literature, which were estimated to be in the range of 28% to 40% [34].

Because the implementation of the rFOV technique in this study allows a higher image resolution compared to the FULL sequence while maintaining clinically-applicable scan times, the technique also decreases partial voluming effects in heterogeneous tissue. The reduced partial volumning and the reduced distortion near tissue interfaces may be partially responsible for the observed significant increase in image contrast between tumor and healthy tissue in the rFOV sequence in comparison to the FULL sequence.

Other acquisition schemes that reduce the number of phase encoding steps could result in reduced distortion for EPI DWI. However, such methods result in either aliasing in the

image, or require a very large FOV to span the body, resulting in poor spatial resolution. The sequence described in this work uses a pulse sequence incorporating a rectangularly-selective excitation, which enables us to attain a FOV smaller than the body size in the phase-encoding direction, thus achieving high spatial resolution.

Recently, there have been several published works using various rectangularly-selective DWI approaches to improve spatial resolution or increase image quality for optic nerve, spine, and prostate imaging [89] [90] [91], which are fundamentally different from the rFOV sequence tested in this study due to the usage of non-coplanar RF pulses. One such modified DWI acquisition technique was recently evaluated to increase the quality of prostate DWI for the purposes of tractography [90]. This technique is the zonal oblique multi-slice diffusion tensor imaging (ZOOM) DTI sequence, which uses tilted non-coplanar RF pulses to refocus spins contained in the imaging slice. This sequence was developed to perform DWI in the presence of large volumes of fat and unpredictable motion and has demonstrated significant improvement in DWI images of the optic nerve [89]. A drawback of the technique is that the non-coplanar pulses leave residual signal in the imaging plane adjacent to the imaged slice. For multi-slice imaging, utilizing this method requires either increasing the gap between slices to avoid unwanted excitation in the imaging plane, or increasing scan time to ensure imaged tissue is fully relaxed before acquiring each slice, making this method most effective in imaging one-dimensional anatomy, as in the optic nerve. The evaluation in the prostate utilized a smaller FOV and higher spatial resolution than the conventional diffusion technique. ZOOM DTI provided a greater number of fibers detected and more homogeneous

fat saturation but did not result in a reduction in prostate image distortions in the small patient population. In contrast, in this study we demonstrate a significant reduction in prostate DWI image distortion with the rFOV technique compared to the FULL sequence.

Another, similar technique to reduce the FOV in MR of the prostate using outer volume suppression has been presented by Reischauer et al. [91]. This research measured ADC performance for prostate cancer detection showing high accuracy (73.5%), specificity (75.2%), and sensitivity (70.4%) in comparison to biopsy, but did not compare the ADC obtained from the novel technique with ADC from the conventional technique to assess the impact on distortion. As both this study and ours reduce the number of phase encoding steps acquired, both are apt to reduce susceptibility artifact in the images, and their study did report attaining high quality images. However, the outer volume suppression method excites tissue adjacent to the imaged slice similar to the ZOOM DTI method, again requiring either increased slice gap or wait time for relaxation. While likely similar in reducing distortion artifact, our study used a 2D, echo-planar RF refocusing pulse [85], which does not excite adjacent tissue, to achieve the reduced-FOV enabling multi-slice imaging without requiring increased scan time or slice gap. However we did not perform a direct comparison to this technique and thus cannot compare the image quality.

The pulse sequence used in our research study has been previously demonstrated to enable high spatial resolution and qualitatively increase image quality in breast DWI [92] and pancreatic DWI [93]. These studies demonstrated that the mean ADC of tumor regions was not significantly different between rFOV and FULL DWI. However, the minimum ADC

value of a tumor region was found to be significantly lower in the rFOV sequence in the breast study [92]. These findings are consistent with our results that demonstrated qualitatively and quantitatively increased image quality and non-significant differences between the ADC values of the FULL and rFOV sequences with a trend toward lower tumor ADC values for rFOV than the FULL sequence. The pancreatic study [93] found no difference between ADC values in FULL and rFOV DWI images, however the sequence was designed to maximize the image quality in favor of increasing contrast. Although these studies represent potential for rFOV DWI in a variety of organs, our study investigated the unique scenario of imaging a thin band of tissue of interest (the peripheral zone) adjacent to tissue with potentially drastically different magnetic susceptibility (air, fecal matter, or blood in the rectum), prone to severe distortion artifacts.

In spite of the sharp excitation profile in the phase encoding direction from the high time-bandwidth 2D RF pulse used in the rFOV sequence [85], in our particular application, signal in the transition band from the very high fluid signal along the rectal wall—such as a perineal hernia—can cause serious wrapping artifact. There is risk of such signal wrapping into the central gland of patients with very large prostates. This is particularly limiting to patients who suffer from benign prostatic hyperplasia, which increases PSA and prostate size, typically leading to clinical testing for prostate cancer staging. Encoding a slightly larger FOV than the excited FOV extent or adding a saturation band to the oblique posterior of the prostate can prevent this artifact.

One limitation of this study is the measures were user dependent in scoring the distor-

tion, in identifying corresponding slices, and in visually matching circles to the rectal wall. However, the changes in visual scores between the FULL and the rFOV sequences were very similar among the three readers, and both the visual scoring and the quantitative measures of rectal wall distortion yielded similarly significant reduction in distortion with the rFOV sequence compared to the FULL sequence. These results lend confidence to our conclusion that the rFOV sequence results in less image distortion on ADC maps than the FULL sequence.

Another limitation of this study is the use of a single, non-zero b-value in all patients with comparison to a b=0 image. Our ADC values may differ from those obtained using a non-zero reference image. Although there is no consensus on the optimal b-value for prostate cancer detection, in addition to the moderate b-value we used (b=600), studies have shown relevance for high-b-value acquisition for detection of prostate cancer [94] [95]. At higher b-values, the rFOV DWI acquisition would require increased averaging to boost the SNR, increasing scan time. Due to scan time constraints in the present study, rFOV DWI at higher b-values was not acquired in this work but will be explored in the future.

Despite the limited scope of our study, the distortion due to susceptibility artifact was significantly lower in the rFOV sequence than in the comparable FULL sequence. Additionally, the rFOV technique employed has been shown to increase contrast between biopsy-proven, radiologist-identified tumor regions and healthy contralateral tissue. This is particularly important, as the ADC map intensity may correlate with tumor grade in prostate cancer [34]. Increasing tumor contrast may increase the value of using the ADC map for both detecting

prostate cancer and assessing its grade.

In conclusion, the rFOV sequence yielded significantly decreased rectal wall susceptibility artifact and provided significantly higher contrast in ADC value between tumor and healthy tissue as compared to the FULL sequence without significantly increasing scan time. This technique shows great promise for improving DWI quality, potentially improving the detection of prostate cancer by MRI.

Chapter 3

Distinguishing Inflammation from Low-Grade Prostate Cancer in the Peripheral Zone of the Prostate

Abstract

Inflammation is a common confounder on prostate MRI, mimicking low-grade prostate cancer in the peripheral zone (PZ). The purpose of this study was to develop a model to distinguish inflammation in the PZ of the prostate from normal PZ tissue and low-grade prostate cancer using an optimized combination of multiparametric MRI (mpMRI) parameters. Eighteen patients with pathologist-defined regions of normal PZ tissue, inflammation, and low-grade prostate cancer, underwent a 3T mpMRI including T_2-weighted imaging, diffusion-weighted imaging, dynamic contrast-enhanced (DCE) MRI, and 3D ^{1}H spectroscopic imaging. Regions of interest were transposed from whole-mount pathology onto T_2-weighted images and propagated to functional maps created from the mpMRI. A depth-restricted decision tree was built to select the most distinguishing features, and to provide an implementable outline for radiologists. A tree built on apparent diffusion coefficient (ADC) and DCE maximal

enhancement slope correctly classified 79.6% of 54 regions as cancer, inflammation, or normal PZ tissue. In Wilcoxon rank sum tests, mean ADC in normal PZ tissue (1.49±0.23 10^{-3}mm^2/s) was significantly higher than that of inflammation (1.11±0.24, $p<0.01$) and low-grade prostate cancer (1.11±0.21, $p<0.01$). Inflammation and low-grade prostate cancer were not distinguishable by ADC alone ($p=0.95$). However, low-grade prostate cancer had significantly faster maximal enhancement slope on DCE (1.24±0.41 enhancement over previous timepoint) than inflammation (0.77±0.28, $p<0.01$) and normal PZ tissue (0.90±0.36, $p=0.02$). Inflammation and normal PZ tissue were not distinguishable on DCE maximal enhancement slope ($p=0.57$) alone.

3.1 Introduction

Multiparametric MRI (mpMRI) is a powerful noninvasive technique for the staging of prostate cancer [96] [97], and is increasingly included in clinical management of patients in the United States [98] [99] and abroad [100] [101]. The number of tissue properties that can be probed by mpMRI in a single exam can improve the characterization of prostate cancer: T_2-weighted imaging for anatomic differentiation, diffusion-weighted imaging (DWI) to measure cellularity, dynamic contrast-enhanced MR imaging (DCE MRI) to assess differences in the gland's perfusion and tissue structure, and ^{1}H-MR spectroscopic imaging (^{1}H-MRSI) to examine differences in metabolite concentrations.

Prostate cancer typically occurs in the presence of heterogeneous benign tissues, which can complicate the ability of mpMRI to identify and assess the presence, extent and ag-

gressiveness of prostate cancer [33] [102]. Inflammation in the prostate is suspected to be a major cause of false positive MRI readings [103] [104] [105], and its characterization of reduced signal on T_2-weighted imaging [106] and apparent diffusion coefficient (ADC) maps is noted in the current version of the Prostate Imaging and Reporting Data System (PI-RADS v2) [13]. In the peripheral zone (PZ), where 70% of prostate cancer is located, inflammation presents with low signal intensity on ADC maps [107]. ADC value scales inversely with prostate cancer grade, and inflammation overlaps to a large extent with low-grade prostate cancer [13].

PI-RADS v2 also cites that inflammation in the PZ can present as a false positive on DCE MRI due to increased perfusion, where a positive DCE MRI finding is defined as early or focal enhancement compared to normal adjacent tissue. However, PI-RADS v2 also notes that assessment of DCE MRI could be enhanced by the creation of parametric maps [13]. Common parametric maps include peak enhancement, time to peak enhancement, and maximal enhancement slope. Fully quantitative metrics, such as the transfer constant from the blood plasma to the extracellular space (K^{trans}), can be robust to patient perfusion differences but rely on arterial input quantification and pharmacokinetic modeling. Inflammation can also confound ^{1}H-MRSI by presenting with elevated choline in comparison to normal tissue in the peripheral zone, statistically indistinguishable from regions of prostate cancer, however this metabolic signature is shared with other confounders such as high-grade prostatic intraepithelial neoplasia [76] [105].

The purpose of this study was to create a model for the prostate PZ for distinguishing

inflammation from both normal tissue and low-grade prostate cancer using an optimized combination of mpMRI parameter maps, using whole-mount section pathology as the reference standard.

3.2 Materials and Methods

This study was approved by the Committee on Human Research at this institution and was compliant with the Health Insurance Portability and Accountability Act. Written, informed consent was obtained from all 18 subjects. After whole-mount resection of the prostate, a pathologist characterized regions of cancer by Gleason grade, as well as regions of inflammation, atrophy, benign prostatic hyperplasia, high-grade prostatic intraepithelial neoplasia, and normal PZ tissue.

Patients with clear-cut regions of low-grade cancer (Gleason 3+3 or Gleason 3+4), of inflammation, and of normal tissue in the PZ identified at the post-surgical whole-mount pathology reading were included in this analysis. Pathological inflammation was defined as 5% or greater infiltration of lymphocytes into the tissue and assumed to be chronic; there were no patients with evidence of acute inflammation enrolled in this study. The patient's mean age at time of scan was 63.9±5.8 years. The average PSA in this population was 5.1±1.8 ng/mL, with 5 patients presenting with a Gleason Score of 3+3 and 13 patients presenting with a Gleason Score of 3+4 at the time of surgery.

Patients received a 3T multiparametric MRI of the prostate (GE Healthcare, Waukesha WI, USA) with a GE pelvic phased coil array and a flexible balloon endorectal coil (Medrad,

Inc., Indianola PA, USA). Anatomic imaging was performed using a T_2-weighted fast spin-echo sequence with FOV = 18 cm, slice thickness = 3mm, matrix = 512 x 512, and TR/TE = 6000/96 ms, prescribed at an obliquity matching the posterior edge of the prostate. Anatomic images were intensity-corrected for the endorectal coil profile [19].

Functional imaging (DWI, DCE MRI and ^{1}H MRSI) was performed at the same obliquity and slice thickness as the anatomical T_2-weighted sequence. Six-direction diffusion-weighted imaging (DWI) was acquired using a 2D single shot spin-echo sequence with a b-value of 600 s/mm^2, FOV = 18 cm, TR/TE = 4000/(minimum full TE) ms, slice thickness = 3mm. Additionally, in 7/18 patients, high b-value DWI was acquired using a 2D single shot spin-echo sequence with a b-value of 1350 s/mm^2, FOV = 26 cm, TR/TE = 4000/(minimum full TE) ms, slice thickness = 3mm. DCE MRI was acquired using a single dose of gadopentatate dimeglumine (Magnavist, Bayer Inc.) injected at 2 mm/sec with total injected amount determined by patient body weight. DCE MRI used a 3D fast SPGR sequence with a temporal resolution of 10.4 seconds, FOV = 46 cm, TR/TE = 3.5/0.9 ms, flip angle = 5^o, with 5 timepoints acquired before injection to establish a baseline for semi-quantitative metrics. ^{1}H-MRSI was acquired using 3D PRESS with TR/TE = 2000/85 ms, resolution = 5.4x5.4x5.4 mm, NEX=1.

An apparent diffusion coefficient (ADC) map was created from the DWI sequence using in-house software that creates a geometric mean of the images using b=600 s/mm^2 and, under the assumption that prostate tissue is isotropic, calculates ADC value per voxel referencing a T_2-weighted b=0 s/mm^2 image. For the 11 patients for which no high b-value

DWI was acquired, an averaged high b-value (b=1350 s/mm^2) DWI was calculated based upon the lower b-value images, assuming a monoexponential decay. Parametric maps of peak enhancement value, time to peak enhancement, maximal enhancement slope, and average washout slope were created from DCE MRI. Peak value is defined as the maximum intensity reached over the time-course divided by the baseline signal intensity; time to peak enhancement is the discrete time point when the enhancement first reaches 90% of the maximum; maximal enhancement slope is defined as the greatest increase in intensity between any two timepoints; washout slope is the slope from a linear fit to the enhancement curve from the peak through to final timepoints [108]. Metabolic maps from the 0.16 cc resolution ^{1}H MRSI prostate spectra were created based on the integrated areas under the curves for the metabolites choline, creatine, and citrate, and intensity-corrected for the endorectal coil profile [19].

To characterize the MR-measured differences between tissue classes, while avoiding overfitting to our small sample size, a decision tree classifier restricted to a maximum depth of two was trained on the full dataset to provide easily translatable guidelines to the clinic. Post hoc Wilcoxon rank sum tests were used to quantify the statistical differences between prostate tissue types.

3.3 Results

Eighteen patients presented with regions of inflammation, low-grade prostate cancer, and normal PZ tissue, resulting in 54 regions to train a decision tree. Figure 3.1 shows a visual

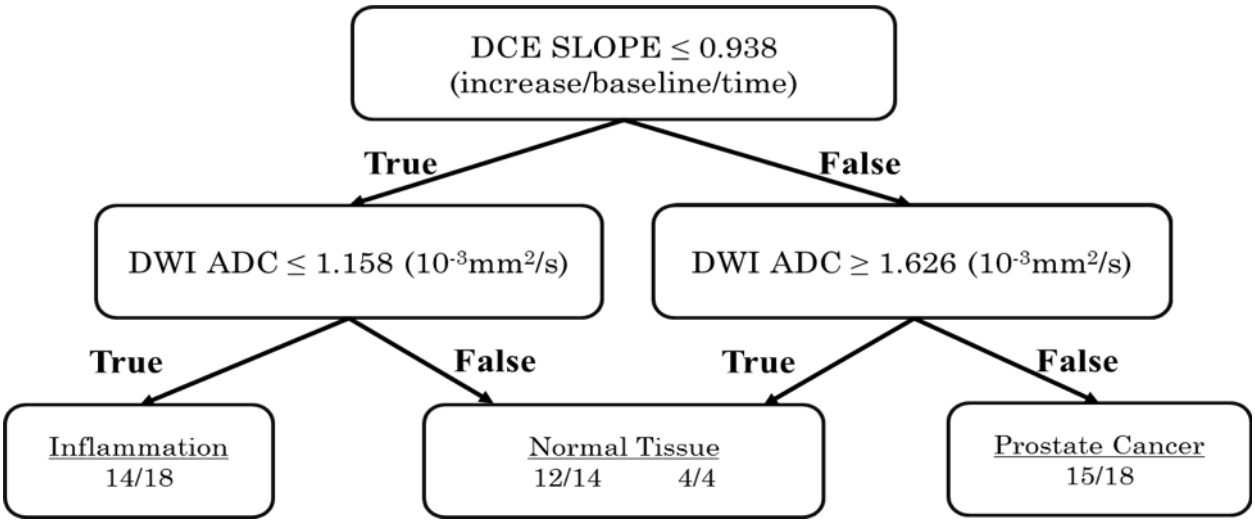

Figure 3.1: The resulting decision tree classifier based on 54 regions of inflammation, low-grade prostate cancer, and normal peripheral zone tissue, constrained to a max depth of two. Signal intensity on the apparent diffusion coefficient (ADC) map created from diffusion-weighted imaging, and on the map of maximal wash-in slope by DCE MRI, correctly classified 80% of all regions and 67% of regions with inflammation.

depiction of the tree structure, which correctly classified 79.6% of the 54 samples as low-grade prostate cancer, inflammation, or normal PZ tissue. Two regions of inflammation and one region of normal PZ tissue were incorrectly classified as low-grade prostate cancer; only one region of low-grade prostate cancer and one region of normal PZ tissue were classified as inflammation. The decision path for identifying normal PZ tissue had two branches, for high and low maximal enhancement slope, both of which included a decision based on a high ADC value. Using these criteria a total of two regions of low-grade prostate cancer and four regions of inflammation were classified as normal PZ tissue.

ROIs were not normally distributed within tissue types (Shapiro-Wilk tests); Wilcoxon rank sum tests were used for post hoc analysis. Intensity ranges for the ADC value and the maximal enhancement slope for normal PZ tissue, regions of inflammation, and low-

grade prostate cancer are shown in Figure 3.2. ADC in normal PZ tissue was significantly higher than that of inflammation ($p<0.01$), and significantly higher than that of low-grade prostate cancer ($p<0.01$). However, inflammation and low-grade prostate cancer were not distinguishable by ADC value ($p=0.95$). Maximal enhancement slope values (measured as enhancement over previous timepoint) in regions of inflammation were not distinguishable from in regions of normal PZ tissue ($p=0.57$). Regions of low-grade prostate cancer had a significantly faster maximal enhancement slope than both normal PZ tissue ($p=0.02$) and inflammation ($p<0.01$). Images from a representative patient with Gleason 3+4 low-grade prostate cancer and a contralateral region of inflammation are shown in Figure 3.3.

We can see that both a region of low-grade prostate cancer denoted by a solid arrow, and a region of inflammation denoted by a striped arrow, are distinguishable from normal PZ tissue by reduced signal on ADC (B). Low-grade prostate cancer is distinguishable from inflammation and normal PZ tissue by increased maximal enhancement slope on DCE MRI, and inflammation is indistinguishable from the normal PZ (C).

ADC was reduced in 17/18 regions of inflammation, and all regions of cancer, compared to normal PZ tissue in a given patient. ADC in both regions of cancer and regions of inflammation was, on average, reduced by 24% compared to normal PZ tissue from the same patient. Maximal enhancement slope was higher in cancer compared to normal tissue in 15 of 18 cases, on average elevated 54%. Regions of inflammation were comparable to normal tissue within patients, with higher maximal enhancement slope in 8 cases and lower maximal enhancement slope in 10 cases. Regions of inflammation showed an average maximal

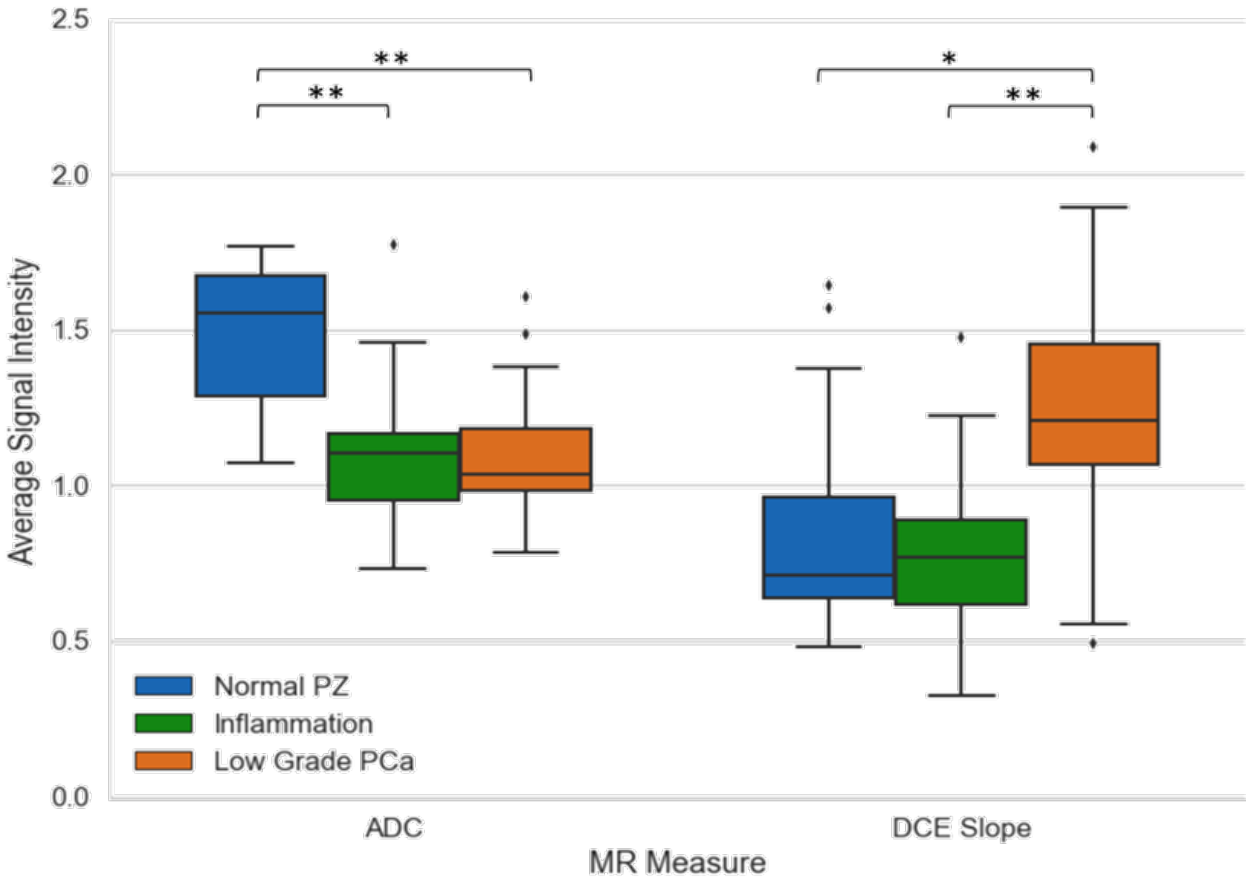

Figure 3.2: Summary of average signal intensities and significances between normal peripheral zone tissue (Normal PZ), inflammation, and low-grade prostate cancer (Low Grade PCa) in the 54 regions studied on the apparent diffusion coefficient (ADC) map created from diffusion-weighted imaging (10^{-3}mm^2/s), and on the map of maximal wash-in slope by dynamic contrast-enhanced (DCE) MRI (enhancement over previous timepoint).

enhancement slope <1% different from regions of normal PZ tissue in the same patient. In all but one case, maximal enhancement slope in regions of inflammation was lower than in regions of cancer within the same patient. Average enhancement per tissue type over time is presented in Figure 3.4.

Other imaging metrics showed significances and trends between the tissue types, but were withheld from our depth-restricted model to avoid overfitting. Inflammation showed

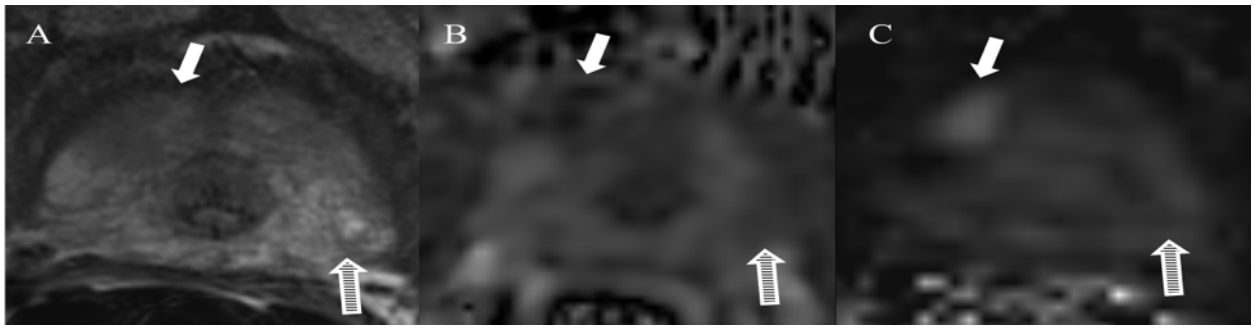

Figure 3.3: A representative **A** T_2-weighted image, **B** ADC map, and **C** DCE MRI maximal enhancement slope map showing a region of Gleason 3+4 low-grade prostate cancer (solid arrows) with reduced T_2 signal intensity, reduced ADC, and increased maximal enhancement slope. The region of inflammation (striped arrows) shows normal T_2 signal intensity, with reduced ADC, and no increase in maximal enhancement slope compared to the contralateral normal PZ tissue.

significantly lower signal on traditional T_2-weighted imaging compared to normal PZ tissue ($p<0.01$), and was not significantly different than low-grade prostate cancer ($p=0.16$). Washout slope in regions of low-grade prostate cancer was significantly faster than in normal PZ tissue ($p<0.05$) and non-significantly faster than in regions of inflammation ($p=0.24$).

Compared to normal PZ tissue, low-grade prostate cancer showed an average of 26%±27% higher levels of choline, and regions of inflammation showed an average of 19%±39% lower levels of choline; none of these differences were significant. Both regions of inflammation and of low-grade prostate cancer had lower levels of creatine (39%±11% and 20%±40% reduced, respectively) and lower levels of citrate (73%±230% and 46%±19% reduced, respectively) than that of normal PZ tissue, but only the low citrate in regions of inflammation was significantly lower than that of normal PZ tissue ($p=0.018$). Regions of inflammation had lower levels of all three metabolites in comparison to low-grade prostate cancer and normal PZ tissue.

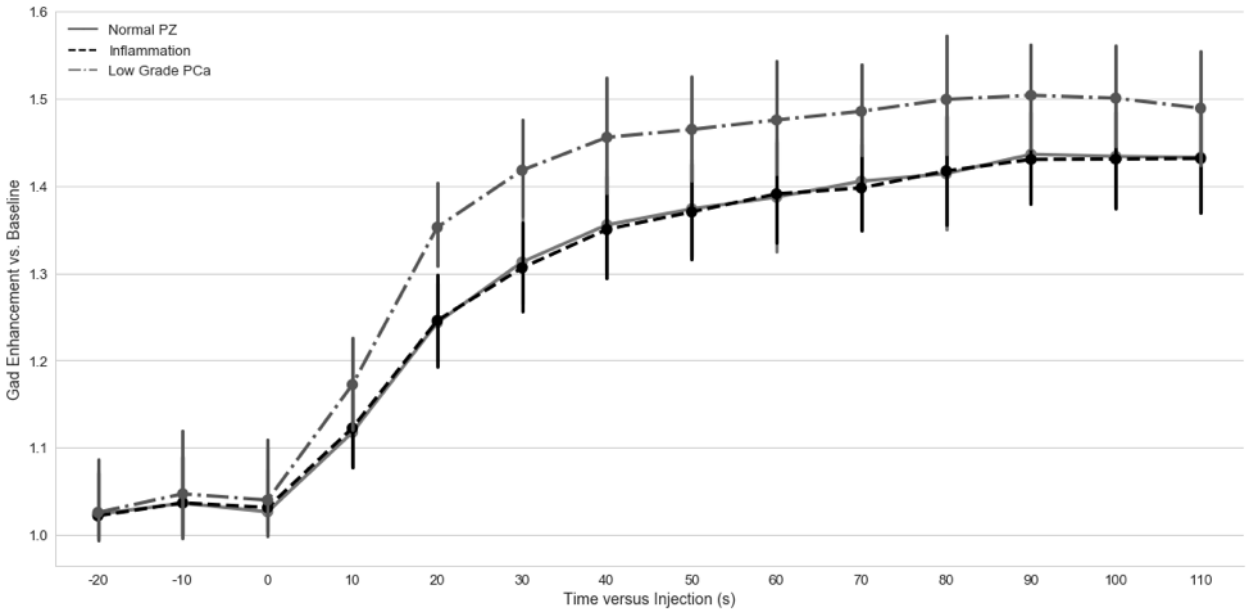

Figure 3.4: DCE MRI results per timepoint, showing mean and 95% CI of signal intensity per tissue type, and normalized to the baseline signal intensity and injection time. We see tissue with inflammation demonstrating behavior remarkably similar to normal PZ tissue, with low-grade prostate cancer showing faster uptake.

3.4 Discussion

In this study we investigated patients with a ^{1}H mpMRI exam prior to radical prostatectomy with whole-mount histopathologic-identified inflammation, low-grade prostate cancer, and normal tissue in the PZ. Standard of care histopathologic assessments typically provide information about the presence, extent, and aggressiveness of cancer, but rarely report the presence and extent of confounding factors such as inflammation, which can significantly impact cancer identification on a ^{1}H mpMRI exam. The most significant finding of this study is that chronic inflammation in the peripheral zone of the prostate, histopathologically assessed by the presence of lymphocytes in tissue, can be quantitatively distinguished from both normal PZ tissue and low-grade prostate cancer using a combination of the ADC and

the maximal enhancement slope values on DCE MRI, acquired as part of standard mpMRI prostate cancer exams being acquired around the world [98] [99] [101]. These quantitative DWI and DCE MRI results can be used in combination with the more qualitative PI-RADS v2 interpretation of prostate cancer presence to improve the assessment of presence and extent of prostate cancer at diagnosis, improving therapeutic selection for individual patients.

Inflammation in the prostate normally presents as acute or chronic. Chronic inflammation is the more likely clinical scenario for patients going on for active surveillance and more aggressive interventions such as surgery or radiation [109]. In our work, no patients were diagnosed with acute prostatitis, therefore the findings pertain to chronic inflammation, whereas most published data [110] [111] references acute inflammation.

Other works [107] [110] have found differences in the ADC value of inflammation compared to normal PZ tissue and prostate cancer, however the definitions of cancer, inflammation, and normal tissue differ in these works. One study found regions of inflammation indistinguishable from normal PZ tissue on ADC, however the normal PZ tissue values were biopsy-confirmed benign regions from radiologist-defined cancer-suspicious regions on MR [107]. This suggests that other confounding benign pathologies such as atrophy, HGPIN, and BPH could have been present in their normal PZ tissues, and explains why regions of inflammation would appear similarly in ADC value. A study comparing inflammation to all grades of prostate cancer, lowering the average ADC value for prostate cancer, found significantly lower ADC values in prostate cancer compared to regions of inflammation [110].

Similarly, there have been consistent findings in DCE MRI studies of inflammation; how-

ever, the semi-quantitative metrics extracted from these studies differ between groups. In a study of 38 needle biopsy samples of inflammation from 178 men after DCE MRI as part of an mpMRI of the prostate, regions of inflammation enhanced in the early part of DCE MRI, similar to prostate cancer, potentially resulting in a false positive radiologic reading [111]. Likewise, in 50 patients studied by whole-mount histopathology after mpMRI, 9 regions of inflammation showed early enhancement with a heterogeneous appearance, similar to regions of prostate cancer [110]. In these works, along with PI-RADS v2 [13], the most commonly referenced metric extracted from DCE MRI is early enhancement.

In this work, we show DCE MRI distinguishing inflammation from prostate cancer, contrary to the above. While regions of inflammation in our data have higher initial enhancement than regions of normal PZ tissue, similar to cancer and described in the above works, it's the behavior of enhancement—characterized by the maximal enhancement slope—that distinguishes regions of inflammation from regions of low-grade prostate cancer. The differences in presentation could also be explained by different types of inflammation in the tissue. Acute inflammation is a call to repair, characterized by leaky vasculature and an influx of lymphocytes, and we would expect increased and early enhancement. However, in chronic inflammation, the vasculature is normal, leading to a normal enhancement slope.

There were several limitations to this study, primarily that the small number of subjects prevents us from reliably extrapolating these findings to a wider population. A larger study could determine numeric cutoffs for the ADC value and maximal enhancement slope that separate inflammation from low-grade prostate cancer and normal PZ tissue with enough

certainty to recommend to other sites. However, the strength of characterization and interpretability in this small population suggests similar guidelines could be incorporated into clinical practice.

A second limitation is that the numerical cutoffs are not directly applicable to other sites or imaging protocols without calibration or use of fully quantitative parameters, such as K^{trans}, instead of maximum enhancement slope. While K^{trans} is robust to differences in patient perfusion, it requires the measurement or assumption of an arterial input function and pharmacokinetic modeling, which may not be possible at all sites. The semi-quantitative maps used in this study can quantify key characteristics of enhancement with limited post-processing needs, while correcting for some patient and acquisition artifacts, but without correcting for the baseline T_1 values from the same tissue, or locating and modeling the input at a lateral artery. Semi-quantitative maps, with their less-intensive post-processing needs and fewer tissue parameters, yielded excellent tissue discrimination in this study. K^{trans} values could be used instead of the maximum enhancement slope, with different cutoffs, but relative differences should hold within a patient whether using semi-quantitative or fully-quantitative metrics.

In conclusion, inflammation in the PZ is characterized by lower ADC and comparable maximal enhancement slope on DCE MRI compared to normal tissue. A combination of ADC value and maximal enhancement slope on DCE MRI can distinguish regions of inflammation from low-grade prostate cancer and from normal PZ tissue in the human prostate with very good accuracy in this population. Considering the widespread presence of chronic

inflammation in the human prostate, these results are promising for improving the differential diagnosis of these tissues and should be explored further in larger patient populations. Future versions of PI-RADS may consider defining a positive DCE MRI read by semi-quantitative parametric maps, potentially expanding the role of DCE MRI for prostate tissue characterization.

Chapter 4

Multi-element, Multi-nuclear Endorectal Coil for Development of a ^{13}C, ^{1}H-Multiparametric Magnetic Resonance Imaging Exam of the Human Prostate at 3T

Abstract

The mpMRI exam is increasingly used to determine if a patient has indolent low-grade versus aggressive high-grade prostate cancer at biopsy diagnosis, and whether active surveillance or aggressive treatment is required for each patient. However, the length of the current mpMRI exam is a major limitation to widespread use, and the combined data cannot adequately determine which tumors will progress and therefore require treatment. MR spectroscopic imaging with hyperpolarized ^{13}C can probe real-time tumor metabolism and correlates with aggressiveness in murine models. The non-renewable hyperpolarization restricts signal reception time, and current hardware cannot cover the full area of the prostate at a clinically-valuable spatial resolution when acquired in patients. Improving hardware to allow parallel

imaging for both proton- and carbon-sensitive sequences will decrease scan time, and tailoring RF coil elements' size and location to that of the prostate gland can recover the signal-to-noise ratio (SNR) inherently lost in acceleration. In this chapter, we propose a multi-nuclear, multi-element endorectal coil (ERC) to mimic the geometry of the prostate, increasing SNR and potential acceleration at the proton and carbon frequencies. Preliminary data shows a three-element longitudinal array to offer the most acceleration while maintaining SNR and penetration depth. As an ethical constraint, all design criteria must be met without increasing the size of the current ERC.

4.1 Background and Significance

Prostate cancer is extremely prevalent, with diagnoses in 1 in 6 American men, but fatal for only 12% of cases [112]. Because the risk of side effects from the aggressive treatment of prostate cancer (surgery and radiation therapy) is high (77%) compared to the risk of short-term progression of prostate cancer (20%), the accurate characterization of prostate cancer at diagnosis remains an active area of research for the clinical management of individual patients as well as for monitoring therapy [113]. Active surveillance has emerged as an appropriate management technique for patients whose disease is likely indolent (small and Gleason grade $\leq$ 3+3) [114]. New focal therapy approaches are being considered for men with defined regions of intermediate risk prostate cancer (moderate size cancers that have some secondary Gleason pattern 4) that can be identified on imaging [113].

These approaches to treating prostate cancer require the ability for clinicians to accurately

identify the location, size and pathologic aggressiveness of often small regions of prostate cancer. This is currently undertaken through a mpMRI exam [115]. Particularly important for accurate representation of disease is a fine spatial resolution, which is limited by each image's SNR. In order to acquire sufficient spatial resolution in a clinically reasonable time, particularly for the low SNR imaging sequences—^{1}H-MRSI, DCE and DWI—the mpMRI data is acquired using an ERC and a phased array of external surface coils [116]. The ERC significantly increases signal within the prostate, and decreases signal obtained from outside the prostate that contributes to noise [41]. Combining an ERC and phased-array coils has proven to increase the SNR in prostate exams at 3T over nine-fold in comparison to use of a phased-array alone [17]. However, the mpMRI with full diagnostic quality lasts approximately 75 minutes, which can limit patient compliance and widespread use.

An additional metric of functional imaging has emerged to probe real-time metabolism for metabolic markers of cancerous activity. Injecting pyruvate labeled with hyperpolarized carbon [1-^{13}C]pyruvate shows flux of clinically-relevant biomarkers that participate in the Warburg Effect [77]: an increase in aerobic glycolytic metabolism in cancerous tissue. Pyruvate is the natural output of glycolysis, and in healthy tissue enters the TCA cycle, with its C1-carbon converted to carbon dioxide (CO_2) [117]. Pyruvate is also converted to alanine via the enzyme alanine transaminase (ALT) to varying degrees in normal tissues. However, due to a number of genetic and microenvironment changes associated with cancer development and progression, a significant proportion of pyruvate is converted to lactate via the enzyme lactate dehydrogenase [118]. Although increased energy in the form of ATP is created via

TCA metabolism, cancer utilizes a high rate of glycolysis even in the presence of oxygen.

Dynamic nuclear polarization (DNP) creates preferential alignment in nuclear spins by the Overhauser effect; by transferring spin polarizations from electrons to nuclei, increasing signal intensity per element until the polarization relaxes [79]. In prostate cancer metabolism, the preferred route to use this technology is in hyperpolarized ^{13}C-labeled pyruvate. To determine the impact of cancerous development on cellular metabolism, we can probe how much [1-^{13}C]pyruvate is converted to [1-^{13}C]lactate versus how much is converted into ^{13}C bicarbonate and [1-^{13}C]alanine by hyperpolarized ^{13}C MRI. ^{13}C is visible on MRI at 3T at a frequency of $\sim$32 MHz [81], and by tuning an ERC to this frequency we can receive signal during and after injection, where hyperpolarization increases the signal from ^{13}C by over 10,000 times [119] [120]. ^{13}C experiences different chemical shielding in pyruvate, lactate, and carbon dioxide, so the increased preference of cancer for increased glycolysis and lactate production are observable by MRSI [79]. However, polarization for hyperpolarized [1-^{13}C]pyruvate decreases rapidly (at the T_1 relaxation rate of the ^{13}C labeled carbonyl in [1-^{13}C]pyruvate, approximately 60 seconds at a magnetic field strength of 3T) after dissolution and injection in to a patient [120].

There are current ERC arrays that combine coils tuned for proton with a coil tuned to another nucleus' frequency. Inclusion of a ^{13}C-sensitive coil in an ERC design creates increased sensitivity to cancer diagnostics and staging, however all such currently designed coils utilize single-element reception, limiting coverage and sensitivity of ^{13}C signal reception across the prostate. No existing ERC contains multiple elements at multiple frequencies,

in spite of the unique potential of parallel imaging to improve spatial resolution for the non-renewable hyperpolarized signal. While there is a design for a multi-element proton-sensitive an ERC [121]—using two elements overlapping in the R/L plane to provide increased sensitivity and parallel imaging capability, overlapping coils in the center of the prostate both limits the width of the minor axis of each element, reducing penetration [122], and increases the signal from the urethra, which runs through the prostate in the same plane. The healthy urethra contains high amounts of glycerophosphocholine, which resonates in the region of choline—a marker of prostate cancer [123] on ^{1}H-MRSI. This design also limits acceleration by using elements with similar sensitivity profiles, which increases the coil g-factor.

Precision medicine relies on diverse and correlative information on a patient's disease state to offer the most beneficial treatment options. For prostate cancer, the mpMRI exam contributes anatomic and functional tumor information, but the exam length limits widespread usage, and measuring increased rates of metabolic reactions associated with cancer presence and progression cannot be acquired using the current mpMRI exam [124] [125]. Incorporating hyperpolarized ^{13}C would allow real-time monitoring of metabolic flux within the prostate [120]; however the spatial resolution of hyperpolarized ^{13}C MRI data from the human prostate is still relatively coarse. The proposed research is significant because it will improve signal reception of the ERC by both decreasing noise received from outside the prostate gland and by enabling accelerated reception by geometrically-optimized parallel imaging of regions within the prostate. This advancement in signal reception will allow acceleration at the proton frequency, which has the potential to shorten any 3D sequence in

the mpMRI [126] [127]. At our institution, anatomic T_1-weighted, MRSI and DCE imaging techniques are acquired in 3D. Additionally, 3D T_2-weighted and 3D DWI sequences are now offered by major MRI suppliers. Utilizing parallel imaging with an acceleration factor of at least 2 will reduce the mpMRI exam time to less than one hour. Additionally, acceleration can lead to acquiring current ^{13}C MRSI in 8.5 seconds instead of 12 seconds, with the remaining 3.5 seconds traded for increased spatial resolution to better assess cancer aggressiveness and treatment response [120].

The focus of this research was to design and build a receive-only proton- and carbon endorectal coil to provide increased SNR and imaging acceleration by optimizing element geometry to the shape of the prostate. The hypothesis for this work, based on preliminary data, is that creating an array in the longitudinal direction with elements tailored to prostate shape will both increase SNR by excluding irrelevant tissues, and will allow for greater disparity in signal profiles from individual elements, resulting in higher acceleration potential and more homogeneous coverage.

While the proposed ERC will create a hardware platform for rapid imaging and in-human diagnostic ^{13}C MRSI, the primary outcomes for this work will be analysis of prototype and simulation quality in comparison to that of current ERC technology. As an ethical constraint, all design criteria must be met without increasing the size of the current ERC.

4.2 Prototype Design and Simulation Results

To design and build a receive-only proton- and carbon-sensitive endorectal coil to provide increased SNR and imaging acceleration by optimizing element geometry to the shape of the prostate, we will need to prove that geometry developed in this proposal better matches the anatomy of the prostate than current designs to improve SNR. We will need to prove that at least two individual elements in our design have nonsignificant sensitivity profile overlap to improve acceleration, and that this is not feasible with currently available designs. We will need to prove that overlapping receive elements in the longitudinal direction is feasible without the effects of inductive coupling between each element, that signal penetration is not lost over the area of the prostate gland compared to currently available designs, that the carbon elements can be decoupled from the proton elements, and that these improvements are feasible under the ethical constraint of not increasing the size of the ERC for equal patient comfort.

Experiment 1: determine the expected shape and size of the prostate gland.

Current ERC technology does not discriminate signal reception in the area of the prostate as it is not tailored to the geometry of the prostate. Instead, it receives non-uniformly from an area including the prostate. Receiving signal from areas outside the prostate increases the amount of noise that can map to pixels inside the prostate on resulting images. While prostate anatomy varies, especially in the diseased state, there are tendencies which we capitalize on in our design. Prostatic growth is generally a product of the central gland

(CG), which can grow during the normal aging process due to benign prostatic hyperplasia (BPH). The CG is largely located in the base of the prostate, thins in the midgland and is absent in the apex. The peripheral zone (PZ) is present surrounding the CG in the base and midgland, and is prominent in the apex. While prostate cancer frequently occurs in the PZ, it is rare in the exams seen at our institution for the PZ to measurably increase in size due to prostate cancer. For this reason, an ERC designed to match the anatomy of healthy and diseased prostate glands should equal the width of current ERCs at the base and midgland of the prostate to accommodate the CG, and taper towards the apex as gland size decreases. This will decrease the amount of signal acquired from tissues surrounding the prostate gland towards the apex while preserving full size towards the base. To validate this hypothesis in a preliminary data set, prostate volume traces from our institution on 8 patients showed a base wider in oblique R/L than towards the apex. An example of this trace is shown in Figure 4.1.

From this preliminary experiment:

$$Prostate\ Width(mm) = \frac{Base}{Midgland} \cong 0.93 \pm 0.116 \quad \frac{Apex}{Midgland} \cong 0.66 \pm 0.067 \tag{4.1}$$

A power analysis will determine whether this preliminary observation holds for the variety of glands seen at our institution, using the mean and standard deviation from the preliminary data, the noncentrality parameter ϕ determines the number of samples required to prove the preliminary observation.

$$To\ Prove: \frac{Base}{Midgland} = 0.93(\phi = 0.55) \quad \frac{Apex}{Midgland} = 0.66(\phi = 0.76) \tag{4.2}$$

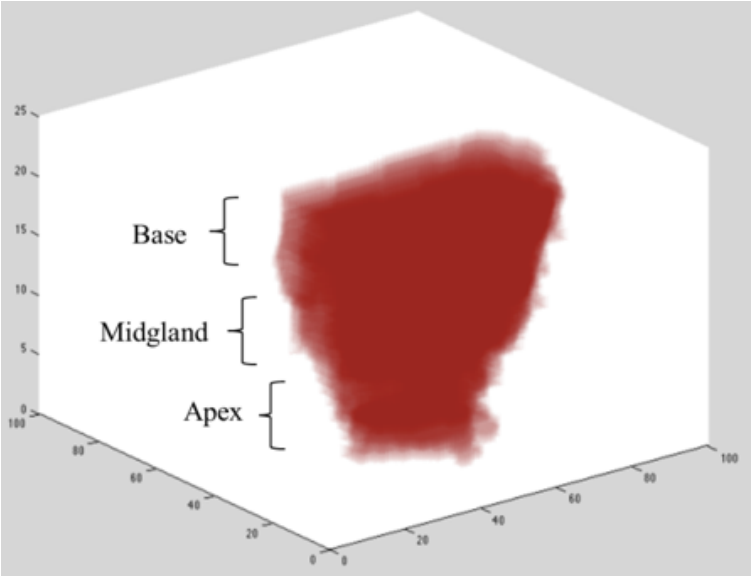

Figure 4.1: In an example patient, we see the base of the prostate is noticeably wider than the apex of the prostate.

To validate this finding, 40 prostates from recent patients at our institution will be segmented and mean width in the base, midgland, and apex will be recorded. The robust commercial software system DynaCAD (Invivo, ©2013) will be used for segmentation. From this, a 3D volume of the prostate will be determined.

Experiment 2: determine the limits of array design based on inductive coupling.

All current ERCs developed with multiple receive elements have two overlapping receive elements, leading to similar sensitivities along the overlap, which underdetermines the matrix combination at the heart of parallel imaging. To prove that at least two elements in our design have no sensitivity profile overlap, we will include three elements in our design. A large center element will receive from the midgland of the prostate, and a small element longitudinally overlapping with the center element will receive from the base and apex of

A

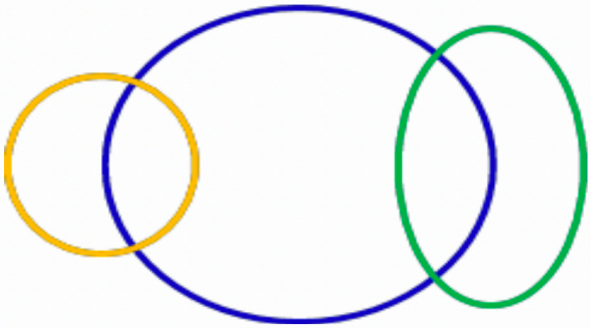

B

Coil	RL (cm)	SI (cm)
Base (green)	4	2.5
Center (blue)	4.5	5.5
Apex (yellow)	3	2.5

Figure 4.2: **A** Proposed 3-element coil design, including a shortened center coil (blue), a wide base coil (green), and a narrow apex coil (yellow), and **B** starting dimensions for individual coil sizes, to be iteratively altered based on optimal coil overlap, while tapering towards the apex in alignment with the gland.

the prostate, respectively, as shown in Figure 4.2.

Although the center element will overlap with both the base and apex elements, the base and apex elements will have minimally-overlapping sensitivity profiles, increasing the potential imaging acceleration. A simulation, shown in Figure 4.3, illustrates the magnetic field induced by the base and apex coils, with little overlap. Because the center coil signal covers the area between base and apex coils, at least two elements will provide signal at all points in the prostate. Determining whether this signal contribution is significant will depend on the iterative size specifications from Experiment 1. This simulation can be repeated with successive designs.

These encouraging simulation results prompted a prototype to prove lack of coupling on the bench. A solid copper wire prototype was developed to resonate at the proton frequency with elements matching the size and shape of the model in Figure 4.2, to determine that overlapping elements in the longitudinal direction is feasible at the proposed dimensions

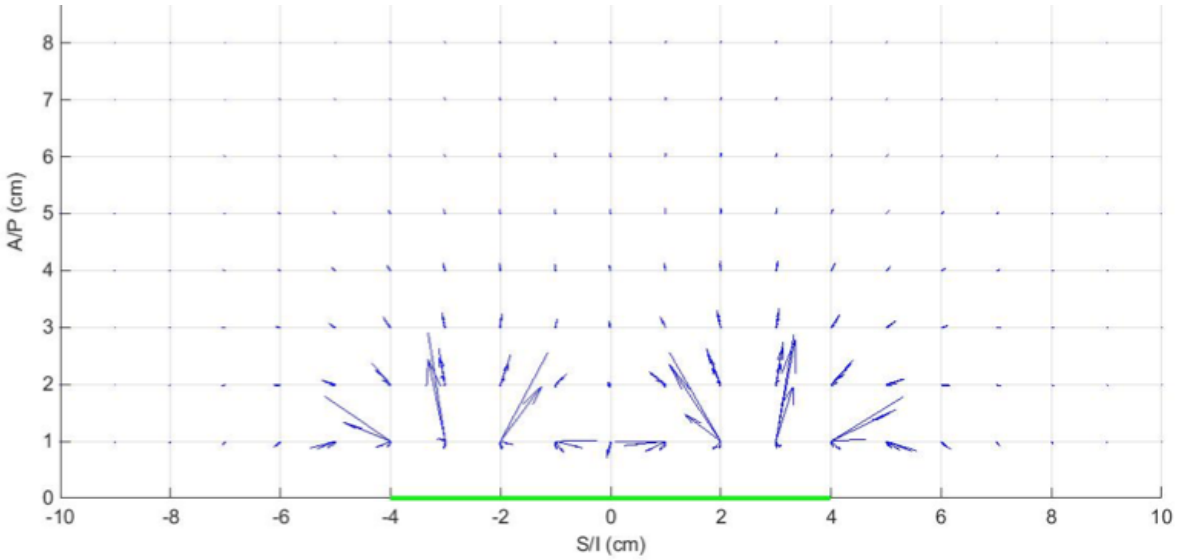

Figure 4.3: Minimal overlap between magnetic fields generated from the base and apex elements (blue) over the length of the coil (green). Note, for this simulation, the magnetic field generated from the center element is not shown.

without the effects of inductive coupling. Using a network analyzer to measure S_{11} (reflection coefficient) by a single-loop sniffer, the elements—once tuned to 128 MHz—were overlapped so that no inductive coupling was present between adjacent elements. The center element was then removed, to ensure no inductive coupling existed between nonadjacent base and apex elements. Overlaid on a ruler in Figure 4.4, we can see that the optimal overlap to negate adjacent inductive coupling extends the coil elements 3mm past the current ERC length of 8 cm. Because an ethical constraint of this project is not increasing the size of the ERC, the center element size will be iteratively shortened to ensure no inductive coupling while keeping within size limitations.

One limitation of this prototype is the use of lumped capacitors, which inherently change the impedance at different locations along an element. The significant lowering in frequency

for reception of ^{13}C changes the relationship between capacitance and inductance and calculation of Q, which relates component values to coil performance and SNR at a range of frequencies given in Eqn 4.3:

$$Q = \frac{f}{\Delta f} = \frac{X_p}{R_p} \qquad where\ X_p = j2\pi fL = \frac{1}{j2\pi fC} \tag{4.3}$$

Where f is the resonant frequency of the coil, Δf is the bandwidth of frequencies received by the coil, R_p is the impedance of the coil, which is 50 ohms, and X_p is the reactance in the coil, which is a function of inductive and capacitive loading in the coil. For ^{13}C-MRSI, Δf must be greater than 5000 Hz to receive from necessary metabolites.

For the proton-sensitive elements, the inductance in the wire is sufficient to resonate at 128 MHz with capacitance in the range of 9 to 14pF—capacitance increases with decreasing element size because length of wire is proportional to inductance. A much higher capacitance is needed to resonate similarly-sized elements at 32 MHz for ^{13}C reception, which will decrease Q, increasing the range of acceptable bandwidth for signal reception. To more accurately distribute the capacitance without introducing lumped inductors, capacitors in the range of 60-140pF will be needed.

Experiment 3: prove that the signal penetration is similar over the area of the prostate in comparison to current ERC designs.

A study of 847 recent prostate exams at our institution was performed to assess the maximal extent of prostate glands in the R/L and oblique A/P directions, with results summarized in Table 4.1. Maximal extent information was obtained from the CSI voxel size of ^{1}H-MRSI

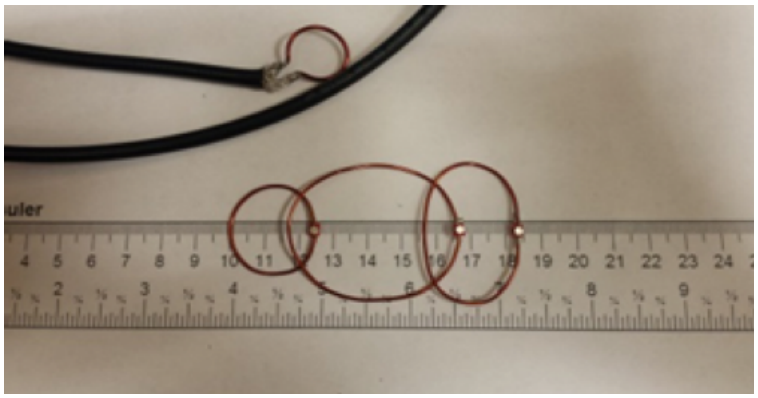

Figure 4.4: Solid copper prototype with lumped capacitors used to assess inductive coupling between adjacent and nonadjacent elements shows no inductive coupling between base and apex coils, and inductive coupling between adjacent elements mitigated by overlap.

in recent exams, which is manually altered by the technologist to align with the edges of the prostate in R/L and oblique A/P. The MatLab simulation introduced in Experiment 2 (Figure 4.3) was expanded to include full magnetic field maps from the proposed coil as well as a model of the current single-loop ERC, shown in Figure 4.5.

We see from Table 4.1 that the maximal size documented in recent prostate exams in R/L is 8 cm. However, in the simulation in Figure 4.5 we see the traditional ERC extending 12-14 cm in R/L, picking up unnecessary signal from outside the prostate gland. This effect is diminished in our proposed design, which extends less than 10cm in R/L. We also see from Table 4.1 that the maximal size in A/P is 7.24 cm, but the 95^{th} percentile is 4.71 cm. Penetration in A/P is difficult for the small element sizes necessary for comfortable ERCs, but less than 5% of prostates extend further than 4.71 cm in A/P. We see that the proposed design performs similarly to the traditional ERC in A/P penetration. However, this preliminary experiment doesn't distinguish the largest extent of the prostate from differences between the base, midgland, and apex. To adequately answer the question to whether the

Table 4.1: Size ranges of prostates examined at our institution, n=847. Data collected based on the prescription volume acquired during ^{1}H-MRSI imaging, wherein prescription volume is tight around the prostate, excluding the surrounding lipid and rectum.

Prostate Sizes	**R/L (cm)**	**A/P (cm)**
Minimum	2.37	1.78
5^{th} %	*4.19*	*2.28*
25^{th} %	*4.92*	*2.86*
Mean	5.40	3.39
Median	5.38	3.30
75^{th} %	*5.89*	*3.85*
95^{th} %	*6.69*	*4.71*
Maximum	8.06	7.24

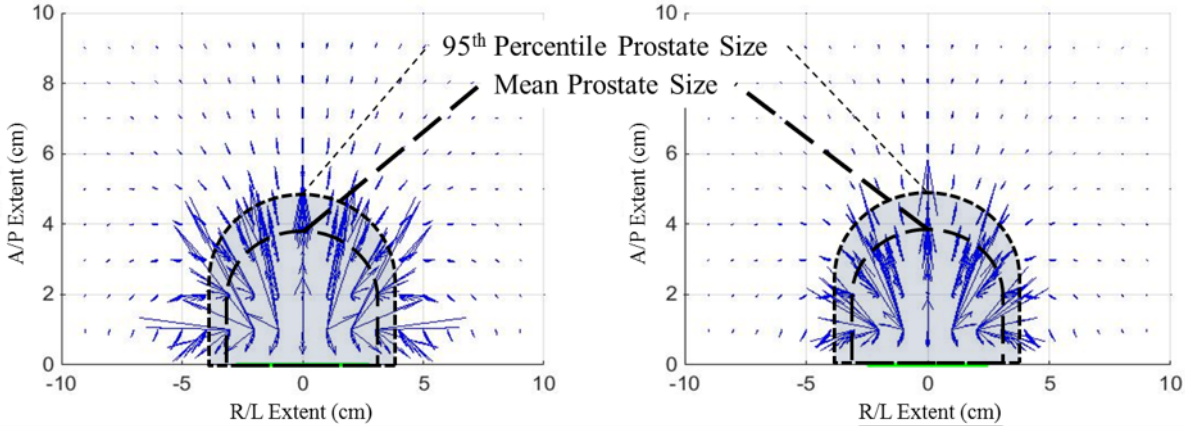

Figure 4.5: 2D views from MatLab simulations showing signal penetration in R/L and A/P for (left) the current single-loop ERC and (right) the proposed ERC design.

proposed design loses signal over the area of the prostate, the model created by averaging prostate shapes in Experiment 1 will be overlaid on the simulated magnetic field maps, and the magnetic field will be measured throughout the average gland. This will be repeated for the 95^{th} percentile prostate size and shape.

Experiment 4: assess and mitigate coupling between carbon and proton coils.

Because the proton frequency, ∼128 MHz, is close to the fourth harmonic of the carbon frequency, ∼32 MHz, at 3T, signal from proton reception has the capability to induce current in the carbon-sensitive elements. To protect from coupled currents in the ^{13}C coil shifting the resonant frequency and decreasing the SNR of the proton coil, an LC trap circuit can create an effective open circuit in the ^{13}C coil triggered at the proton frequency. Without current flow, the circuit will not generate a received electric signal. It may similarly be necessary to include trap circuits tuned to the carbon frequency on the proton coils. However, trap circuits present additional lumped circuitry and therefore resistance and potential for component failure.

Decoupling is not always necessary depending on distance and signal strength, so trap circuits will be planned but not included in simulation. Instead, once geometry and position of elements are settled in Experiments 1-4, a prototype will be built with proton- and carbon-sensitive elements. Current will be induced in each of the proton-sensitive elements and a network analyzer measuring S_{21} (forward voltage) will detect induced current in each carbon-sensitive element. Induced current in any carbon-sensitive element from any proton-sensitive element will trigger the need for a trap circuit. This experiment will be repeated to detect induced current in each proton-sensitive element from each carbon-sensitive element, and necessary trap circuits will be included.

4.3 Future Directions

With an ERC using multiple elements at the proton and carbon frequencies, every 3D sequence in the mpMRI of the prostate can be shortened. However, optimal conditions for acceleration will vary between the sequences and will therefore require extensive testing. As an example, it may be more optimal for data collection to utilize the time saved in DCE to acquire additional slices than are currently available, or it may be more valuable to increase spatial resolution in 3D anatomic imaging to facilitate reconstruction to the coronal and sagittal planes.

Early-phase clinical trials on hyperpolarized ^{13}C-MRSI efficacy in human prostate cancer are ongoing at our institution. Utilization of this coil in conjunction with these trials would provide the means of testing in-human performance in carbon-sensitive imaging and the limits of practical acceleration and therefore, spatial resolution. These clinical trials include patients intending to undergo radical prostatectomy, meaning performance versus the currently-available ERC can be tested using whole-mount pathology as a gold standard.

As a final direction, it is desirable to create the most comfortable probe. Using an inflatable balloon probe to house the ERC could increase patient comfort, and therefore patient compliance in completing the mpMRI. Options including flexible braided wires and printed circuit boards on flexible materials should be explored for application in the proposed design.

Chapter 5

The Rate of Hyperpolarized [1-^{13}C]Pyruvate to [1-^{13}C]Lactate Conversion Distinguishes High-Grade from Low-Grade Prostate Cancer in Patients

Abstract

There is a pressing clinical need to distinguish aggressive cancers from indolent cancers in the prostate to avoid diminishing quality-of-life and costly overtreatment. In this work, we present results from a phase 2 clinical trial of hyperpolarized [1-^{13}C]pyruvate magnetic resonance imaging, and quantitatively measure real-time metabolomics in prostate cancers and regions of benign tissue. Twenty-three patients underwent a 3T multiparametric ^{1}H/^{13}C MRI of the prostate followed by radical prostatectomy and whole-mount pathological grading. Carbon imaging parameters of overall lactate (AUC_{Lac}), lactate/pyruvate ratio ($\mathrm{AUC}_{Lac/Pyr}$), and the modeled rate of flux from pyruvate to lactate, (k_{PL}), were measured in eighteen high-grade lesions, thirteen low-grade lesions, and twenty-three benign regions.

Mixed linear models characterized differences between tissue types while controlling for data partially-paired by patient. Low-grade cancers had significantly higher values of all carbon metrics compared to benign regions (AUC_{Lac}, $AUC_{Lac/Pyr}$, and k_{PL}). While AUC_{Lac} was not significantly higher in high-grade disease, there was a significant difference in $AUC_{Lac/Pyr}$ ($p<0.025$), and a strongly significant difference in the k_{PL} ($p<0.0005$). This study demonstrated for the first time that k_{PL} is significantly elevated in high-grade prostate cancer versus both benign prostate tissue and low-grade disease, consistent with prior pre-clinical studies.

5.1 Introduction

While 164,690 men were estimated to be diagnosed with prostate cancer in the United States in 2018, only 18% ($\approx$ 29,430) of these patients will have aggressive disease resulting in death from prostate cancer [128]. Due to increased screening using serum prostate specific antigen (PSA) and extended-template TRUS-guided biopsies, patients with prostate cancer are being identified at an earlier and potentially more treatable stage. Despite a sharp fall in mortality since the start of the PSA-based early detection era in the US [128], prostate cancer early detection efforts have become controversial [129] [130], in part due to high rates of diagnosis and over-treatment of low-risk, indolent tumors, many of which would likely never have caused symptoms or loss of life had they remained undiagnosed. All treatments entail potential adverse effects on long-term quality of life (QOL) (e.g. erectile dysfunction, incontinence) [131] and for those with indolent disease, these effects come without the benefit of improved life expectancy. While those with indolent tumors can be managed with

active surveillance, approximately 30% of these patients will be reclassified as higher risk for disease progression, requiring definitive therapy [132] [133]. The aggressiveness of individual tumors cannot be predicted with great confidence using currently available clinical and imaging prognostic data. Current clinico-pathological variables including PSA levels, biopsy characteristics (grade and volume of disease), and stage of disease all provide important insight into disease risk [134], but unfortunately fail in discriminating aggressive versus indolent disease in many patients. The current state-of-the-art for imaging localized prostate cancer, multiparametric ^{1}H MRI, has demonstrated the ability to localize tumors for subsequent biopsy and treatment, but cannot consistently grade tumor aggressiveness accurately in individual patients [135]. There is an unmet clinical need for an accurate, non-invasive imaging method to detect aggressive, clinically significant cancer early in these patients so timely treatment of this potentially deadly metastatic disease can be initiated.

There is growing evidence that the ability of cancer cells to invade adjacent normal tissues and locally grow and metastasize to distant sites is significantly impacted by changes in tumor cellular metabolism [136]. Specifically, the Warburg effect, an up-regulation of aerobic glycolysis and production of lactate, the result of the lactate dehydrogenase (LDH) reaction, is an adaptation of cancer cells that aids in survival, growth, and metastases to a lethal phenotype [136]. Lactate dehydrogenase-A (LDHA), a protein subunit of the highly lactate-favoring LDH isoform muscle-type 5 (LDH-5), catalyzes the reduction of pyruvate to lactate and is overexpressed in many cancers, including prostate tumors [137] [138]. The Warburg effect is increased in prostate cancer due to key genomic changes that directly upregulate

LDHA expression: loss of the PTEN (phosphatase and tensin homolog) locus, leading to activation of the PI3K/AKT pathway in 70% of prostate cancers; and 8q amplification, including amplification of the Myc gene, which occurs in 30% of prostate cancers [139].

Hyperpolarized ^{13}C magnetic resonance spectroscopic imaging (HP ^{13}C MRSI) is a powerful new metabolic imaging method which uses specialized instrumentation to provide signal enhancements of over 10,000-fold using enriched, safe, endogenous, non-radioactive compounds [79]. While prostate cancer is often inadequately evaluated using FDG-PET (fluorodeoxyglucose-positron emission tomography); which assesses glucose uptake and phosphorylation [140] [141], HP ^{13}C MRSI detects down-stream metabolism, specifically the metabolic shift of prostate cancer cells from producing and secreting citrate to producing lactate [142] [143]. In a phase 1 clinical trial of HP [1-^{13}C]pyruvate MRSI, the metabolic rate of conversion of HP ^{13}C-pyruvate to ^{13}C-lactate, (k_{PL}), was shown to be significantly increased in regions of prostate cancer [80], however this clinical trial involved patients who did not receive surgery, therefore correlation of k_{PL} with pathologic grade was not possible.

In this manuscript we present the first patient data demonstrating the ability of k_{PL} to detect aggressive, high-grade (>20% Gleason pattern 4 disease) prostate cancer. A 3D dynamic hyperpolarized ^{13}C MRSI [82] / multiparametric ^{1}H MRI approach [115] was utilized to determine the k_{PL} associated with benign prostate tissue, low- and high-grade prostate cancer using whole-mount step section histopathology after surgery as the standard of reference.

5.2 Materials and Methods

This study was approved by the Committee on Human Research at this institution and was compliant with the Health Insurance Portability and Accountability Act. Written, informed consent was obtained from 23 subjects enrolled in a clinical trial entitled "A pilot study of magnetic resonance (MR) imaging with hyperpolarized pyruvate (^{13}C) to detect high-grade localized prostate cancer" (NCT02526368). Patients received a 3D dynamic hyperpolarized ^{13}C MRSI / multiparametric ^{1}H MRI exam acquired on a 3T MRI (GE Healthcare, Waukesha WI, USA) using a dual-tuned ^{1}H/^{13}C endorectal coil [144] in combination with a 4-channel ^{1}H pelvic array for reception and a ^{13}C Helmholtz configuration "clamshell" coil for ^{13}C excitation. Patients were instructed to eat a light diet for 24 hours before the exam and to perform a FLEET enema 1-3 hours before the exam.

A solution of 0.43 mL/kg [1-^{13}C]pyruvate was polarized for 120-210 minutes in a 5T SPINLab^{TM} hyperpolarizer (GE Healthcare, Waukesha WI, USA) and injected at a flow rate of 2 mL/s before a 20 mL saline flush. Sufficient EPA filtration and physiologic pH were confirmed by a pharmacist before injection.

Anatomic imaging was performed using a T_2-weighted fast spin-echo sequence with FOV = 18 cm, slice thickness = 3mm, matrix = 512 x 512, and TR/TE = 6000/96, prescribed at an obliquity matching the posterior edge of the prostate. Anatomic images were intensity-corrected for the endorectal coil profile [19].

Functional imaging (DWI and DCE MRI) was performed at the same obliquity and slice thickness as the anatomical T_2-weighted sequence. Six-direction diffusion-weighted imaging

(DWI) was acquired using a 2D single shot spin-echo sequence with a b-value of 600 s/mm^2, FOV = 18 cm, TR/TE = 4000/(minimum full TE) ms, slice thickness = 3mm. Additionally, a high b-value DWI was acquired using a 2D single shot spin-echo sequence with a b-value of 1350 s/mm^2, FOV = 26 cm, TR/TE = 4000/(minimum full TE) ms, slice thickness = 3mm. DCE MRI was acquired using a single dose of gadopentatate dimeglumine (Magnavist, Bayer Inc.) injected at 2 mm/sec with total injected amount determined by patient body weight. DCE MRI used a 3D fast SPGR sequence with a temporal resolution of 10.4 s, FOV = 46 cm, TR/TE = 3.5/0.9 ms, flip angle = 5°, with 5 timepoints acquired before injection to establish a baseline for semi-quantitative metrics.

The MR scanner was calibrated to the carbon frequency immediately before dissolution, based on signal from a 660 μL of 8 M ^{13}C-urea standard embedded in the endorectal coil. 3D dynamic carbon imaging was performed using a dualband spectral-spatial pulse sequence with a variable flip angle to conserve non-replenishing SNR, followed by an echo-planar spectroscopic imaging (EPSI) readout with compressed sensing in both the spatial and temporal dimensions for a total 288-fold acceleration over full-sampled conventional spectroscopic imaging [82]. This acquisition scheme covers the entire prostate with 8mm^3 resolution and 2 s temporal resolution over 21 timepoints.

Hyperpolarized carbon data were reconstructed using an in-house MATLAB routine [145]. After accounting for frequency drift due to transmit field heterogeneity, the pyruvate and lactate signal at each timepoint was measured as the integrated area under the curve of the real component of a phase-corrected spectrum. The exam noise was calculated as the

pyruvate signal in next-to-edge slices in the first timepoint of acquisition, presumably before the pyruvate bolus.

Image maps of the total area under the curve over time of pyruvate (AUC_{Pyr}) and lactate (AUC_{Lac}) were intensity-corrected for the endorectal receive coil profile [19]. A Lactate/Pyruvate AUC Ratio map ($\mathrm{AUC}_{Lac/Pyr}$) was created as a ratiometric surrogate for metabolic conversion, and an uncorrected SNR_{Pyr} map based on the AUC_{Pyr} and calculated exam noise was used as a check on voxel quality:

$$SNR_{Pyr} = \frac{AUC_{Pyr}}{\sigma(noise)} \tag{5.1}$$

An inputless, two-compartment kinetic model was built to measure the pyruvate-to-lactate conversion rate, k_{PL} [146]. The two-site exchange model accounts for uni-directional conversion of pyruvate to lactate, signal loss due to serial RF excitations, and the spin-lattice relaxation (T_1) of pyruvate and lactate. At each timepoint, the available pyruvate magnetization serves as the input function, and the available pyruvate and estimated lactate at the previous timepoint are used to estimate the available lactate. A hybrid discrete-continuous model accounts for the variable flip angle acquisition scheme by using the magnetization immediately prior to each RF pulse to compute the magnetization available after each RF pulse [147]. Confidence intervals and a coefficient of determination for each k_{PL} measurement based on the nonlinear least-squares curve-fitting between true and modeled lactate were also mapped for quality control during ROI analysis.

After radical prostatectomy, whole-mount resections were sliced at 3mm resolution to

match T_2-weighted imaging, and regions of cancerous and noncancerous tissue were labeled by Gleason score and percent cancer by a licensed pathologist. Regions-of-Interest (ROIs) were manually translated from whole-mount pathology onto high-resolution T_2-weighted images, and propagated to image maps of carbon metrics after 3D rigid registration based on a urea phantom embedded in the endorectal coil and nearest-neighbor interpolation to the high-resolution T_2-weighted image.

A variety of checks were implemented to control the quality of carbon data analyzed in this clinical trial. Carbon image maps were sinc-interpolated by 2, and only voxels with 25% area or more in the ROI were included in the analysis of that ROI. Additionally, only voxels with an SNR_{Pyr} over 105, (an average SNR_{pyr} of 5 per timepoint over 21 timepoints), were included. Voxels with proportionally large confidence intervals or low coefficients of determination were determined to have poor fit quality, and were excluded from analysis.

The maximum value of each carbon parameter in an ROI was used to represent the region, similar to injected agents used in PET imaging [148]. For regions spanning ROIs on multiple slices, the overall grade was calculated based on the size, percent cancerous tissue, and percent Gleason grade of each ROI on each slice. Cancerous lesions with 20% Gleason pattern 4 disease or higher were considered high-grade, aggressive cancers in this study.

Differences in metabolism between benign tissue and low-grade cancers, and between low-grade and high-grade cancers were characterized by mixed linear effects analyses to account for data partially-paired by patient and Bonferroni corrected for multiple comparisons. Significance was determined by likelihood ratio tests between models with a fixed effect of cancer

grade and models without. To evaluate the ability of k_{PL} to predict aggressive prostate cancer, k_{PL} values were normalized to the region of normal tissue for each patient, and ROC analyses were performed and compared to the predictive ability of mean water ADC and a linear combination of k_{PL} (normalized to benign tissue) and mean ADC. Statistics were performed in python (Python Software Foundation, Python Language Reference, version 3) and R (R, Inc., Boston, MA © 2016).

5.3 Results

Twenty-three patients underwent a multiparametric MRI with ^{13}C-MRSI at our institution. Patients presented at an average 66 ± 7.5 years of age, with an average PSA of 8.4 ± 5.2 ng/mL. Seventeen patients presented with a PI-RADS score of 5, 4 patients presented with a PI-RADS score of 4, and 2 patients presented with a PI-RADS score of 3 based on a clinical mpMRI. The clinical information of all patients is summarized in Table 5.1.

The average time to injection for [1-^{13}C]pyruvate in this patient cohort was 62.3s (range 49 to 83s); injection time was 67.6s, (range 43 to 88s), in the phase 1 trial (18). The injection had an average volume of 34 ± 3.0 mL, an average pyruvate concentration of 237 ± 11.4 mM, and a ^{13}C polarization of 38 ± 6.0% (17.8 ± 3% polarization was obtained in the phase 1 trial [80]). From these twenty-three patients, eighteen high-grade tumors, thirteen low-grade tumors and twenty-three regions of non-cancerous tissue—one in each patient—were identified.

A representative patient with high-grade prostate cancer is shown in Figure 5.1. A

Gleason 4+5 lesion was observed in the right posterior aspect of the peripheral zone extending from the apex through the base of the prostate on whole-mount step section pathology. The corresponding T_2-weighted and ADC image demonstrates a clear region of reduced T_2 signal intensity and ADC (ADC = 1327 $\pm$ 342 10^{-3} mm^2/s) in the same location as the region of the Gleason 4+5 pathologic lesion. Based on the mpMRI findings, this lesion was given a PI-RADS score of 5. Correspondingly there was an elevation of k_{PL} (0.0052 $\pm$ 0.0019 s^{-1}) which was clearly visualized on the T_2-weighted images overlaid with a map of normalized k_{PL} in the same spatial location as the ADC and pathologic abnormalities, with a k_{PL} within the lesion of 275% that of the normal tissue in this patient. Interestingly, there was a great deal of heterogeneity in ADC and k_{PL} across this large high-grade lesion and the region of lowest ADC did not correlate with the region of highest k_{PL}.

A representative patient with low-grade prostate cancer is shown in Figure 5.2. A Gleason 3+3 lesion was observed in the right posterior midgland close to the midline on whole-mount step section pathology. The corresponding T_2-weighted and ADC images demonstrated a region of reduced T_2 signal intensity and ADC (ADC = 1439 $\pm$ 165 10^{-3} mm^2/s) in the same location as the region of the Gleason 3+3 pathologic lesion. The magnitude of reduction in T_2 signal intensity and water ADC were less than the high-grade patient's tumor in Figure 5.1, consistent with low-grade disease, however this lesion was still clear enough to be given a PI-RADS score of 4. There was a corresponding elevation of k_{PL} (0.0104 $\pm$ 0.0019 s^{-1}) which was clearly visualized on the T_2-weighted images overlaid with a map of normalized k_{PL} in the same spatial location as the ADC and pathologic abnormalities, with a k_{PL} in

Table 5.1: Clinical presentation of 23 patients after multiparametric MRI of the prostate and radical prostatectomy with whole-mount resection.

Age	High-Grade Lesion	Low-Grade Lesion	PSA	ECE	PNI	SVI
70	G4+4	G3+4	26.2	Yes	Yes	No
60	G4+3	G3+3	7.32	Yes	Yes	No
60		G3+4	5.01	Yes	Yes	No
74	G4+4	G3+3	3.71	No	Yes	No
77	G5+4		16.3	Yes	Yes	Yes
75	G4+3		1.13	No	Yes	No
70	G5+4		7.31	Yes	Yes	Yes
67	G4+4	G3+3	7.35	No	Yes	No
53		G3+3	6.32	No	Yes	No
71	G5+4		8.62	Yes	Yes	No
55		G3+3	7.22	Yes	Yes	No
56		G3+4	7.96	Yes	Yes	No
70		G3+4	4.80	Yes	Yes	No
56	G4+3	G3+3	10.9	No	No	No
65	G4+3	G3+3	6.47	Yes	Yes	No
73	G5+4		5.62	Yes	Yes	Yes
66	G5+4	G3+4	12.1	Yes	Yes	No
78	G5+4		7.49	Yes	Yes	Yes
62	G4+3	G3+3	4.20	Yes	Yes	Yes
73	G4+3		12.6	Yes	Yes	No
61	G4+3		12.9	Yes	Yes	No
59	G4+3		4.19	No	Yes	No
68	G4+5		7.12	Yes	Yes	Yes

the lesion of 140% that of the normal tissue in this patient. The k_{PL} across this smaller low-grade tumor was more homogenous than in the high-grade tumor.

A summary of the maximum AUC_{Lac}, $\text{AUC}_{Lac/Pyr}$, and k_{PL} values in benign tissue, low-grade prostate cancers, and high-grade prostate cancers, is provided in Table 5.2 and Figure 5.3. The maximum value in each HP carbon parameter, AUC_{Lac}, $\text{AUC}_{Lac/Pyr}$, and k_{PL}, increased from benign to low-grade cancer and from low-grade to high-grade cancer. AUC_{Lac} was the most variable carbon metric for all three tissue types (benign, low- and

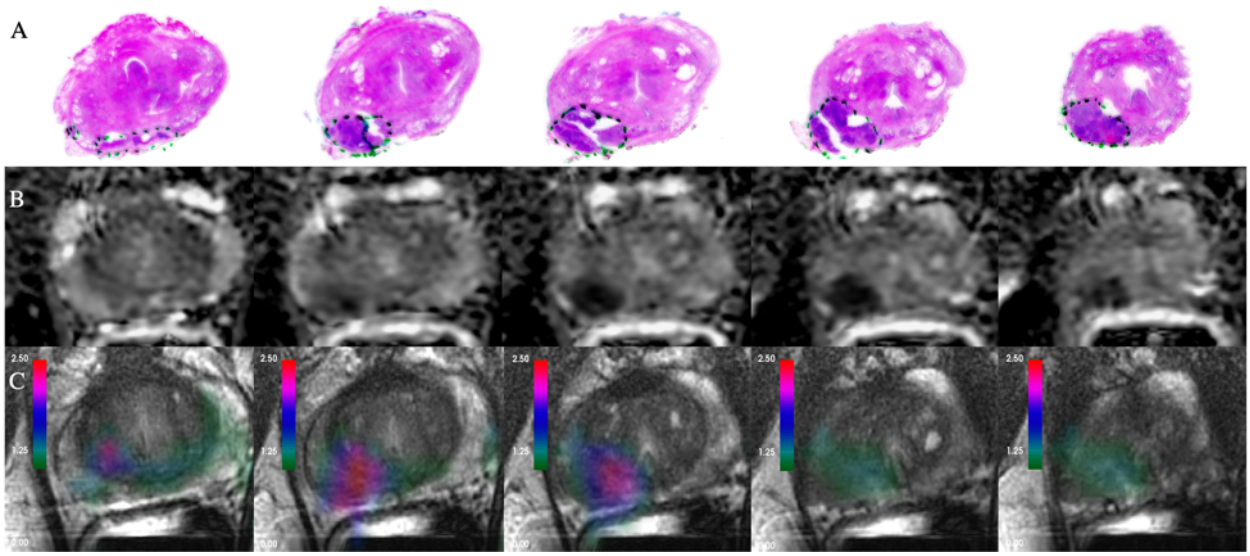

Figure 5.1: A 68-year-old patient with a PSA of 7.12 ng/mL, Gleason 4+5 prostate cancer in the left peripheral zone from base to apex (pT3bN1, ECE, SVI) at step section pathology (**A**) after surgery, PI-RADS 5 on mpMRI, k_{PL} = 275% of normal. The **B** ADC map clearly shows the region of tumor, and **C** the normalized k_{PL} maps overlaid on T_2-weighted images showed a region of elevated k_{PL} over the lesion identified by ADC and whole-mount pathology.

high-grade cancer), and was significantly elevated in low-grade cancer relative to benign prostate tissues but not between low- and high-grade disease. $\text{AUC}_{Lac/Pyr}$ and k_{PL} both demonstrated significant increases from benign prostate tissue to low-grade prostate cancer and between low- and high-grade disease. The maximum $\text{AUC}_{Lac/Pyr}$ was 61 ± 22% higher in low-grade cancer relative to benign tissue ($p \leq 0.0005$), and 27 ± 34% higher in high-grade relative to low-grade cancers ($p \leq 0.025$). The maximum k_{PL} in a region was 63 ± 19% higher in low-grade cancer relative to benign tissue ($p \leq 0.0005$), and provided the best separation of high- and low-grade cancer, 33 ± 16% higher in high-grade disease ($p \leq 0.0005$).

Although all of the tumors investigated using HP [1-^{13}C]pyruvate MRI in this study were

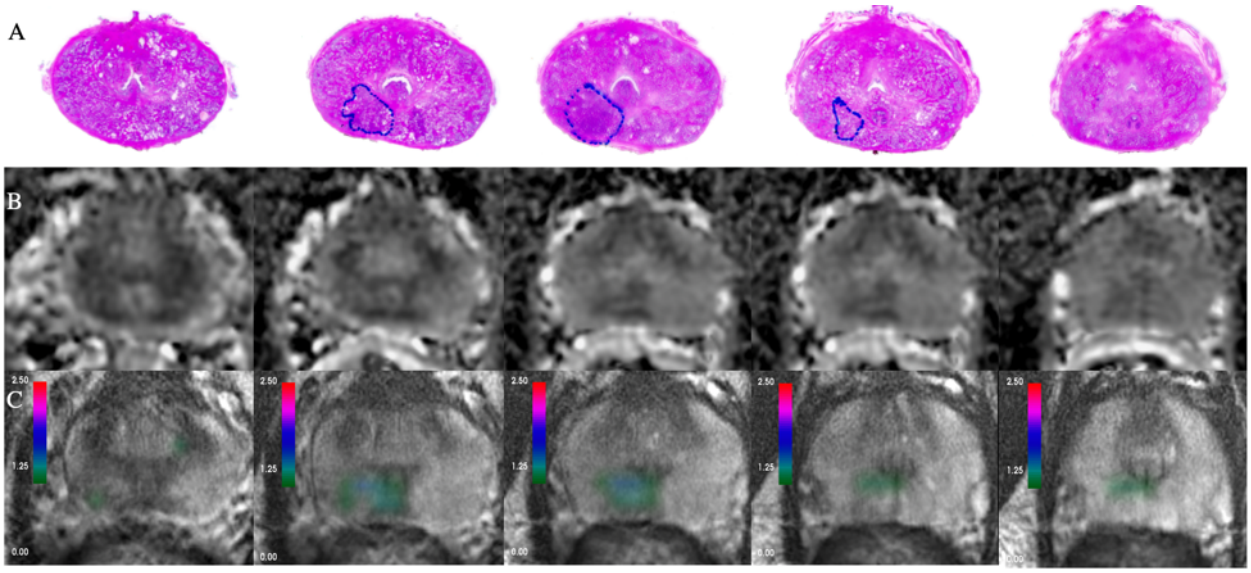

Figure 5.2: A 53-year-old patient with a PSA of 6.32ng/mL, and Gleason 3+3 prostate cancer in the right peripheral zone of the midgland (pT2bN0) at step section pathology **A** after surgery, PI-RADS score of 4 on mpMRI, and a k_{PL} 140% of normal. The **B** ADC map shows diffusely reduced ADC consistent with low-grade disease, and the **C** normalized k_{PL} map overlaid on a T_2-weighted image shows moderately increased k_{PL} over the lesion identified by ADC and whole-mount pathology.

Table 5.2: Means and standard deviations of carbon parameters in 23 normal peripheral zone, 13 low-grade, and 18 high-grade prostate cancers.
Significantly different between benign and low-grade cancer: '†' 0.025 '†††' 0.0005
Significantly different between low- and high-grade cancer: '$*$' 0.025 '$***$' 0.0005

Carbon Parameter		**Tissue Type**	
Mean ± Std. Dev.	**Normal Peripheral Zone**	**Low-Grade Prostate Cancers**	**High-Grade Prostate Cancers**
$\mathbf{AUC}_{Lac}$	59.32 ± 40.70 a.u.	96.10 ± 59.92 †	116.7 ± 82.55
$\mathbf{AUC}_{Lac/Pyr}$	0.245 ± 0.110	0.388 ± 0.144 †††	0.453 ± 0.285 $*$
k_{PL}	0.0082 ± 0.0029 s^{-1}	0.0134 ± 0.0049 †††	0.0165 ± 0.0102 $***$

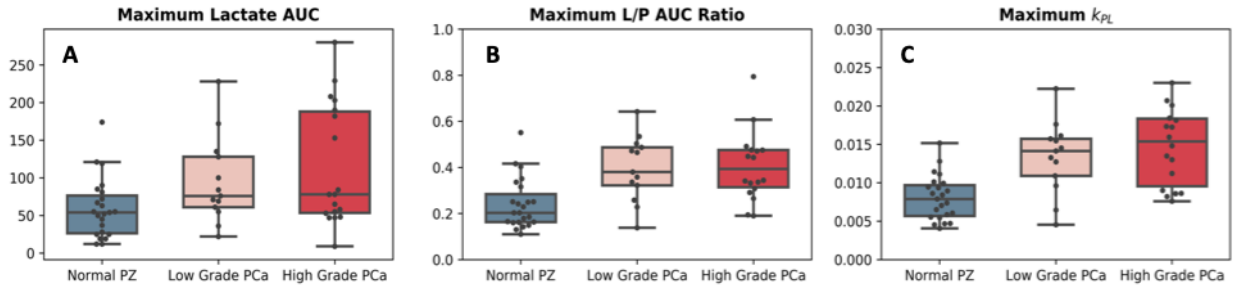

Figure 5.3: Box plot of the maximum values of carbon parameters; **A** AUC_{Lac}, **B** $AUC_{Lac/Pyr}$, and **C** k_{PL} for 23 benign prostate tissues, 13 low- and 18 high-grade prostate tumors.

identified by ^{1}H mMRI, there were several cases in which there were spatial mismatches in maximum k_{PL} and low ADC. There were also several cases in which small volume Gleason 3+3 tumors were missed by both mpMRI and HP [1-^{13}C]pyruvate MRI. A representative example of both these scenarios is shown in Figure 5.4. While both the ADC map and the k_{PL} map overlaying the T_2-weighted image identify bilateral disease in Figure 5.4, the mean ADC in the Gleason 3+4 lesion was 1011 10^{-3} mm^2/s, much lower than the mean ADC of 1360 10^{-3} mm^2/s in the Gleason 5+4 lesion. The smaller, more aggressive Gleason 5+4 lesion had a higher maximum k_{PL} of 0.023 s^{-1}, 423% of benign prostate tissue as compared to the G3+4 lesion which had a maximum k_{PL} of 0.016 s^{-1}, 284% of benign tissue. The small, anterior Gleason 3+3 lesion was not determined to be abnormal on either ADC or k_{PL}.

Two of the three tumors with an equivocal PI-RADS score of 3 were found in the same patient, a Gleason 3+3 and a Gleason 4+3 lesion, but this patient presented with extra-capsular extension and perineural invasion. The other PI-RADS 3 lesion was identified as Gleason 4+3 on whole-mount pathology. While these three tumors had the same PI-RADS

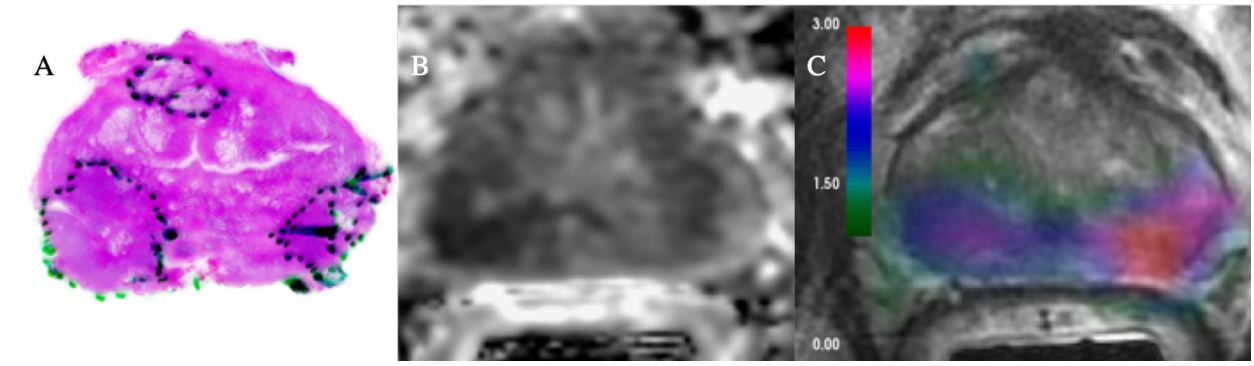

Figure 5.4: A 70 year old patient with a PSA of 7.31 ng/mL, and multifocal prostate cancer at whole-mount step-section pathology after surgery **A**; Gleason 5+4 (50% Gleason 5) in the left posterior midgland, Gleason 3+4 cancer (40% Gleason 4) in the right posterior midgland and Gleason 3+3 in the right anterior midgland, with a surgical stage of pT2bN0. Water ADC **B** had the most dramatic reduction in the G3+4 tumor while **C** k_{PL} was the most elevated in the G5+4 tumor.

scores, they had dramatically different maximum k_{PL}, values (0.0127, 0.0159 and 0.0184 s^{-1}), and the k_{PL} values were higher than the average maximum k_{PL} value in low-grade cancers.

Both the maximum, normalized k_{PL} and the mean ADC predicted aggressive disease in this cohort of patient with an overall area under the ROC of 0.68, and combining k_{PL} and ADC yields an area under the ROC of 0.75. The difference in sensitivity and specificity between ADC and k_{PL} ROC curves suggest that these imaging parameters provide complementary information.

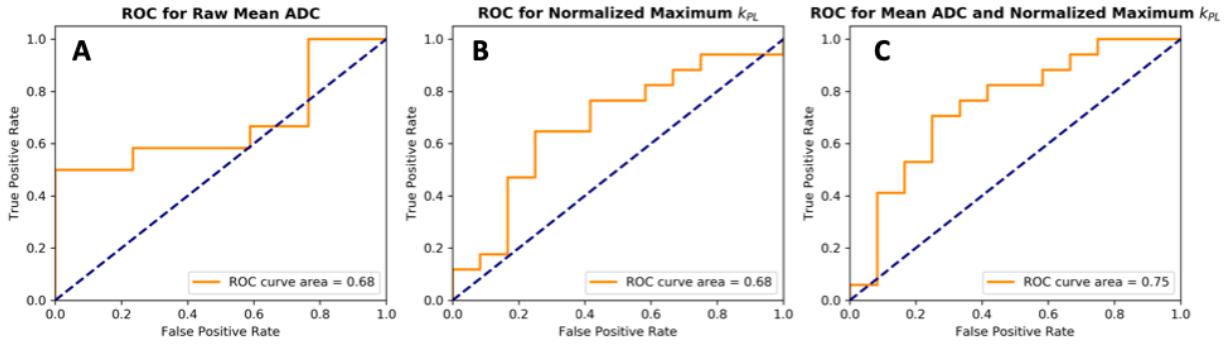

Figure 5.5: ROC analyses; **A** mean ADC, **B** normalized maximum k_{PL} , and **C** combined mean ADC and normalized maximum k_{PL}.

5.4 Discussion

A pressing need facing the clinical management of prostate cancer patients is an accurate imaging method for distinguishing aggressive, high-grade prostate cancer from indolent disease at the time of diagnosis. Current standard-of-care prostate cancer ^{1}H multiparametric MRI includes T_2- and diffusion-weighted imaging and dynamic contrast-enhanced sequences, interpreted using the PI-RADS framework [149] [150] [151]. This method is highly effective in detecting and localizating prostate cancer for subsequent biopsy, but is limited by poor detection of small volumes of high-grade disease, and the inability to reliably grade lesions based on imaging parameters [135] [152] [153] [154]. High- spatial and temporal resolution 3D dynamic hyperpolarized ^{13}C MRSI has previously demonstrated the ability to correlate the rate of hyperpolarized (HP) [1-^{13}C]pyruvate to [1-^{13}C]lactate conversion, k_{PL}, with the pathologic grade of prostate cancer in a murine model [155]. A phase 1 clinical trial of HP [1-^{13}C]pyruvate (NCT01229618) in biopsy-proven prostate cancer patients demonstrated both the safety and feasibility of imaging cancer within the prostate, discriminating prostate

cancer from benign tissue based on significantly elevated k_{PL} obtained from 2D dynamic ^{13}C spectroscopic imaging data, but with only biopsy-based pathology correlations [80]. In this manuscript, the k_{PL} associated with benign prostate tissue, low-grade (<20% Gleason pattern 4), and high-grade prostate cancer in patients was determined using whole-mount step section histopathology after surgery as the standard of reference.

A number of significant technical improvements were implemented in this study relative to the phase 1 trial, including use of improved strategies and technology for generating sterile hyperpolarized material using a commercial 5T DNP polarizer (SPINlab^{TM}), automated injection of HP [1-^{13}C]pyruvate, and use of a new 3D-CSI EPSI dynamic hyperpolarized ^{13}C MRSI sequence [82]. These improvements lead to a doubling of the [1-^{13}C]pyruvate polarization and a 7.8% reduction in HP [1-^{13}C]pyruvate injection time thereby allowing the acquisition of high spatial and temporal resolution 3D-CSI EPSI with full prostate gland coverage. Using a inputless, two-compartment kinetic model [146] and an appropriate pyruvate SNR threshold (SNR$_{pyr}$ over 105, an average SNR$_{pyr}$ of 5 per timepoint over 21 timepoints), k_{PL} maps were robustly calculated, overlaid on the corresponding T_2 weighted anatomic images and correlated with the digitized whole-mount step section pathology providing the first report of the relationship between k_{PL} and pathologic grade in prostate cancer patients. In addition, the ability of k_{PL} to discriminate prostate cancer and it's aggressiveness was compared to two hyperpolarized carbon parameters (AUC$_{Lac}$ and AUC$_{Lac/Pyr}$) that have been used in prior hyperpolarized ^{13}C MR studies to assess the increased rate of conversion of HP pyruvate to [1-^{13}C]lactate associated with prostate cancer presence and progression.

All three HP carbon parameters investigated in this study, AUC_{Lac}, $AUC_{Lac/Pyr}$, and k_{PL}, increased with the development of prostate cancer and with progression from low- to high-grade cancer consistent with prior HP [1-^{13}C]pyruvate MR pre-clinical studies [81] [82] [118]. In this study, AUC_{Lac} was the most variable carbon metric for assessing increased lactate production and was significantly increased in cancer relative to benign prostate but not between low- and high-grade cancer. Both $AUC_{Lac/Pyr}$ and k_{PL} significantly increased in high- versus low-grade prostate cancer and k_{PL} demonstrated the best discrimination of high- and low-grade prostate cancer, indicating the benefit of correcting for pyruvate delivery and modeling the dynamic HP [1-^{13}C]pyruvate data.

Of the mpMRI parameters, water ADC has shown the greatest promise for reflecting the pathologic grade of prostate cancer, with lower ADC values found in higher Gleason grade cancers [156] [157] [158] [159]. In this study, k_{PL} and water ADC predicted high-grade (Gleason score $\geq$ 4+3) disease in this cohort of patients with the same accuracies (ROC of 0.68). However, the differences in sensitivity and specificity observed between the ADC and k_{PL} ROC curves, and the fact that we observed spatial mismatches between lowest ADC and highest k_{PL} in individual tumors, suggest that these imaging parameters provide complementary information. Moreover, combining k_{PL} and ADC increased the accuracy of predicting high-grade disease over either technique alone (ROC of 0.75).

Several limitations of our study are worth mentioning. First, the prostate cancer patient population studied was heavily weighted towards patients with more advanced disease (Table 5.1), since this is the patient population that currently receive surgery at our institution.

Specifically, there were only three Gleason 3+3 tumors studied in the low-grade patient cohort, with the remaining low-grade tumors containing up to 20% Gleason pattern 4. Additionally, the Gleason 3+3 tumors studied were associated with more aggressive pathologic features, i.e., large volume ($\geq$ 0.5cc) disease, adjacent extracapsular extension or perineural invasion, and high-grade disease in other parts of the gland. A prior published pre-clinical study indicated a lack of significant increase in the HP Lac/Pyr ratio (i.e., the Warburg effect) in low-grade prostate cancer versus benign prostate tissue, with significance only occurring with progression to aggressive, high-grade disease [118]. This finding is consistent with prior publications suggesting that the Warburg effect does not become important in prostate cancer until late-stage/high-grade disease [160] [161] [162] [163]. These publications argue that early-stage/low-grade (Gleason 3+3) prostate cancers rely on lipids and other biologic fuels for energy production, and that the glycolytic phenotype is only associated with the evolution of aggressive disease [164] [165]. Taken together these findings suggest that the k_{PL} observed for the low-grade tumors in this study are higher, and the difference between low- and high-grade disease smaller, than what would be expected for a cohort of patients with truly low-grade/indolent (Gleason 3+3) disease. This hypothesis is being tested in a recently initiated HP [1-^{13}C]pyruvate MRI study of prostate patients with early-stage/indolent disease selecting or on active "active surveillance" as their clinical management course and receiving MRI/TRUS fusion biopsy as the pathologic standard of reference (NCT03933670).

Another potential limitation of this study was the spatial resolution of the 3D dynamic HP MR data acquired ($\approx$ 0.5cc) which could impact k_{PL} and the other HP ^{13}C parameters

studied due to partial voluming of the region of interest (benign or malignant) with surrounding tissues. Partial volume effects were minimized by using the maximum values of the HP ^{13}C parameters for analyses, similar to what is done with SUV_{max} in positron emission tomography (PET) [148]. Nevertheless, the HP ^{13}C MRI spatial resolution was sufficient for us to capture significant differences in k_{PL} between benign, low- and high-grade cancer as well as heterogeneity in k_{PL} within individual lesions. Additionally, advances in HP ^{13}C MRI imaging technology will reduce the achievable voxel size, and higher resolution ($\approx$ 0.3cc) 3D HP ^{13}C EPI [166] studies of the human prostate are being implemented.

In conclusion, high spatial and temporal resolution 3D dynamic hyperpolarized [1-^{13}C]pyruvate MRSI with full prostate coverage can be obtained, and the 3D dynamic data modeled, to produce maps of the apparent rate of conversion of pyruvate to lactate (k_{PL}). This study demonstrated for the first time that k_{PL} is significantly elevated in high-grade prostate cancer versus both benign prostate tissue and low-grade disease, consistent with what was observed in a prior pre-clinical studies [81] [82] [118] and confirming the observations of the initial phase 1 clinical trial of HP[1-^{13}C]pyruvate in prostate cancer patients (NCT01229618) [80]. The k_{PL} values determined for benign, low- and high-grade prostate cancer can be used to design future patient studies to assess the utility of k_{PL} in combination with other multi-parametric MRI parameters, to best select patients for surveillance or aggressive treatment, and to quantify early therapeutic response or failure.

Conclusion

The multiparametric MRI offers unique information to clinicians and patients about the spread, functionality, and energetics of prostate cancers, however ambiguous disease staging can lead to unnecessary invasive diagnostic metrics and overtreatment of prostate cancer.

In Chapter 1, we outlined the current state of the art of the multiparametric MRI of the prostate, with high resolution anatomic imaging in conjunction with functional diffusion-weighted imaging, dynamic contrast-enhanced MRI (DCE MRI), and proton magnetic resonance spectroscopic imaging (^{1}H-MRSI). In Chapter 2, we provided an improvement to the diffusion-weighted imaging portion of the multiparametric MRI. By limiting the number of phase encodes, and by using the chemical shift between water and fat to only refocus the water signal, we can significantly reduce the susceptibility artifact on resulting apparent diffusion coefficient maps. In Chapter 3, we showed how to use diffusion and DCE MRI to distinguish chronic inflammation, a common confounder in prostate cancer MRI diagnostics, from low-grade prostate cancers. In Chapter 4, we conceptualized and simulated a novel radiofrequency receive coil array to translate hyperpolarized ^{13}C imaging to the clinic. We showed that a three-element longitudinal design will allow parallel imaging, greatly increasing the amount of available signal during the non-renewable hyperpolarized signal decay and resulting in a usable clinical resolution for hyperpolarized carbon imaging of the human prostate. In Chapter 5 we show initial results from the first phase 2 clinical trial of ^{13}C in the

characterization of prostate cancer aggressiveness, showing a unique ability to quantitatively measure differences in real-time tissue metabolism. Together, these techniques improve the precision with which we use the multiparametric MRI to grade prostate cancer, aiding in the management of clinical patients.

Bibliography

[1] Jelle O Barentsz et al. "ESUR prostate MR guidelines 2012". In: *European radiology* 22.4 (2012), pp. 746–757.

[2] Louise Dickinson et al. "Scoring systems used for the interpretation and reporting of multiparametric MRI for prostate cancer detection, localization, and characterization: could standardization lead to improved utilization of imaging within the diagnostic pathway?" In: *Journal of Magnetic Resonance Imaging* 37.1 (2013), pp. 48–58.

[3] Annette Fenner. "Prostate cancer: multiparametric MRI scans could be a useful adjunct for active surveillance in prostate cancer". In: *Nature Reviews Urology* 10.5 (2013), p. 247.

[4] Caroline MA Hoeks et al. "Prostate cancer: multiparametric MR imaging for detection, localization, and staging". In: *Radiology* 261.1 (2011), pp. 46–66.

[5] Kiri Sandler et al. "Multiparametric-MRI and targeted biopsies in the management of prostate cancer patients on active surveillance". In: *Frontiers in oncology* 5 (2015), p. 4.

[6] Jason C Crane, Marram P Olson, and Sarah J Nelson. "SIVIC: open-source, standards-based software for DICOM MR spectroscopy workflows". In: *Journal of Biomedical Imaging* 2013 (2013), p. 12.

[7] O Rouvière. "Imaging techniques for local recurrence of prostate cancer: for whom, why and how?" In: *Diagnostic and interventional imaging* 93.4 (2012), pp. 279–290.

[8] Antonio C Westphalen et al. "Multiparametric 3T endorectal mri after external beam radiation therapy for prostate cancer". In: *Journal of Magnetic Resonance Imaging* 36.2 (2012), pp. 430–437.

[9] Glenn J Bubley et al. "Accuracy of endorectal magnetic resonance/transrectal ultrasound fusion for detection of prostate cancer during brachytherapy". In: *Urology* 81.6 (2013), pp. 1284–1290.

[10] T Barrett et al. "DCE and DW MRI in monitoring response to androgen deprivation therapy in patients with prostate cancer: a feasibility study". In: *Magnetic resonance in medicine* 67.3 (2012), pp. 778–785.

[11] Ansgar Rudisch et al. "Metallic artifacts in magnetic resonance imaging of patients with spinal fusion: a comparison of implant materials and imaging sequences". In: *Spine* 23.6 (1998), pp. 692–699.

[12] Elisabetta Panfili et al. "Magnetic resonance imaging (MRI) artefacts in hip prostheses: a comparison of different prosthetic compositions". In: *La radiologia medica* 119.2 (2014), pp. 113–120.

[13] American College of Radiology et al. "MR prostate imaging reporting and data system version 2.0". In: *ACR Webpage* (2015).

[14] Yousef Mazaheri et al. "Prostate tumor volume measurement with combined T2-weighted imaging and diffusion-weighted MR: correlation with pathologic tumor volume". In: *Radiology* 252.2 (2009), pp. 449–457.

[15] Jeffrey C Weinreb et al. "Prostate cancer: sextant localization at MR imaging and MR spectroscopic imaging before prostatectomy—results of ACRIN prospective multi-institutional clinicopathologic study". In: *Radiology* 251.1 (2009), pp. 122–133.

[16] Hedvig Hricak et al. "Imaging prostate cancer: a multidisciplinary perspective". In: *Radiology* 243.1 (2007), pp. 28–53.

[17] Susan M Noworolski et al. "A clinical comparison of rigid and inflatable endorectal-coil probes for MRI and 3D MR spectroscopic imaging (MRSI) of the prostate". In: *Journal of Magnetic Resonance Imaging: An Official Journal of the International Society for Magnetic Resonance in Medicine* 27.5 (2008), pp. 1077–1082.

[18] Yael Rosen et al. "3T MR of the prostate: reducing susceptibility gradients by inflating the endorectal coil with a barium sulfate suspension". In: *Magnetic Resonance in Medicine: An Official Journal of the International Society for Magnetic Resonance in Medicine* 57.5 (2007), pp. 898–904.

[19] Susan M Noworolski et al. "Post-processing correction of the endorectal coil reception effects in MR spectroscopic imaging of the prostate". In: *Journal of Magnetic Resonance Imaging* 32.3 (2010), pp. 654–662.

[20] Zarine K Shah et al. “Performance comparison of 1.5-T endorectal coil MRI with 3.0-T nonendorectal coil MRI in patients with prostate cancer”. In: *Academic radiology* 22.4 (2015), pp. 467–474.

[21] Baris Turkbey et al. “Comparison of endorectal coil and nonendorectal coil T2W and diffusion-weighted MRI at 3 Tesla for localizing prostate cancer: correlation with whole-mount histopathology”. In: *Journal of Magnetic Resonance Imaging* 39.6 (2014), pp. 1443–1448.

[22] Louise Dickinson et al. “Magnetic resonance imaging for the detection, localisation, and characterisation of prostate cancer: recommendations from a European consensus meeting”. In: *European urology* 59.4 (2011), pp. 477–494.

[23] Matthias C Roethke et al. “Prostate magnetic resonance imaging at 3 Tesla: Is administration of hyoscine-N-butyl-bromide mandatory?” In: *World journal of radiology* 5.7 (2013), p. 259.

[24] Christopher Lim et al. “Does a cleansing enema improve image quality of 3T surface coil multiparametric prostate MRI?” In: *Journal of Magnetic Resonance Imaging* 42.3 (2015), pp. 689–697.

[25] D.G. Nishimura. *Principles of magnetic resonance imaging*. Stanford University, 1996. URL: https://books.google.ca/books?id=uz9BAQAAIAAJ.

[26] Vasiliki Pasoglou et al. “Whole-body 3D T1-weighted MR imaging in patients with prostate cancer: feasibility and evaluation in screening for metastatic disease”. In: *Radiology* 275.1 (2014), pp. 155–166.

[27] Blanca Paño et al. “Pathways of lymphatic spread in male urogenital pelvic malignancies”. In: *Radiographics* 31.1 (2011), pp. 135–160.

[28] Ali-Reza Sharif-Afshar et al. “Impact of post prostate biopsy hemorrhage on multiparametric magnetic resonance imaging”. In: *Can J Urol* 22.2 (2015), pp. 7698–7702.

[29] Maarten de Rooij et al. “Accuracy of magnetic resonance imaging for local staging of prostate cancer: a diagnostic meta-analysis”. In: *European urology* 70.2 (2016), pp. 233–245.

[30] Andrew B Rosenkrantz et al. “Prostate cancer: comparison of 3D T2-weighted with conventional 2D T2-weighted imaging for image quality and tumor detection”. In: *American Journal of Roentgenology* 194.2 (2010), pp. 446–452.

[31] Antonio C Westphalen et al. “High-resolution 3-T endorectal prostate MRI: a multireader study of radiologist preference and perceived interpretive quality of 2D and 3D T2-weighted fast spin-echo MR images”. In: *American Journal of Roentgenology* 206.1 (2016), pp. 86–91.

[32] Edward O Stejskal and John E Tanner. “Spin diffusion measurements: spin echoes in the presence of a time-dependent field gradient”. In: *The journal of chemical physics* 42.1 (1965), pp. 288–292.

[33] NM Desouza et al. “Magnetic resonance imaging in prostate cancer: the value of apparent diffusion coefficients for identifying malignant nodules”. In: *The British journal of radiology* 80.950 (2007), pp. 90–95.

[34] Hebert Alberto Vargas et al. "Diffusion-weighted endorectal MR imaging at 3 T for prostate cancer: tumor detection and assessment of aggressiveness". In: *Radiology* 259.3 (2011), pp. 775–784.

[35] Rajakumar Nagarajan et al. "Correlation of Gleason scores with diffusion-weighted imaging findings of prostate cancer". In: *Advances in urology* 2012 (2012).

[36] Yuxi Pang et al. "Intravoxel incoherent motion MR imaging for prostate cancer: an evaluation of perfusion fraction and diffusion coefficient derived from different b-value combinations". In: *Magnetic resonance in medicine* 69.2 (2013), pp. 553–562.

[37] Kazuhiro Katahira et al. "Ultra-high-b-value diffusion-weighted MR imaging for the detection of prostate cancer: evaluation in 201 cases with histopathological correlation". In: *European radiology* 21.1 (2011), pp. 188–196.

[38] Yoshiko Ueno et al. "Computed diffusion-weighted imaging using 3-T magnetic resonance imaging for prostate cancer diagnosis". In: *European radiology* 23.12 (2013), pp. 3509–3516.

[39] Keyvan Farahani et al. "Effect of field strength on susceptibility artifacts in magnetic resonance imaging". In: *Computerized Medical Imaging and Graphics* 14.6 (1990), pp. 409–413.

[40] D Rickards. "Transrectal ultrasound 1992". In: *British journal of urology* 69.5 (1992), pp. 449–455.

[41] Yousef Mazaheri et al. "Diffusion-weighted MRI of the prostate at 3.0 T: comparison of endorectal coil (ERC) MRI and phased-array coil (PAC) MRI—the impact of SNR on ADC measurement". In: *European journal of radiology* 82.10 (2013), e515–e520.

[42] Natalie Korn et al. "Reduced-FOV excitation decreases susceptibility artifact in diffusion-weighted MRI with endorectal coil for prostate cancer detection". In: *Magnetic resonance imaging* 33.1 (2015), pp. 56–62.

[43] Lucy E Kershaw and David L Buckley. "Precision in measurements of perfusion and microvascular permeability with T1-weighted dynamic contrast-enhanced MRI". In: *Magnetic Resonance in Medicine: An Official Journal of the International Society for Magnetic Resonance in Medicine* 56.5 (2006), pp. 986–992.

[44] SM Noworolski et al. "Dynamic contrast-enhanced MRI in normal and abnormal prostate tissues as defined by biopsy, MRI, and 3D MRSI". In: *Magnetic Resonance in Medicine: An Official Journal of the International Society for Magnetic Resonance in Medicine* 53.2 (2005), pp. 249–255.

[45] Giovanna Russo et al. "Angiogenesis in prostate cancer: onset, progression and imaging". In: *BJU international* 110.11c (2012), E794–E808.

[46] Joseph L Sottnik et al. "The PCa tumor microenvironment". In: *Cancer Microenvironment* 4.3 (2011), pp. 283–297.

[47] Sofie Isebaert et al. "Multiparametric MRI for prostate cancer localization in correlation to whole-mount histopathology". In: *Journal of magnetic resonance imaging* 37.6 (2013), pp. 1392–1401.

[48] Eline K Vos et al. "Assessment of prostate cancer aggressiveness using dynamic contrast-enhanced magnetic resonance imaging at 3 T". In: *European urology* 64.3 (2013), pp. 448–455.

[49] Andrew B Rosenkrantz et al. "Dynamic contrast-enhanced MRI of the prostate with high spatiotemporal resolution using compressed sensing, parallel imaging, and continuous golden-angle radial sampling: preliminary experience". In: *Journal of Magnetic Resonance Imaging* 41.5 (2015), pp. 1365–1373.

[50] Fiona M Fennessy et al. "Dynamic contrast-enhanced magnetic resonance imaging in prostate cancer clinical trials: potential roles and possible pitfalls". In: *Translational oncology* 7.1 (2014), pp. 120–129.

[51] Barry G Hansford et al. "Dynamic contrast-enhanced MR imaging curve-type analysis: is it helpful in the differentiation of prostate cancer from healthy peripheral zone?" In: *Radiology* 275.2 (2015), pp. 448–457.

[52] Noel Weidner et al. "Tumor angiogenesis correlates with metastasis in invasive prostate carcinoma." In: *The American journal of pathology* 143.2 (1993), p. 401.

[53] Paul S Tofts et al. "Estimating kinetic parameters from dynamic contrast-enhanced T1-weighted MRI of a diffusable tracer: standardized quantities and symbols". In: *Journal of Magnetic Resonance Imaging: An Official Journal of the International Society for Magnetic Resonance in Medicine* 10.3 (1999), pp. 223–232.

[54] Yahui Peng et al. "Quantitative analysis of multiparametric prostate MR images: differentiation between prostate cancer and normal tissue and correlation with Gleason

score—a computer-aided diagnosis development study". In: *Radiology* 267.3 (2013), pp. 787–796.

[55] John V Hegde et al. "Multiparametric MRI of prostate cancer: an update on state-of-the-art techniques and their performance in detecting and localizing prostate cancer". In: *Journal of magnetic resonance imaging* 37.5 (2013), pp. 1035–1054.

[56] Fiona M Fennessy et al. "Practical considerations in T1 mapping of prostate for dynamic contrast enhancement pharmacokinetic analyses". In: *Magnetic resonance imaging* 30.9 (2012), pp. 1224–1233.

[57] Roberto Sanz-Requena et al. "Automatic individual arterial input functions calculated from PCA outperform manual and population-averaged approaches for the pharmacokinetic modeling of DCE-MR images". In: *Journal of Magnetic Resonance Imaging* 42.2 (2015), pp. 477–487.

[58] Juan E Ortuño et al. "DCE@ urLAB: a dynamic contrast-enhanced MRI pharmacokinetic analysis tool for preclinical data". In: *BMC bioinformatics* 14.1 (2013), p. 316.

[59] David S Smith et al. "DCEMRI. jl: a fast, validated, open source toolkit for dynamic contrast enhanced MRI analysis". In: *PeerJ* 3 (2015), e909.

[60] Frank G Zöllner et al. "UMMPerfusion: an open source software tool towards quantitative MRI perfusion analysis in clinical routine". In: *Journal of digital imaging* 26.2 (2013), pp. 344–352.

[61] Amita Shukla-Dave et al. “Detection of prostate cancer with MR spectroscopic imaging: an expanded paradigm incorporating polyamines”. In: *Radiology* 245.2 (2007), pp. 499–506.

[62] LC Costello and RB Franklin. “Novel role of zinc in the regulation of prostate citrate metabolism and its implications in prostate cancer”. In: *The Prostate* 35.4 (1998), pp. 285–296.

[63] John Kurhanewicz and Daniel B Vigneron. “Advances in MR spectroscopy of the prostate”. In: *Magnetic resonance imaging clinics of North America* 16.4 (2008), pp. 697–710.

[64] H Hricak. “MR imaging and MR spectroscopic imaging in the pre-treatment evaluation of prostate cancer”. In: *The British journal of radiology* 78.special_issue_2 (2005), S103–S111.

[65] John Kurhanewicz et al. “Combined magnetic resonance imaging and spectroscopic imaging approach to molecular imaging of prostate cancer”. In: *Journal of Magnetic Resonance Imaging: An Official Journal of the International Society for Magnetic Resonance in Medicine* 16.4 (2002), pp. 451–463.

[66] Thiele Kobus et al. “Mapping of prostate cancer by 1H MRSI”. In: *NMR in Biomedicine* 27.1 (2014), pp. 39–52.

[67] Miriam W Lagemaat et al. “1 H MR spectroscopic imaging of the prostate at 7 T using spectral-spatial pulses”. In: *Magnetic resonance in medicine* 75.3 (2016), pp. 933–945.

[68] Tuan-Khanh C Tran et al. "Very selective suppression pulses for clinical MRSI studies of brain and prostate cancer". In: *Magnetic Resonance in Medicine: An Official Journal of the International Society for Magnetic Resonance in Medicine* 43.1 (2000), pp. 23–33.

[69] Ryan G Males et al. "Clinical application of BASING and spectral/spatial water and lipid suppression pulses for prostate cancer staging and localization by in vivo 3D 1H magnetic resonance spectroscopic imaging". In: *Magnetic Resonance in Medicine: An Official Journal of the International Society for Magnetic Resonance in Medicine* 43.1 (2000), pp. 17–22.

[70] Charles H Cunningham et al. "Design of symmetric-sweep spectral-spatial RF pulses for spectral editing". In: *Magnetic Resonance in Medicine: An Official Journal of the International Society for Magnetic Resonance in Medicine* 52.1 (2004), pp. 147–153.

[71] Juyoung A Jung et al. "Prostate depiction at endorectal MR spectroscopic imaging: investigation of a standardized evaluation system". In: *Radiology* 233.3 (2004), pp. 701–708.

[72] Jurgen J Fütterer et al. "Standardized threshold approach using three-dimensional proton magnetic resonance spectroscopic imaging in prostate cancer localization of the entire prostate". In: *Investigative radiology* 42.2 (2007), pp. 116–122.

[73] Thiele Kobus et al. "In vivo assessment of prostate cancer aggressiveness using magnetic resonance spectroscopic imaging at 3 T with an endorectal coil". In: *European urology* 60.5 (2011), pp. 1074–1080.

[74] Kirsten M Selnæs et al. “Spatially matched in vivo and ex vivo MR metabolic profiles of prostate cancer–investigation of a correlation with Gleason score”. In: *NMR in biomedicine* 26.5 (2013), pp. 600–606.

[75] Sadhna Verma et al. “Prostate MRI and 3D MR spectroscopy: how we do it”. In: *American Journal of Roentgenology* 194.6 (2010), pp. 1414–1426.

[76] Alessandro Sciarra et al. “Magnetic resonance spectroscopic imaging (1H-MRSI) and dynamic contrast-enhanced magnetic resonance (DCE-MRI): pattern changes from inflammation to prostate cancer”. In: *Cancer investigation* 28.4 (2010), pp. 424–432.

[77] Otto Warburg. “On the origin of cancer cells”. In: *Science* 123.3191 (1956), pp. 309–314.

[78] Malcolm H Levitt. *Spin dynamics: basics of nuclear magnetic resonance*. John Wiley & Sons, 2001.

[79] Jan H Ardenkjær-Larsen et al. “Increase in signal-to-noise ratio of¿ 10,000 times in liquid-state NMR”. In: *Proceedings of the National Academy of Sciences* 100.18 (2003), pp. 10158–10163.

[80] Sarah J Nelson et al. “Metabolic imaging of patients with prostate cancer using hyperpolarized [1-13C] pyruvate”. In: *Science translational medicine* 5.198 (2013), 198ra108–198ra108.

[81] Mark J Albers et al. “Hyperpolarized 13C lactate, pyruvate, and alanine: noninvasive biomarkers for prostate cancer detection and grading”. In: *Cancer research* 68.20 (2008), pp. 8607–8615.

[82] Hsin-Yu Chen et al. “Technique development of 3D dynamic CS-EPSI for hyperpolarized 13C pyruvate MR molecular imaging of human prostate cancer”. In: *Magnetic resonance in medicine* 80.5 (2018), pp. 2062–2072.

[83] APS Kirkham et al. “Prostate MRI: who, when, and how? Report from a UK consensus meeting”. In: *Clinical radiology* 68.10 (2013), pp. 1016–1023.

[84] Kazuhiro Kitajima et al. “Prostate cancer detection with 3 T MRI: comparison of diffusion-weighted imaging and dynamic contrast-enhanced MRI in combination with T2-weighted imaging”. In: *Journal of Magnetic Resonance Imaging: An Official Journal of the International Society for Magnetic Resonance in Medicine* 31.3 (2010), pp. 625–631.

[85] Emine Ulku Saritas et al. “DWI of the spinal cord with reduced FOV single-shot EPI”. In: *Magnetic Resonance in Medicine: An Official Journal of the International Society for Magnetic Resonance in Medicine* 60.2 (2008), pp. 468–473.

[86] Baris Turkbey, Peter A Pinto, and Peter L Choyke. “Imaging techniques for prostate cancer: implications for focal therapy”. In: *Nature Reviews Urology* 6.4 (2009), p. 191.

[87] Thomas Hambrock et al. “Relationship between apparent diffusion coefficients at 3.0-T MR imaging and Gleason grade in peripheral zone prostate cancer”. In: *Radiology* 259.2 (2011), pp. 453–461.

[88] Courtney A Woodfield et al. “Diffusion-weighted MRI of peripheral zone prostate cancer: comparison of tumor apparent diffusion coefficient with Gleason score and percentage of tumor on core biopsy”. In: *American Journal of Roentgenology* 194.4 (2010), W316–W322.

[89] M-Y Wang, P-H Qi, and D-P Shi. “Diffusion tensor imaging of the optic nerve in subacute anterior ischemic optic neuropathy at 3T”. In: *American Journal of Neuroradiology* 32.7 (2011), pp. 1188–1194.

[90] Satoru Takahashi et al. “Tractography of the neu rovascular bundles of the prostate with zoom DTI technique: pre liminary report”. In: *ISMRM, Salt Lake city, USA* 1780 (2013).

[91] Carolin Reischauer et al. “High-resolution diffusion tensor imaging of prostate cancer using a reduced FOV technique”. In: *European journal of radiology* 80.2 (2011), e34–e41.

[92] Lisa Singer et al. “High-resolution diffusion-weighted magnetic resonance imaging in patients with locally advanced breast cancer”. In: *Academic radiology* 19.5 (2012), pp. 526–534.

[93] Chao Ma et al. “High resolution diffusion weighted magnetic resonance imaging of the pancreas using reduced field of view single-shot echo-planar imaging at 3 T”. In: *Magnetic resonance imaging* 32.2 (2014), pp. 125–131.

[94] Kazuhiro Kitajima et al. “High b-value diffusion-weighted imaging in normal and malignant peripheral zone tissue of the prostate: effect of signal-to-noise ratio”. In: *Magnetic Resonance in Medical Sciences* 7.2 (2008), pp. 93–99.

[95] Chan Kyo Kim, Byung Kwan Park, and Bohyun Kim. “High-b-value diffusion-weighted imaging at 3 T to detect prostate cancer: comparisons between b values of 1,000 and 2,000 s/mm2”. In: *American Journal of Roentgenology* 194.1 (2010), W33–W37.

[96] Amita Shukla-Dave and Hedvig Hricak. “Role of MRI in prostate cancer detection”. In: *NMR in Biomedicine* 27.1 (2014), pp. 16–24.

[97] Michele Fascelli et al. “The role of MRI in active surveillance for prostate cancer”. In: *Current urology reports* 16.6 (2015), p. 42.

[98] James L Leake et al. “Prostate MRI: access to and current practice of prostate MRI in the United States”. In: *Journal of the American College of Radiology* 11.2 (2014), pp. 156–160.

[99] Daniel T Oberlin et al. “Dramatic increase in the utilization of multiparametric magnetic resonance imaging for detection and management of prostate cancer”. In: *Abdominal Radiology* 42.4 (2017), pp. 1255–1258.

[100] Louise Clare Brown et al. “Multiparametric MRI to improve detection of prostate cancer compared with transrectal ultrasound-guided prostate biopsy alone: the PROMIS study.” In: *Health technology assessment (Winchester, England)* 22.39 (2018), p. 1.

[101] MJ Scheltema et al. "Utilization of multiparametric prostate magnetic resonance imaging in clinical practice and focal therapy: report from a Delphi consensus project". In: *World journal of urology* 35.5 (2017), pp. 695–701.

[102] Andrew B Rosenkrantz and Samir S Taneja. "Radiologist, be aware: ten pitfalls that confound the interpretation of multiparametric prostate MRI". In: *American Journal of Roentgenology* 202.1 (2014), pp. 109–120.

[103] Alexandre Ben Cheikh et al. "Evaluation of T2-weighted and dynamic contrast-enhanced MRI in localizing prostate cancer before repeat biopsy". In: *European radiology* 19.3 (2009), pp. 770–778.

[104] Amita Shukla-Dave et al. "Chronic prostatitis: MR imaging and 1H MR spectroscopic imaging findings—initial observations". In: *Radiology* 231.3 (2004), pp. 717–724.

[105] Michael S Leapman et al. "Impact of the integration of proton magnetic resonance imaging spectroscopy to PI-RADS 2 for prediction of high grade and high stage prostate cancer". In: *Radiologia brasileira* 50.5 (2017), pp. 299–307.

[106] Gillian Murphy et al. "The expanding role of MRI in prostate cancer". In: *American Journal of Roentgenology* 201.6 (2013), pp. 1229–1238.

[107] Klaas NA Nagel et al. "Differentiation of prostatitis and prostate cancer by using diffusion-weighted MR imaging and MR-guided biopsy at 3 T". In: *Radiology* 267.1 (2013), pp. 164–172.

[108] Olga Starobinets et al. "Characterization and stratification of prostate lesions based on comprehensive multiparametric MRI using detailed whole-mount histopathology as a reference standard". In: *NMR in Biomedicine* 30.12 (2017), e3796.

[109] Gregory T MacLennan et al. "The influence of chronic inflammation in prostatic carcinogenesis: a 5-year followup study". In: *The Journal of urology* 176.3 (2006), pp. 1012–1016.

[110] Meltem Esen et al. "Utility of ADC measurement on diffusion-weighted MRI in differentiation of prostate cancer, normal prostate and prostatitis". In: *Quantitative imaging in medicine and surgery* 3.4 (2013), p. 210.

[111] Jin Iwazawa et al. "Prostate cancer detection with MRI: is dynamic contrast-enhanced imaging necessary in addition to diffusion-weighted imaging?" In: *Diagnostic and Interventional Radiology* 17.3 (2011), p. 243.

[112] Rebecca L Siegel, Kimberly D Miller, and Ahmedin Jemal. "Cancer statistics, 2015". In: *CA: a cancer journal for clinicians* 65.1 (2015), pp. 5–29.

[113] Hashim U Ahmed et al. "Focal therapy for localised unifocal and multifocal prostate cancer: a prospective development study". In: *The lancet oncology* 13.6 (2012), pp. 622–632.

[114] Scott E Eggener et al. "A multi-institutional evaluation of active surveillance for low risk prostate cancer". In: *The Journal of urology* 189.1S (2013), S19–S25.

[115] Olga Starobinets et al. “Practical aspects of prostate MRI: hardware and software considerations, protocols, and patient preparation”. In: *Abdominal Radiology* 41.5 (2016), pp. 817–830.

[116] Hedvig Hricak et al. “Carcinoma of the prostate gland: MR imaging with pelvic phased-array coils versus integrated endorectal–pelvic phased-array coils.” In: *Radiology* 193.3 (1994), pp. 703–709.

[117] Matthew G Vander Heiden, Lewis C Cantley, and Craig B Thompson. “Understanding the Warburg effect: the metabolic requirements of cell proliferation”. In: *science* 324.5930 (2009), pp. 1029–1033.

[118] Robert Bok et al. “The Role of Lactate Metabolism in Prostate Cancer Progression and Metastases Revealed by Dual-Agent Hyperpolarized 13C MRSI”. In: *Cancers* 11.2 (2019), p. 257.

[119] Ralph J DeBerardinis et al. “Beyond aerobic glycolysis: transformed cells can engage in glutamine metabolism that exceeds the requirement for protein and nucleotide synthesis”. In: *Proceedings of the National Academy of Sciences* 104.49 (2007), pp. 19345–19350.

[120] SJ Kohler et al. “In vivo 13carbon metabolic imaging at 3T with hyperpolarized 13C-1-pyruvate”. In: *Magnetic Resonance in Medicine: An Official Journal of the International Society for Magnetic Resonance in Medicine* 58.1 (2007), pp. 65–69.

[121] Eline K Vos et al. “Clinical comparison between a currently available single-loop and an investigational dual-channel endorectal receive coil for prostate magnetic resonance

imaging: a feasibility study at 1.5 and 3 T". In: *Investigative radiology* 49.1 (2014), pp. 15–22.

[122] Walid E Kyriakos et al. "Sensitivity profiles from an array of coils for encoding and reconstruction in parallel (SPACE RIP)". In: *Magnetic Resonance in Medicine: An Official Journal of the International Society for Magnetic Resonance in Medicine* 44.2 (2000), pp. 301–308.

[123] John Kurhanewicz et al. "Phosphorus metabolite characterization of human prostatic adenocarcinoma in a nude mouse model by 31P magnetic resonance spectroscopy and high pressure liquid chromatography". In: *NMR in Biomedicine* 5.4 (1992), pp. 185–192.

[124] Hasan Aydin, Baki Hekimogl, and Idil Gunes Tatar. "Limitations, disabilities, and pitfalls of dynamic contrast-enhanced MRI as a diagnostic modality in prostate cancer". In: *American Journal of Roentgenology* 200.3 (2013), W326–W326.

[125] Gianluca Giannarini, Giuseppe Petralia, and Harriet C Thoeny. "Potential and limitations of diffusion-weighted magnetic resonance imaging in kidney, prostate, and bladder cancer including pelvic lymph node staging: a critical analysis of the literature". In: *European urology* 61.2 (2012), pp. 326–340.

[126] Antoine Lutti et al. "High-resolution functional MRI at 3 T: 3D/2D echo-planar imaging with optimized physiological noise correction". In: *Magnetic Resonance in Medicine* 69.6 (2013), pp. 1657–1664.

[127] VO Boer et al. “Parallel reconstruction in accelerated multivoxel MR spectroscopy”. In: *Magnetic resonance in medicine* 74.3 (2015), pp. 599–606.

[128] RL Segal, KD Miller, and A Jemal. “Cancer statistics, 2018”. In: *CA Cancer J Clin* 68 (2018), pp. 7–30.

[129] Peter R Carroll. *Early stage prostate cancer—do we have a problem with over-detection, overtreatment or both?* 2005.

[130] Virginia A Moyer. “Screening for prostate cancer: US Preventive Services Task Force recommendation statement”. In: *Annals of internal medicine* 157.2 (2012), pp. 120–134.

[131] Timothy J Wilt et al. “Systematic review: comparative effectiveness and harms of treatments for clinically localized prostate cancer”. In: *Annals of internal medicine* 148.6 (2008), pp. 435–448.

[132] Jan-Erik Johansson et al. “Natural history of early, localized prostate cancer”. In: *Jama* 291.22 (2004), pp. 2713–2719.

[133] Anna Bill-Axelson et al. “Radical prostatectomy versus watchful waiting in early prostate cancer”. In: *New England journal of medicine* 352.19 (2005), pp. 1977–1984.

[134] Matthew R Cooperberg, Jeanette M Broering, and Peter R Carroll. “Risk assessment for prostate cancer metastasis and mortality at the time of diagnosis”. In: *JNCI: Journal of the National Cancer Institute* 101.12 (2009), pp. 878–887.

[135] Berrend G Muller et al. "The role of magnetic resonance imaging (MRI) in focal therapy for prostate cancer: recommendations from a consensus panel". In: *BJU international* 113.2 (2014), pp. 218–227.

[136] Robert A Gatenby and Robert J Gillies. "Why do cancers have high aerobic glycolysis?" In: *Nature reviews cancer* 4.11 (2004), p. 891.

[137] MI Koukourakis et al. "Lactate dehydrogenase 5 isoenzyme overexpression defines resistance of prostate cancer to radiotherapy". In: *British journal of cancer* 110.9 (2014), p. 2217.

[138] Cara J Valvona et al. "The regulation and function of lactate dehydrogenase a: therapeutic potential in brain tumor". In: *Brain pathology* 26.1 (2016), pp. 3–17.

[139] Carmen Priolo et al. "AKT1 and MYC induce distinctive metabolic fingerprints in human prostate cancer". In: *Cancer research* 74.24 (2014), pp. 7198–7204.

[140] J-M Beauregard et al. "Pilot comparison of 18F-fluorocholine and 18F-fluorodeoxyglucose PET/CT with conventional imaging in prostate cancer". In: *Journal of medical imaging and radiation oncology* 54.4 (2010), pp. 325–332.

[141] M Farsad et al. "Positron-emission tomography in imaging and staging prostate cancer". In: *Cancer Biomarkers* 4.4-5 (2008), pp. 277–284.

[142] May-Britt Tessem et al. "Evaluation of lactate and alanine as metabolic biomarkers of prostate cancer using 1H HR-MAS spectroscopy of biopsy tissues". In: *Magnetic resonance in medicine* 60.3 (2008), pp. 510–516.

[143] Kayvan R Keshari et al. “Metabolic reprogramming and validation of hyperpolarized 13 C lactate as a prostate cancer biomarker using a human prostate tissue slice culture bioreactor”. In: *The Prostate* 73.11 (2013), pp. 1171–1181.

[144] James S Tropp et al. *Systems, methods and apparatus for an endo-rectal receive-only probe*. US Patent 7,945,308. 2011.

[145] Peder EZ Larson et al. “Fast dynamic 3D MR spectroscopic imaging with compressed sensing and multiband excitation pulses for hyperpolarized 13C studies”. In: *Magnetic resonance in medicine* 65.3 (2011), pp. 610–619.

[146] Peder EZ Larson et al. “Investigation of analysis methods for hyperpolarized 13C-pyruvate metabolic MRI in prostate cancer patients”. In: *NMR in Biomedicine* 31.11 (2018), e3997.

[147] John Maidens et al. “Optimizing flip angles for metabolic rate estimation in hyperpolarized carbon-13 MRI”. In: *IEEE transactions on medical imaging* 35.11 (2016), pp. 2403–2412.

[148] Wolfgang P Fendler et al. “68Ga-PSMA PET/CT detects the location and extent of primary prostate cancer”. In: *Journal of Nuclear Medicine* 57.11 (2016), pp. 1720–1725.

[149] Andrew B Rosenkrantz et al. “Prostate Imaging Reporting and Data System (PI-RADS), version 2: a critical look”. In: *American Journal of Roentgenology* 206.6 (2016), pp. 1179–1183.

[150] Matthew D Greer et al. "Accuracy and agreement of PIRADSv2 for prostate cancer mpMRI: a multireader study". In: *Journal of Magnetic Resonance Imaging* 45.2 (2017), pp. 579–585.

[151] Jelle O Barentsz et al. "Synopsis of the PI-RADS v2 guidelines for multiparametric prostate magnetic resonance imaging and recommendations for use". In: *European urology* 69.1 (2016), p. 41.

[152] Kirema Garcia-Reyes et al. "Impact of lesion visibility on transrectal ultrasound on the prediction of clinically significant prostate cancer (Gleason score 3+ 4 or greater) with transrectal ultrasound-magnetic resonance imaging fusion biopsy". In: *The Journal of urology* 199.3 (2018), pp. 699–705.

[153] Samuel Borofsky et al. "What are we missing? False-negative cancers at multiparametric MR imaging of the prostate". In: *Radiology* 286.1 (2017), pp. 186–195.

[154] Baris Turkbey and Peter L Choyke. "Multiparametric MRI and prostate cancer diagnosis and risk stratification". In: *Current opinion in urology* 22.4 (2012), p. 310.

[155] Hsin-Yu Chen et al. "Assessing prostate cancer aggressiveness with hyperpolarized dual-agent 3D dynamic imaging of metabolism and perfusion". In: *Cancer research* 77.12 (2017), pp. 3207–3216.

[156] Kengo Yoshimitsu et al. "Usefulness of apparent diffusion coefficient map in diagnosing prostate carcinoma: correlation with stepwise histopathology". In: *Journal of Magnetic Resonance Imaging: An Official Journal of the International Society for Magnetic Resonance in Medicine* 27.1 (2008), pp. 132–139.

[157] NM Desouza et al. "Diffusion-weighted magnetic resonance imaging: a potential non-invasive marker of tumour aggressiveness in localized prostate cancer". In: *Clinical radiology* 63.7 (2008), pp. 774–782.

[158] Baris Turkbey et al. "Is apparent diffusion coefficient associated with clinical risk scores for prostate cancers that are visible on 3-T MR images?" In: *Radiology* 258.2 (2011), pp. 488–495.

[159] Sadhna Verma et al. "Assessment of aggressiveness of prostate cancer: correlation of apparent diffusion coefficient with histologic grade after radical prostatectomy". In: *American Journal of Roentgenology* 196.2 (2011), pp. 374–381.

[160] Andrea Dueregger et al. "Differential utilization of dietary fatty acids in benign and malignant cells of the prostate". In: *PLoS One* 10.8 (2015), e0135704.

[161] Eric Eidelman et al. "The metabolic phenotype of prostate cancer". In: *Frontiers in oncology* 7 (2017), p. 131.

[162] Rouhallah Najjar Sadeghi, Fatemeh Karami-Tehrani, and Siamak Salami. "Targeting prostate cancer cell metabolism: impact of hexokinase and CPT-1 enzymes". In: *Tumor Biology* 36.4 (2015), pp. 2893–2905.

[163] Jeffrey Twum-Ampofo et al. "Metabolic targets for potential prostate cancer therapeutics". In: *Current opinion in oncology* 28.3 (2016), pp. 241–247.

[164] Nelma Pertega-Gomes et al. "A glycolytic phenotype is associated with prostate cancer progression and aggressiveness: a role for monocarboxylate transporters as

metabolic targets for therapy". In: *The Journal of pathology* 236.4 (2015), pp. 517–530.

[165] Patrizia Sanità et al. "Tumor-stroma metabolic relationship based on lactate shuttle can sustain prostate cancer progression". In: *BMC cancer* 14.1 (2014), p. 154.

[166] Jeremy W Gordon et al. "Translation of Carbon-13 EPI for hyperpolarized MR molecular imaging of prostate and brain cancer patients". In: *Magnetic resonance in medicine* 81.4 (2019), pp. 2702–2709.

Publishing Agreement

It is the policy of the University to encourage the distribution of all theses, dissertations, and manuscripts. Copies of all UCSF theses, dissertations, and manuscripts will be routed to the library via the Graduate Division. The library will make all theses, dissertations, and manuscripts accessible to the public and will preserve these to the best of their abilities, in perpetuity.

Please sign the following statement:

I hereby grant permission to the Graduate Division of the University of California, San Francisco to release copies of my thesis, dissertation, or manuscript to the Campus Library to provide access and preservation, in whole or in part, in perpetuity.

Author Signature

6/5/2019

Date